Technische Universität München

Fakultät für Chemie
Fachgebiet Organische Chemie

Quantification methods for time-resolved metabolic magnetic resonance imaging using hyperpolarized [1-^{13}C]pyruvate

Oleksandr Khegai

Vollständiger Abdruck der von der Fakultät für Chemie der
Technischen Universität München zur Erlangung des akademischen Grades
eines Doktors der Naturwissenschaften genehmigten Dissertation.

Vorsitzender:	Univ.-Prof. Dr. Bernd Reif
Prüfer der Dissertation:	1. Univ.-Prof. Dr. Steffen J. Glaser
	2. apl. Prof. Dr. Sibylle I. Ziegler

Die Dissertation wurde am 27.08.2013 bei der Technischen Universität München
eingereicht und durch die Fakultät für Chemie am 14.10.2013 angenommen.

"Everything should be made as simple as possible, but not simpler."

- Albert Einstein

Abstract

Quantification methods for time-resolved metabolic magnetic resonance imaging using hyperpolarized [1-^{13}C]pyruvate.

Dissolution dynamic nuclear polarization enables real-time non-invasive measurement of metabolic fluxes using magnetic resonance spectroscopy. Quantitative kinetic information of in vivo metabolism is of great interest for medicine as a key characteristic of some diseases. In this work, comprehensive methods for the data acquisition, quantification, interpretation and visualization of dynamic ^{13}C metabolite signals in vitro and in vivo were developed using the example of hyperpolarized [1-^{13}C]pyruvate.

Zusammenfassung

Quantifizierungsmethoden für zeitaufgelöste metabolische Magnetresonanz-Bildgebung mit hyperpolarisiertem [1-^{13}C]Pyruvat.

Dynamische Kernpolarisation in Flüssigkeiten ermöglicht nicht-invasive Echtzeit-Messung der metabolischen Flüsse mit Magnetresonanz-Spektroskopie. Quantitative kinetische Information über in-vivo Stoffwechsel ist von großem Interesse für die Medizin als wesentliches Merkmal von einigen Krankheiten. In dieser Arbeit wurden umfassende Methoden zur Datenerfassung, Quantifizierung, Interpretation und Visualisierung der dynamischen Signale von ^{13}C-Metaboliten in vitro und in vivo entwickelt am Beispiel von hyperpolarisiertem [1-^{13}C]Pyruvat.

Contents

1 Summary

The phenomenon of nuclear magnetic resonance (NMR) was first introduced in 1945 independently by Felix Bloch [1] and Edward Purcell [2], who were awarded for their achievements with the Nobel Prize in 1952. The fundamental principle of NMR is based on the interaction of atomic nuclei with an external magnetic field. Since the first applications in physics research, NMR spectroscopy has quickly become an important tool in chemistry and biochemistry. In the 70's Paul C. Lauterbur and Sir Peter Mansfield (both received Nobel Prize for Medicine 2003) showed the key ideas for the reconstruction of spatially resolved images using NMR ([3],[4]), which led to wide variety of applications in magnetic resonance imaging (MRI) and spectroscopy (MRS).

In medicine, today's MRI and MRS methods are mainly used for diagnostic purposes and allow the representation and differentiation of various tissues, such as the distinction between healthy and malignant structures. MRI is not limited only to morphology, but can also perform functional studies. For example, measurements of blood flow in a vessel, diffusion, perfusion or tissue activity can be quantified. Indeed, various atomic nuclei with a magnetic moment can be studied using NMR, the clinical use of MRI is still mainly limited to protons (^{1}H). Due to its high gyromagnetic ratio and high concentration in biological tissues, proton is the nucleus with the highest MR sensitivity and provides sufficient signal for fast imaging. The NMR signal, and thus, the signal-to-noise ratio (SNR) at a given magnetic field is dependent on the thermal equilibrium polarization of nuclear spins, which increases with the strength of the magnetic field. Another possibility for increasing the NMR signal provides so-called "hyperpolarization", i.e. an artificial non-equilibrium population of spin energy levels. This condition can be obtained using dynamic nuclear polarization (DNP) method based on the Overhauser effect [5]. Using hyperpolarization, MRI can be extended to other than ^{1}H atomic nuclei, e.g. ^{13}C. Based

on the low natural abundance, hyperpolarized MRI with ^{13}C-labeled compounds has an advantage in suppressing the background signal. Molecules containing carbon atoms play also a major role in metabolism and are therefore interesting for metabolic investigation. The main limitation of the method is the finite lifetime of the hyperpolarized state, determined by the spin-lattice relaxation time T_1.

The time evolution of the hyperpolarized signal differs substantially from the thermally polarized samples due to the non-recoverable magnetization. Additionally to the T_1 relaxation, hyperpolarized signal is depleted by radio frequency (RF) excitations required for MR imaging. The fast signal decay demands rapid execution of the experiments and careful choice of the acquisition strategies. The standard MR pulse sequences are suboptimal or even useless for the hyperpolarized imaging. Therefore, it is necessary to search for new acquisition strategies and to design appropriate pulse sequences for hyperpolarized MRI ([6],[7],[8],[9],[10],[11]).

The recent development of dissolution DNP enables NMR signal enhancement of ^{13}C-labeled compounds in liquid state by up to five orders of magnitude compared to thermal equilibrium ([12],[13]). Such drastically increased sensitivity allows in vivo measurement of metabolic fluxes in real time [14]. The T_1 relaxation time of hyperpolarized ^{13}C nuclei is a crucial limitation for the estimation of metabolic parameters and has to be in the order of metabolic conversion time or longer for meaningful signal acquisition. In case of significantly slower conversion and uptake, the non-recoverable, hyperpolarized ^{13}C signal disappears before downstream metabolite signals can be observed. High polarization levels (up to 50 %), long T_1 relaxation time (about 30 s in vivo and 60 s in vitro) together with rapid uptake and intracellular conversion make pyruvate a promising hyperpolarized agent to investigate metabolism ([15],[16]). Furthermore, the chemical shifts (CS) of pyruvate and its downstream metabolites are well separated as required for fast CS imaging (CSI).

In metabolically active tissues hyperpolarized [1-^{13}C]pyruvate rapidly exchanges with endogenous [1-^{13}C]lactate, [1-^{13}C]alanine, and ^{13}C-bicarbonate. Particularly, metabolic conversion of pyruvate to lactate is of great interest and is determined by lactate dehydrogenase (LDH) activity. Increases in LDH activity, changes in glutaminolysis, and decreases in pyruvate kinase activity have been associated with

cancer ([17],[18]). Recent studies have demonstrated feasibility of detecting these effect using hyperpolarized pyruvate ([19],[20],[21],[22],[23],[24],[25],[26]).

Similar to standard MRI, absolute quantification of ^{13}C metabolite signals is typically difficult due to uncertainties in experimental factors, such as polarization level, B_1 homogeneity, transmitter and receiver gain settings, T_1 relaxation, etc. The quantification of hyperpolarized ^{13}C spectra is commonly performed by either simple manual integration over the peaks or more advanced fitting algorithms such as AMARES or LCModel ([27],[28]). Except for LCModel, the methods require a manual user interaction, which can make the quantification user dependent. The LCModel algorithm works fully automatically, but was primarily designed for brain proton MRS. It needs first to be carefully adapted for hyperpolarized ^{13}C spectra [29], which typically have broad linewidths and only a few well separated peaks. Hence, it is useful to develop a user independent fully automatic spectral fitting method for hyperpolarized ^{13}C MRS, which utilize the specific properties of the ^{13}C spectra.

Different methods to quantify the hyperpolarized ^{13}C pyruvate metabolism are used in order to distinguish cancerous from healthy tissue or to detect treatment response and monitor cancer progression. Most commonly two-site kinetic modeling is applied on time-resolved spectral data ([20],[30]). The estimated exchange rate constants represent quantitatively metabolic flux of pyruvate. It has been shown that, in addition to any enzyme mediated net flux, exchange of the ^{13}C label has significant contribution to the lactate signal ([20],[31]). The two-site exchange approach has been demonstrated for in vitro experiments with cell cultures ([20],[32],[33],[34]) and in vivo experiments with signal acquisition from single slices or defined regions of interest ([20],[25],[35]). However, kinetic modeling of dynamic CS images is challenging due to the low SNR, which is based on smaller voxel sizes and fast decay of the hyperpolarized signals. For this reason, dynamic CS images are often represented as either time-averaged metabolite maps ([19],[21],[24],[36],[37],[38]) or metabolite ratios of certain time intervals ([20],[26],[29]). Furthermore, differences in pyruvate bolus arrival and manual choice of the starting point or the time interval cause difficulties on the standardization of imaging results.

The aim of this work was to develop new comprehensive methods for acquisition and quantification of dynamic hyperpolarized ^{13}C signals. The theoretically possible improvements of acquisition strategies are found by modifying and optimizing known imaging pulse sequences using optimal control theory. For the quantification purpose, first a simple time-domain spectral fitting is described based on CS inversion. The method is specifically adapted to the sparsity of hyperpolarized ^{13}C spectra typically consisting of only a few well-separated singlet peaks and the absence of a macromolecular baseline. The CS frequencies required for the CS inversion are obtained from iterative matching pursuit fitting. Secondly, apparent build-up and effective decay rates of downstream metabolites are estimated using a two-site exchange kinetic model. In the differential form the equations can be solved both in time and frequency domains without estimating an arterial input function. With temporally resolved CSI data, the method allows the extraction of spatially-resolved apparent build-up rate constant maps.

The main content of the thesis is divided into several chapters. Chapter two provides first a brief introduction to NMR and MRI, showing how the MR signal is produced, acquired and modeled. Further, in order to provide a foundation for most of the experimental part, the mechanism of DNP and basics of tumor metabolism are described. Finally, state-of-the-art of the hyperpolarized metabolic MRI is briefly discussed. Chapter three explores the theoretical aspects of the developed optimization and quantification algorithms together with utilized fast MR spectroscopic imaging. The experimental parameters and details are described in chapter four. Chapter five presents some theoretical results of the pulse sequence optimization. It also shows quantitative results of the developed quantification method for various types of experiments and the achieved significant improvements compared to other commonly used metrics. Chapter six concludes this work, summarizing the advantages and disadvantages of the proposed quantification method together with outlook on future development in this research area.

2 Introduction

Like other diagnostic medical imaging modalities, MRI is based on the interaction of the human body or rather particular organs or tissues with an outer radiation field. In addition to the X-rays, the human body is also transparent to radiation in the short and ultra short wavelength range. Unlike the classical X-ray imaging or computed tomography (CT), MRI uses the frequency window in the VHF range. Using pulsed radio frequency fields (RF pulses) in the MHz range, high magnetic field and superimposed in three dimensions magnetic field gradients, the sharp resonance absorption by atomic nuclei in the human body can be spatially encoded and thus the distribution of atomic nuclei can be visualized. The dependence of the NMR signal on tissue-specific parameters (proton density, relaxation time, chemical shift, etc.) as well as motion, flow, and diffusion, allows not only to reproduce morphological details with high resolution, but also to present functional processes in the human body.

2.1 Nuclear magnetic resonance

MRI relies on the phenomenon of nuclear magnetic resonance of atomic nuclei in a static external magnetic field. The interaction of the spins with an alternating magnetic field generates a dynamic change of the magnetization state of the whole system, which can be detected by proper instrumentation and further the signal-generating object can be reconstructed. MRI technology is generally based on the detection of MR signals from atomic nuclei in an external magnetic field after irradiation of RF pulse and subsequent post-processing.

2.1.1 Magnetic moment

The NMR phenomenon is based on the fundamental characteristic of the atomic nuclei to possess an angular momentum or so called spin. This spin is a result of rotation of subatomic particles, such as protons, neutrons, and electrons, about a

fixed axis, so that some atomic nuclei with unpaired spins (e.g. ^{1}H or ^{13}C) obtain an overall angular momentum J. Due to the fact that nucleus partially consists of charged particles, their rotation results in a total magnetic moment

$$\vec{\mu} = \gamma \vec{J} \tag{2.1}$$

The proportionality constant γ denotes the isotope-specific gyromagnetic ratio. According to quantum mechanics, the spin is quantized and therefore $\vec{\mu}$ can take only discrete values. These values are eigenvalues of the angular momentum operator. The possible values for the angular momentum along the z-axis are

$$J_z = \hbar m \tag{2.2}$$

with $\hbar = h/2\pi = 1{,}05459 \cdot 10^{-34}$ J·s and h Planck constant. The magnetic quantum number m indicates the degenerate spin energy levels. m can take the following values

$$m = I, I-1, \ldots, -I+1, -I$$

with I the nuclear spin quantum number, which can be full or half integer depending on the considered nuclei. The total number of all possible eigenvalues (stationary states) of the nucleus is then $2I+1$. The atomic nuclei of the isotopes ^{1}H and ^{13}C which will be considered in this work, have both magnetic quantum number $I = 1/2$. Due to this fact, there are only two possible eigenvalues for them $m = \pm 1/2$. The z-component of their magnetic moment is therefore

$$\mu_z = \gamma \hbar m = \pm \frac{1}{2} \gamma \hbar \tag{2.3}$$

In the absence of an external magnetic field, these two degenerate energy levels of atomic nuclei with eigenvalues $m = +1/2$ and $m = -1/2$ are energetically identical. However, bringing a nucleus into an external magnetic field B_0 (the coordinate system is chosen so that B_0 lies along the z-axis), the magnetic moment μ aligns parallel or anti-parallel to the magnetic field. The state with μ oriented parallel to the field direction is energetically more favorable. The potential energy

(normalized to $E_m = 0$ at $B_0 = 0$) is

$$E_m = -\mu_z B_0 = -\gamma \hbar B_0 m \tag{2.4}$$

With a positive γ (e.g. ^{1}H and ^{13}C) it raises linearly with the field strength B_0 at $m = -1/2$ ($E_\uparrow = -\frac{1}{2}\gamma \hbar B_0$) and sinks at $m = +1/2$ ($E_\downarrow = \frac{1}{2}\gamma \hbar B_0$) (Fig. 2.1).

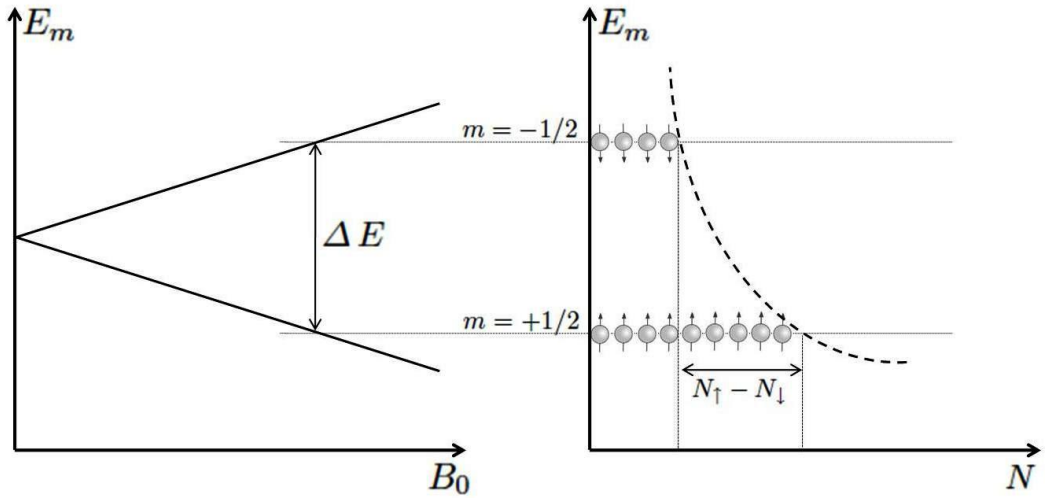

Figure 2.1: The splitting of the degenerate nuclear energy levels of the nucleus with the magnetic quantum number $I = 1/2$ by the applied magnetic field B_0.

In thermal equilibrium at the given temperature of the spin system T, the two energy levels are not equally populated. The difference between the two levels is described by the Boltzmann distribution

$$\frac{N_\uparrow}{N_\downarrow} = e^{\frac{\Delta E}{k_B T}} \tag{2.5}$$

with $N_\uparrow$ and $N_\downarrow$ the number of spins oriented parallel or anti-parallel to the field, respectively, ΔE the energy difference $\Delta E = E_\uparrow - E_\downarrow = \gamma \hbar B_0$, and $k_B = 1{,}38 \cdot 10^{-23}\ J/K$ the Boltzmann constant.

In practice, a spin system is always measured with a macroscopic magnetization M, which represents the sum of all N magnetic moments

$$M = \sum_i^N \mu_i \tag{2.6}$$

which, along with Eq. (2.3) and (2.5), results in

$$M = (N_\uparrow - N_\downarrow)\mu_z \approx \frac{N\gamma\,\hbar\,B_0}{2k_BT}\mu_z = \frac{N\gamma^2\,\hbar^2}{4k_BT}\,B_0 = \chi(T)B_0 \tag{2.7}$$

with χ magnetic susceptibility.

2.1.2 Bloch equations

The dynamics of the macroscopic magnetization vector $\vec{M}$ in magnetic field $\vec{B}$ is described by the Bloch equation

$$\frac{d\vec{M}}{dt} = \gamma(\vec{M} \times \vec{B}) \tag{2.8}$$

In addition to the static magnetic field $\vec{B_0}$, there are three other magnetic fields in the MR system: magnetic field inhomogeneity $\delta\vec{B}$, gradient field $\vec{k}(\vec{G}\vec{r})$ for the slice selection or signal readout (which is ideally linearly dependent on $\vec{r}$ with $\vec{G}$ the proportionality constant and $\vec{k}$ unit vector) and $\vec{B_1}$ field caused by RF pulse. Accordingly, Eq. (2.8) can be rewritten as

$$\frac{d\vec{M}}{dt} = \gamma\left[\vec{M} \times \left\{\vec{B_0} + \delta\vec{B} + \vec{k}(\vec{G}\vec{r}) + \vec{B_1}\right\}\right] \tag{2.9}$$

Neglecting the magnetic field inhomogeneity $\delta\vec{B}$ and setting the slice selection gradient and RF pulse to zero, Eq. (2.9) has a simple analytical solution. In this case the temporal behavior of the magnetization is a precession of the magnetization vector $\vec{M}$ about the direction of main magnetic field $\vec{B_0}$ with the Larmor frequency $\omega_L = \gamma B_0$.

2.1.3 Relaxation phenomena

Owing to motion, the molecules are influenced magnetically by their environment, e.g. by the dipole-dipole interaction (dipolar coupling), chemical shift anisotropy or electric quadrupole moment. These effects cause fluctuations of the local magnetic field, that all the individual magnetic moments in a sample experience.

In a highly simplified model, the longitudinal relaxation can be illustrated as follows: due to the field fluctuations, the magnetic field, about which the magnetic moment precesses, is slightly temporally variable in magnitude and direction.

The magnetic moments of a sample point in slightly different directions. Hence, the magnetic moment is moving between different precession cones and changes its orientation slowly over time. Over a longer time period, the magnetic moment may take any possible orientation in space. The distribution of the magnetic moments is however not isotropic. According to the Boltzmann distribution the movement towards lower energy alignment is more probable than the movement towards alignment with higher energy. Therefore the resulting macroscopic magnetization dissolves over time and undergoes a longitudinal relaxation towards the thermal equilibrium. The longitudinal relaxation is also called spin-lattice relaxation, since the energy is dissipated to the environment by the transition between the Zeeman eigenstates. The velocity of this process is tissue specific and is described by a characteristic time constant, the longitudinal relaxation time T_1. The relaxation process above is represented by the following phenomenological differential equation

$$\frac{dM_z}{dt} = \frac{M_0 - M_z}{T_1} \tag{2.10}$$

with M_z longitudinal and M_0 thermal equilibrium magnetization.

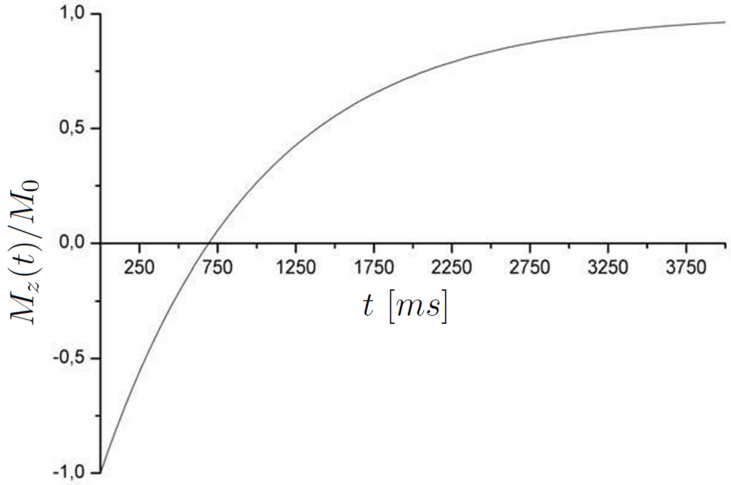

Figure 2.2: Time course of the longitudinal magnetization after complete inversion of the magnetization by 180° pulse. T_1 is approximately 1000 ms, a typical value e.g. for brain tissue.

The second relaxation process causes a faster than expected by the spin-lattice relaxation decrease of the transverse component of the magnetization. This is due to small inhomogeneities of the magnetic field caused by the interaction between

spins (spin-spin interaction). Because of these field fluctuations, the Larmor frequencies of the spins differ slightly, with the result that they lose their phase relation to each other, the coherence, which is the basis of the transverse magnetization. Due to this dephasing process, which is called spin-spin relaxation, the transverse magnetization in the excited volume decreases. The characteristic time constant, the transverse relaxation time T_2, determines the velocity of this process. Hence, the time dynamics of the transverse magnetization M_{xy} is described by

$$\frac{dM_{xy}}{dt} = -\frac{M_{xy}}{T_2} \tag{2.11}$$

Further faster compared to T_2 dephasing effects, that are triggered by temporally constant magnetic field inhomogeneities, can be characterized by the T_2' decay time. Here the imperfections of the main magnetic field B_0 as well as different diamagnetic or paramagnetic properties of the local environment (susceptibility) lead to field fluctuations. The experimentally observed decay of the transverse magnetization can thus be understood as the sum of the two effects and described by the overall T_2^* relaxation time whereby

$$\frac{dM_{xy}}{dt} = -\frac{M_{xy}}{T_2^*}, \text{ with} \qquad \frac{1}{T_2^*} = \frac{1}{T_2} + \frac{1}{T_2'} \tag{2.12}$$

In contrast to the spin-spin relaxation, the fluctuations of the main magnetic field caused by such inhomogeneities are constant in time. Through appropriate manipulation, the dephasing caused by this effect is reversible and forms the basis of the spin echo.

Taking into account the relaxation processes described above, the Bloch equation (2.8) transforms to

$$\frac{d\vec{M}}{dt} = \gamma(\vec{M} \times \vec{B}) - \begin{pmatrix} \frac{M_x}{T_2} \\ \frac{M_y}{T_2} \\ \frac{M_z - M_0}{T_1} \end{pmatrix} \tag{2.13}$$

In the coordinate system rotating at the Larmor frequency, the cross product is zero and once excited on-resonant magnetization vector undergoes only relaxation. The analytic solution of the Bloch equation is given then by

$$M_{xy}(t) = M_{xy}(0)e^{-\frac{t}{T_2}} \tag{2.14}$$

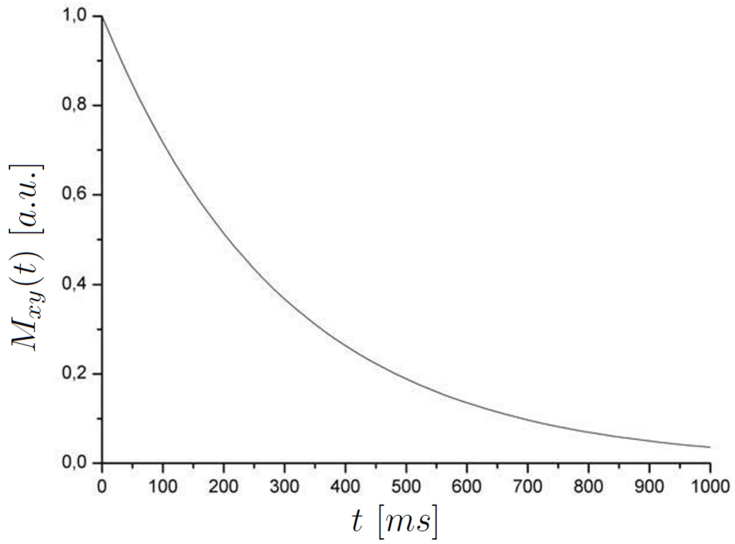

Figure 2.3: Time course of the transverse magnetization with a T_2 relaxation time of 300 ms. The fanning out of the spins causes the decay of the induction signal, which is also called free induction decay (FID).

and

$$M_z(t) = M_0(1 - e^{-\frac{t}{T_1}}) + M_z(0)e^{-\frac{t}{T_1}} \tag{2.15}$$

The transverse magnetization M_{xy} decays exponentially, the longitudinal magnetization M_z also moves exponentially to the equilibrium value (Fig. 2.2 and 2.3).

2.1.4 RF pulse

For the detection of MR signal, first a high frequency alternating magnetic field (RF pulse) has to be irradiated. It deflects the magnetization from the equilibrium. The duration of the RF pulse is considered to be very short compared with T_1 and T_2, in order to neglect the relaxation terms in Eq. (2.13). A typical pulse in MRI takes about $200\mu s$ to $5ms$ and is implemented by a high frequency alternating magnetic field $\vec{B_1}$ perpendicular to $\vec{B_0}$ (that means $B_x(t) = B_1 \cos(\omega t)$ and $B_y(t) = B_1 \sin(\omega t)$). According to Eq. (2.8) this results in

$$\begin{pmatrix} \dot{M}_x \\ \dot{M}_y \\ \dot{M}_z \end{pmatrix} = \gamma \begin{pmatrix} 0 & B_0 & B_1 \sin(\omega t) \\ -B_0 & 0 & B_1 \cos(\omega t) \\ -B_1 \sin(\omega t) & -B_1 \cos(\omega t) & 0 \end{pmatrix} \begin{pmatrix} M_x \\ M_y \\ M_z \end{pmatrix} \tag{2.16}$$

In the resonant case, i.e. $\omega = \omega_L$, along with the initial condition $\vec{M}(0) = (0, 0, M_0)$, the following analytical solution can be found

$$\begin{pmatrix} M_x \\ M_y \\ M_z \end{pmatrix} = M_0 \begin{pmatrix} -\sin(\alpha)\cos(\omega_L t) \\ \sin(\alpha)\sin(\omega_L t) \\ \cos(\alpha) \end{pmatrix} \tag{2.17}$$

This corresponds to a precession of the magnetization vector $\vec{M}$ about the direction of the main magnetic field with $\omega_L = \gamma B_0$. Additionally, this movement is superimposed with a helical rotation towards the xy plane (Fig. 2.4 left).

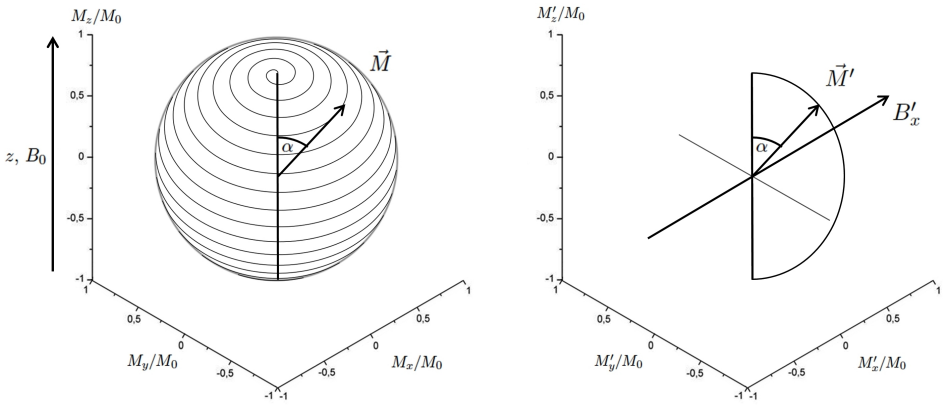

Figure 2.4: Temporal evolution of the macroscopic magnetization $\vec{M}$ and $\vec{M}'$ in static (left) and rotating (right) reference system upon irradiation of an alternating magnetic field with $\omega = \omega_L$.

The dependence of the flip angle α on the rotating at the Larmor frequency ω_L magnetic field B_1 is given by

$$\alpha = \int_0^\tau \gamma \left| \vec{B_1}(t) \right| dt \tag{2.18}$$

with τ the duration of the applied RF pulse. One speaks, for instance, about $\pi/2$ pulse, if the entire magnetization is flipped into the transverse plane perpendicular to the static magnetic field. The measured MR signal is generated by the precessing transverse magnetization that induces a voltage in the high frequency receiver coil (Fig. 2.5).

Considering Eq. (2.8) in a rotating with ω_L reference system, the high frequency magnetic field $\vec{B_1}(t)$ turns into the time independent field $B'_1 = (B_1, 0, 0)$. In this

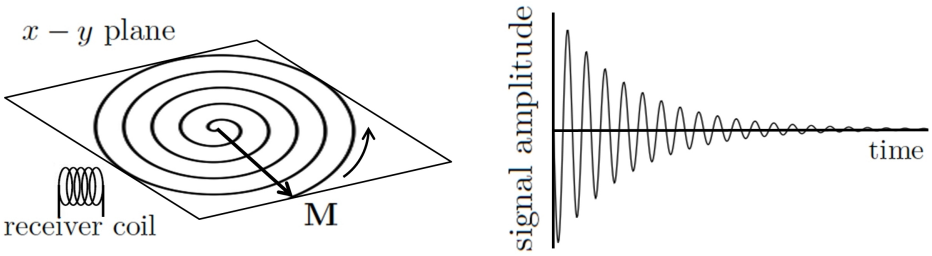

Figure 2.5: MR signal detection after RF pulse.

system, the following solution of Eq. (2.17) is obtained

$$\begin{pmatrix} M'_x \\ M'_y \\ M'_z \end{pmatrix} = M_0 \begin{pmatrix} 0 \\ \sin(\alpha) \\ \cos(\alpha) \end{pmatrix} \tag{2.19}$$

Thus, the transverse magnetization is produced by simple rotation of $\vec{M}'$ about the direction of the alternating magnetic field $\vec{B}'_1$ (Fig. 2.4 right).

2.1.5 Chemical shift

The environment of the spins influences not only the relaxation times, but also the resonance frequency ω_0. The electron shell of the atoms in the molecule shields diamagnetically the external magnetic field B_0, hence the nuclear spin sees only an effective magnetic field

$$B_{eff} = B_0(1 - \sigma) \tag{2.20}$$

with σ the "shielding" constant. Spins in differing chemical environments or structures have therefore distinct resonance frequencies

$$\omega_i = \gamma B_0(1 - \sigma_i) \tag{2.21}$$

The difference between the resonance frequencies is dependent on the type of bond and the binding partners of the considered spins. The chemical shifts are typically expressed as parts per million (ppm) with reference to a stable compound, in order not to be dependent on the strength of the magnetic field. The reference compound most often used is tetramethylsilane (TMS), all twelve hydrogen atoms of which are equivalent and result therefore in a strong singlet signal. Fig. 2.6

shows, as example, the ^{1}H MR spectrum of major metabolites in a normal brain.

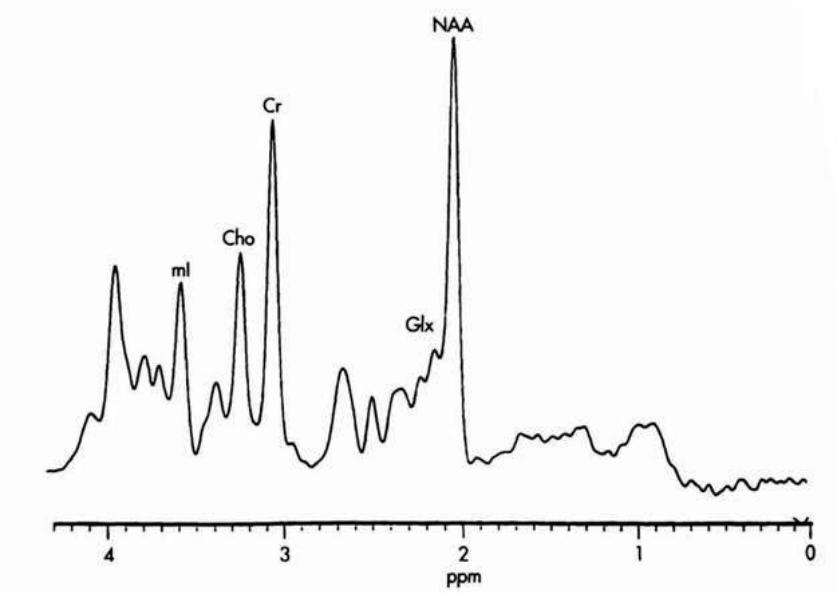

Figure 2.6: ^{1}H spectrum of major metabolites in a normal brain. NAA: N-acetylaspartate, Glx: Glutamine and glutamate, Cr: Creatine, Cho: Choline, mI: Myo-Inositol. The figure is reprinted with permission of the Department of Radiology at the University of Missouri-Kansas City, MO.

2.2 Magnetic resonance imaging

In 1973 Paul Lauterbur [3] and Peter Mansfield [4] independently published papers outlining the rudiments of MR imaging using spatially dependent magnetic fields. This allowed for determining the origin of the radio waves emitted from the nuclei of the object of study and thereby for the desired localization of the various signal contributions. By applying an additional constant magnetic field with gradient $\vec{G}$ to the static magnetic field, the Larmor frequency becomes a function of location

$$\omega_0(r) = \gamma(B_0 + \vec{G}\vec{r}) = \gamma(B_0 + G_x x + G_y y + G_z z) \tag{2.22}$$

Using gradients in all three spatial directions allows extraction of the entire spatial information of the sample. The principle of the encoding is explained below.

2.2.1 Slice selection

By applying a gradient $\vec{G}$ during the frequency selective RF pulse in, for instance, z direction, only the spins within particular slice will be excited (so-called "slice selective excitation"). The thickness of the slice (Fig. 2.7) is given by

$$\Delta z = \frac{\Delta\omega}{\gamma G_z} \tag{2.23}$$

with $\Delta\omega$ the frequency bandwidth of the pulse and G_z the slice selection gradient. In this case the term "selective excitation" is used. The frequency bandwidth depends on the shape of the RF pulse. Within the excited slice the spins precess with differing Larmor frequencies due to the finite bandwidth of the pulse. By adjusting the frequency band of the RF pulse, the selected slice can be moved along the z direction. Depending on the direction of the slice selection gradient, the slice can take any desired orientation in the magnetic field.

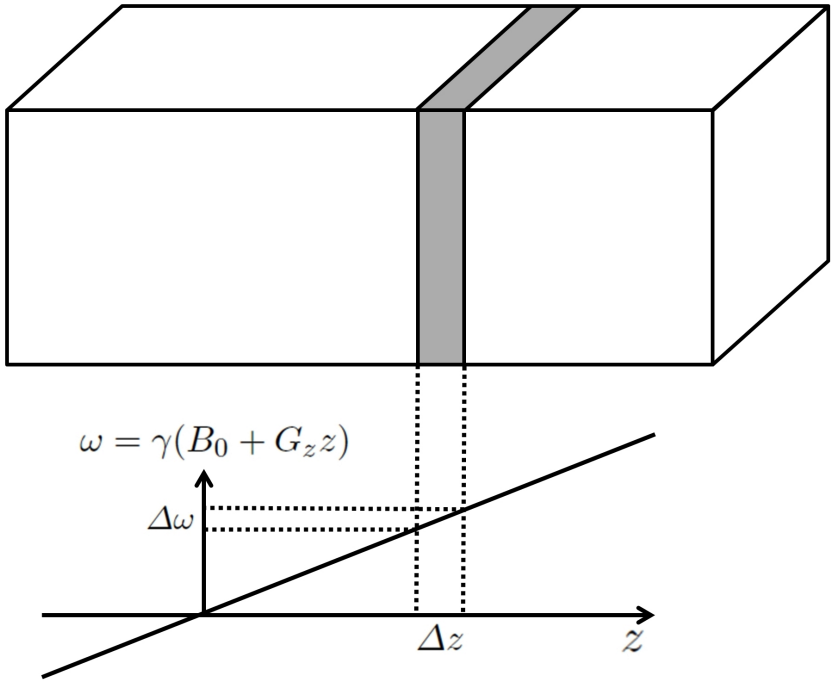

Figure 2.7: Slice selective excitation by an RF pulse. The resonance condition is satisfied only for the spins with the Larmor frequency in the $\Delta\omega$ range (the frequency bandwidth of the RF excitation pulse) along the z direction.

2.2.2 Spatial encoding and k-space

The basic idea of spatial encoding in the excited slice is based on the decomposition of the spin density distribution in individual spatially dependent frequency components. Also for this decomposition linear magnetic field gradients are used. The desired slice is described in the spatial domain by the spin density $\rho(x, y)$. The signal intensity is obtained by integrating the sum of the transverse magnetization over the entire slice and is given by

$$S(k_x,k_y) = C \int \int \rho(x, y) e^{i(k_x x + k_y y)} dx dy \tag{2.24}$$

Here, the so-called k-space is introduced with the coordinates

$$k_i = \gamma \int_0^t G_i(\tau) d\tau \tag{2.25}$$

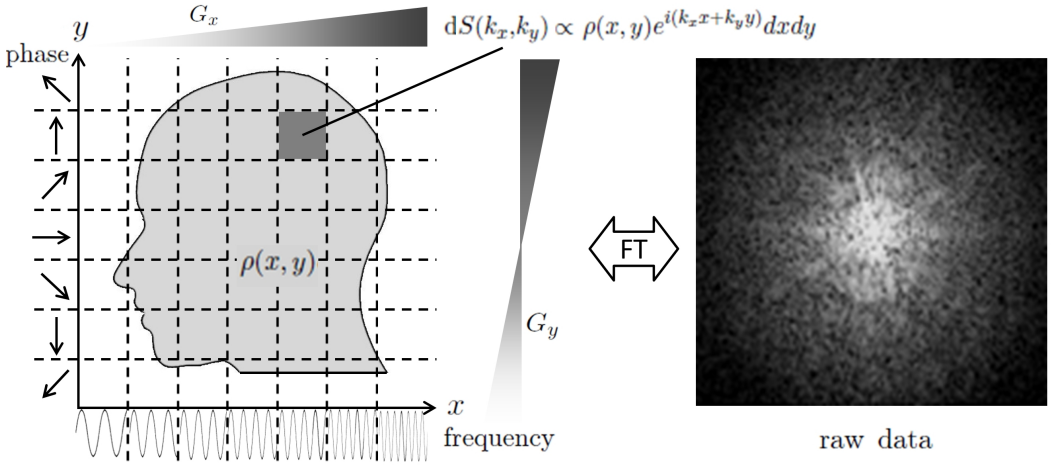

Figure 2.8: The principle of the 2D spatial encoding: differing precession frequencies are assigned to the spins along the reading direction (x), while differing signal phases are generated line by line in the phase encoding direction (y). The local signal components are thus assigned to their spatial localization. The acquired raw data matrix (k-space) is transformed by the 2D Fourier transform into the spatial domain.

The signal intensity in Eq. (2.24) represents the Fourier transform (FT) of the spin density distribution. Hence, using the inverse FT results in

$$\rho(x, y) = C \int \int S(k_x,k_y) e^{-i(k_x x + k_y y)} dk_x dk_y \tag{2.26}$$

According to that, the spin density of the object in the position-space (x, y) and the measured MR signal in the k-space (k_x, k_y) are connected by a FT. The spatial encoding of the MR signals corresponds by now to the filling of the components (k_x, k_y) of the k-space. For this purpose, the induced in the receiver coil continuous MR signal is sampled in discrete steps. By doing this, a two-dimensional data set is incrementally recorded by a successive acquisition of the MR signal, which obtained the spatial information in form of phase distribution by encoding gradients.

For basic MRI, typically Cartesian readout trajectories are used, i.e. the k-space is filled line by line. In order to reduce a scan time, so-called non-Cartesian sampling is utilized for specific applications. Typical trajectories in this case are radial and spiral, but there exists a multitude of other possibilities. In the case of spiral k-space filling, phase encoding and readout gradients have a sinusoidal growing envelope. In all cases, the continuous readout signal imposes k-space regularisation before the image can be reconstructed. The Fourier plane matrix values are calculated by mathematical interpolations that are more or less complex depending on the filling trajectory used. The spatial distribution of tissue-specific spin density can then be determined by simple inverse FT of the total signal $S(k_x,k_y)$ and provides the desired image information about the examined object. The two-dimensional FT is a standard method for image reconstruction in MRI. A schematic representation of the principle of the two-dimensional spatial encoding by linear magnetic field gradients is shown in Fig. 2.8.

2.2.3 Signal-to-noise ratio

An important parameter for the evaluation of image quality in MRI is the signal-to-noise ratio (SNR). The noise has two primary independent sources. First source is the measuring object itself and the noise is caused by the Brownian molecular motion of charged ions in biological tissues. The other noise component is caused by the thermal motion of electrons in the receiver coil and the downstream electronic circuit. The relationship between the SNR and the image and system parameters is given by

$$SNR \propto \frac{S\sqrt{VN_{av}T_{aq}}}{4k_BTR} \tag{2.27}$$

with S signal amplitude, V the voxel volume, N_{av} the number of averages, T_{aq} the acquisition time, k_B the Boltzmann constant, T the effective temperature of the

measured object and receiver circuit and R the specific resistance, which includes the resistance of the receiver circuit and of the measured object. The acquisition time T_{aq} includes receiver bandwidth $BW \propto 1/T_{aq}$, which is represented by the sampling rate. Higher sampling rate at the constant number of acquisition points causes shorter acquisition time T_{aq} and therefore lower SNR. On the other hand, low receiver bandwidth means high SNR, but longer measurement time.

2.2.4 Contrast-to-noise ratio and contrast resolution

The contrast-to-noise ratio (CNR) is an object size-independent measure of the signal level in the presence of noise. In MRI, CNR is the relationship of the absolute difference in intensities between two regions to the level of fluctuations in intensity due to the noise. Improving CNR increases perception of the distinct differences between two clinical areas of interest. CNR is a summary of both SNR and contrast. The strict definition is the difference in SNR between two relevant tissue types, A and B:

$$CNR = \frac{S_A - S_B}{\sigma} = SNR_A - SNR_B \tag{2.28}$$

The CNR is a good metrics for describing the signal amplitude relative to the ambient noise in an image, and it is particularly useful for simple objects. Because the CNR is computed using the difference in mean values between the signal region and the background, this metrics is most applicable when test objects that generate a homogeneous signal level are used. That is the case, where the mean gray scale in the signal ROI is representative of the entire object [43]. The CNR is useful for optimizing image acquisition parameters of generic objects of variable sizes and shapes.

Contrast resolution (CR) or contrast-detail is an approach to describing the image quality in terms of both the image contrast and resolution. CR is the ability to distinguish between differences in intensity in an image. The measure is used in medical imaging to quantify the quality of acquired images. It is a difficult quantity to define, because it depends on the human observer as much as the quality of the actual image. For example, the size of a feature affects how easily it is detected by the observer. One definition of image contrast is:

$$CR = \frac{S_A - S_B}{S_A + S_B} \tag{2.29}$$

2.2.5 Pulse sequences

In practice, the filling of the k-space is performed by so-called pulse sequences. Pulse sequence denotes a particular manner of MR signal acquisition and is predefined by designated amplitude, duration and timing of magnetic field gradients and RF pulses. Various pulse sequences differ in measurement time, the resulting contrast behavior and SNR of MR image, as well as in specific imaging artifacts. The choice of the pulse sequence is therefore very important for appropriate imaging and is highly dependent on desired application.

One of the most common MR pulse sequences is spin-echo pulse sequence (Fig. 2.9). The basic principle is based on the generation of Hahn's spin echo by refocusing the T_2^* signal decay. For this purpose, some time $TE/2$ after the first excitation pulse with a flip angle α, the second refocusing pulse α_R is applied. The excitation pulse generates the transverse magnetization, which dephases afterwards with T_2^*. The dephased magnetization is partially (only the inhomogeneous part) rephased by the following in $TE/2$ refocusing pulse, with the result that a spin echo signal is observed at time point TE. Any RF pulse pairs (α,α_R) can be used for spin echo creation, whereby the signal intensity at time point TE strongly depends on the choice of these flip angles. Typically the spin echo pulse sequence consists of a slice-selective 90° pulse followed by a slice-selective 180° refocusing pulse.

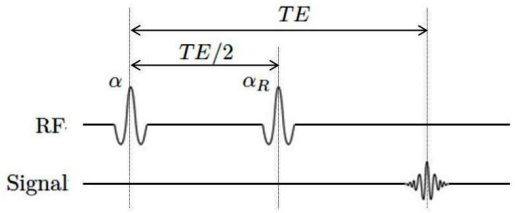

Figure 2.9: Spin echo pulse sequence

The gradient echo is another common signal rephasing mechanism, which provides the basis of many imaging techniques for fast data acquisition. In contrast to the spin echo, here the echo signal is obtained not due to the refocusing pulse α_R, but by a suitable time delayed switching of inverse magnetic field gradient (Fig. 2.10). In comparison to the spin-echo sequence, significantly shorter echo times can be achieved due to the lack of refocusing pulse. However, dephasing of the transverse magnetization, caused by the static magnetic field inhomogeneities, will not be refocused, so that in addition to T_1 the signal intensity is dependent on T_2^*

and not on T_2. The influence of the field inhomogeneities becomes greater with increasing echo time and thus the amplitude of the echo decreases.

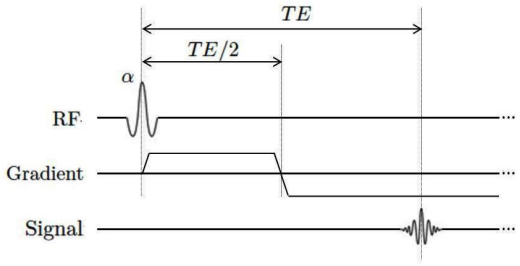

Figure 2.10: Gradient echo pulse sequence

Using small flip angle, the gradient echo sequence is also known as FLASH (fast low angle shot) sequence. The smaller flip angle allows not to consume the complete longitudinal magnetization by one excitation. Thus, there is still available residual magnetization after the excitation RF pulse, which can be used immediately. This allows shorter repetition times TR between the excitation pulses.

Other pulse sequences, which have been widely used for fast imaging in MRI, are CPMG (Carr-Purcell-Meiboom-Gill) and bSSFP (balanced steady state free precession) pulse sequences. For the CPMG pulse sequence [44], after a 90° excitation pulse a train of repeating 180° refocusing pulses is used (Fig. 2.11). The refocusing pulses are shifted in phase by 90° relative to the excitation pulse. It can be shown that in this way the error of the non-ideal flip angle can be averaged. Each refocusing pulse produces an echo. Its amplitude decays with T_2 that limits the number of refocusing pulses used after the excitation pulse.

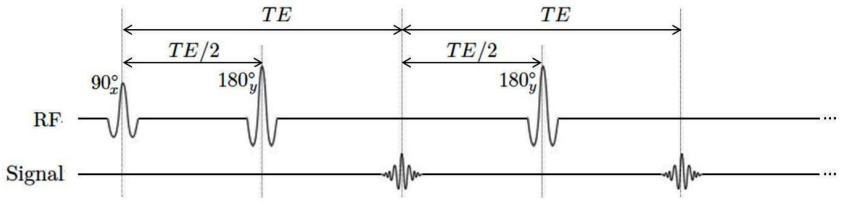

Figure 2.11: CPMG (Carr-Purcell-Meiboom-Gill) pulse sequence

The bSSFP pulse sequence ([45], [46]), also known as trueFISP (true fast imaging with steady state precession) or FIESTA (fast imaging employing steady state) is shown in Fig. 2.12. It uses alternating excitation pulses $\pm\alpha$ and generates an echo

signal at time TR. However, it takes some sequence cycles at the beginning to reach the steady state, which is usually performed by simple $-\alpha/2$ pulse. Starting directly with the bSSFP pulse sequence results in strong signal oscillations. An important property of bSSFP sequence, is the complete compensation of all gradient moments ($\int Gdt = 0$). Another feature of the bSSFP sequence is a strong sensitivity to off-resonance [47].

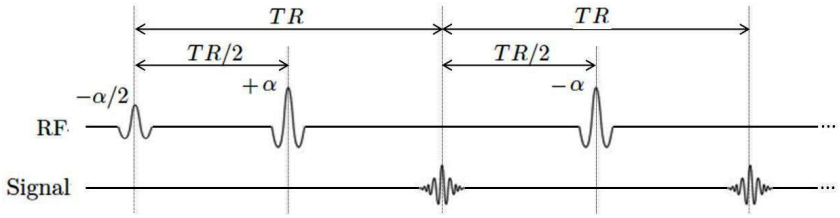

Figure 2.12: bSSFP (balanced steady state free precession) pulse sequence

Another relatively new pulse sequence, designed to be insensitive to the off-resonance effects and inaccuracies of the refocusing pulses, is so-called non-CPMG pulse sequence ([48],[49],[50]). Its main difference to the CPMG sequence is a quadratic phase modulation ($\varphi_n = \Delta n^2 + bn + c$) of the refocusing pulses, which allows the use of low excitation flip angles and non-ideal refocusing pulses. Using quadratic phase modulation, a particular off-resonance independent eigenstate of the magnetization can be obtained. Further advantage of this pulse sequence is a longer exponential decay of the total magnetization (between T_1 and T_2 relaxation times) compared to other pulse sequences. These properties make the non-CPMG pulse sequence very suitable for spectroscopic imaging of hyperpolarized nuclei. However, it is not trivial to obtain the mentioned before eigenstate in a short time, that raises the necessity and importance of the preparation pulses for non-CPMG sequence. Using the optimal control theory, which will be described in chapter 3.1., the preparation pulses can be found numerically.

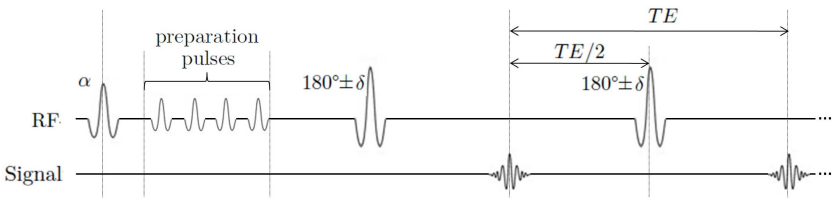

Figure 2.13: Non-CPMG pulse sequence.

2.2.6 MR scanner

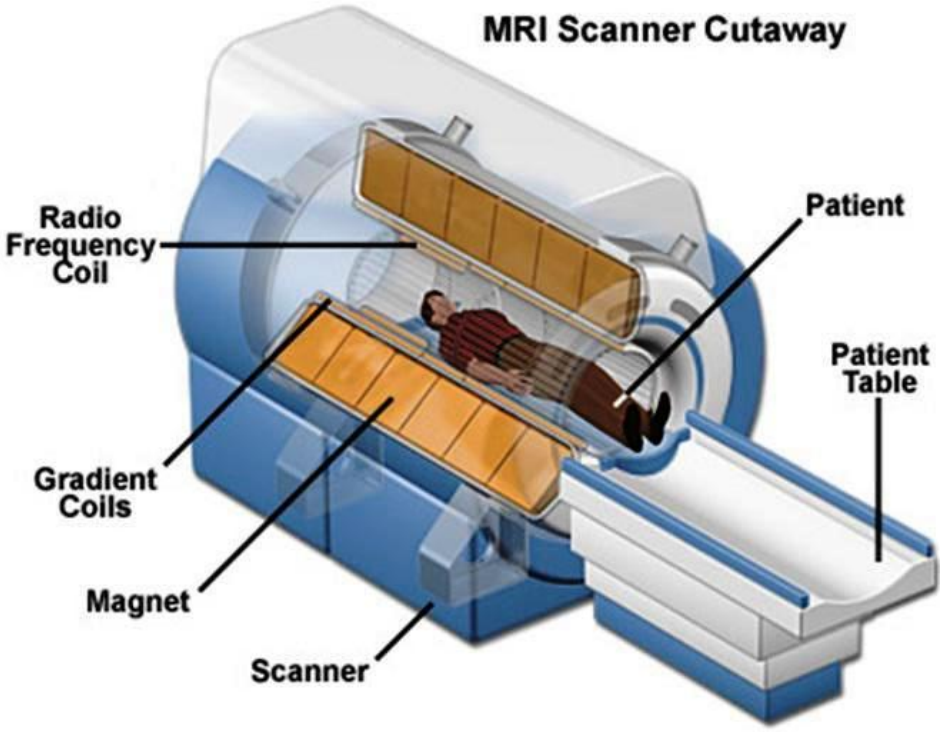

Figure 2.14: A cross-sectional illustration of a clinical MRI scanner showing the superconductive main magnet coils, the gradient coils, the RF coil, and a patient laying on a patient table. The figure is reprinted with permission of the National High Magnetic Field Laboratory, Tallahassee, FL.

An illustration of a clinical MRI scanner is shown in Fig. 2.14. The device consists of coaxial elements where the outermost one is the superconductive magnet generating the strong magnetic field for spin polarization. For clinical use, polarizing field strengths typically correspond to magnetic flux densities between 0.5 T and 3.0 T. For research use, the current highest field strength is 9.4 T for human scanner and 16.4 T for small animal system. A set of three gradient coils is placed inside the superconductive coil to generate gradient fields for image encoding. The most common way to generate xy-gradients is to utilize a set of interleaved saddle coils, where the z-gradient is generated with a Helmholtz coil.

The innermost part of the scanner is the whole body RF coil for excitation and detection of magnetization. When studying a defined anatomical region (e.g. knee,

neck) or for animal experiments, local transmit-receive and receive-only coils are typically used for higher signal to noise ratio.

2.3 Hyperpolarization

Assuming that the sample noise dominates over the coil noise [51], the SNR depends linearly on the product of the gyromagnetic constant of the nucleus γ, the polarization level P and the number of nuclei N

$$SNR \propto \gamma P N \tag{2.30}$$

In chapter 2.1 it was shown that the polarization level at thermal equilibrium is determined by the Boltzmann distribution and can be expressed as

$$P = \frac{\gamma \hbar B_0}{2 k_B T} \tag{2.31}$$

According to Eq. (2.30) and (2.31), the SNR obtained for nuclei at thermal equilibrium increases linearly with B_0 and quadratically with the gyromagnetic constant.

At magnetic field strength of 1.5 T and room temperature, the polarization of proton nuclei is $\approx 5 \cdot 10^{-5}$ and for ^{13}C nuclei $\approx 1 \cdot 10^{-5}$, based on the almost four times greater gyromagnetic ratio of ^{1}H nucleus ($\gamma_{^1H} = 2\pi \cdot 42{,}576$ MHz/T $\gamma_{^{13}C} = 2\pi \cdot 10{,}705$ MHz/T). The high concentration of protons in the human body and almost 100 % natural abundance of ^{1}H isotope are also a big advantage for imaging in comparison to ^{13}C molecules (natural abundance of ^{13}C is $\approx$ 1,1%). Consequently, the SNR of the ^{13}C nuclei is significantly lower than the one of protons in the human body.

If the polarization level is not determined by the thermal equilibrium, Eq. (2.30) is still valid and a linear dependence of the SNR on γ is expected instead, while the SNR dependence on the field strength, as shown in Eq. (2.31), is lost. One way to increase polarization and therefore the SNR offers the hyperpolarization, i.e. the polarization that is not caused by thermal Boltzmann distribution but by another external polarization method (Fig. 2.15). Following methods have been developed to generate the hyperpolarized state:

- **brute force**: thermal polarization at extremely low temperatures in very strong magnetic fields

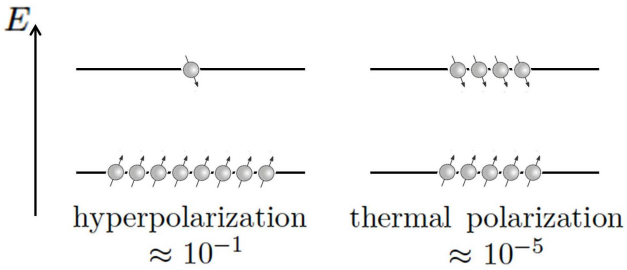

Figure 2.15: Schematic comparison of the thermal equilibrium polarization and hyperpolarized state

- **spin exchange optical pumping**: hyperpolarization of noble gases, e.g. ^{3}He and ^{129}Xe, based on the transmission of the electron spin of the alkali metals by stimulating their unpaired electrons with circularly polarized light in the presence of a quenching gas
- **para-hydrogen-induced hyperpolarization**: chemical method, which makes use of the correlation between nuclear spins in parahydrogen to create hyperpolarized molecules
- **dynamic nuclear polarization**: polarization based on transferring spin polarization from electrons to nuclei using suitable radicals

The "dynamic nuclear polarization" (DNP) method is best suited for the hyperpolarization of ^{13}C molecules.

2.3.1 Dynamic nuclear polarization

The DNP method [52] is based on the transfer of polarization from the electron spins of paramagnetic centers embedded in a glassy frozen solution to neighboring nuclear spins through dipolar interactions. It utilizes the property of electron spin, to possess at the same magnetic field and temperature a much higher polarization level than atomic nuclei due to the much higher magnetic moment of the electron spin (Fig. 2.16). This difference in polarization is given by the ratio of the electron to nuclei gyromagnetic ratio. For the purpose of DNP, the material containing the nuclei to be hyperpolarized is doped with a free radical. When exposed to a high magnetic field ($\approx$ 3T) and low temperature ($\approx$ 1K), the unpaired electrons of the free radical are highly polarized ($>$ 90 %), whereas the ^{13}C nuclei are polarized to only $<$ 0.1%. Due to weak interactions between electrons and nuclei (based

on Overhauser effect [5], solid-effect, thermal-mixing or the cross-effect [53],[54]), polarization is transferred from the unpaired electrons to the nuclei by the use of sufficiently long microwave irradiation near the electron paramagnetic resonance frequency.

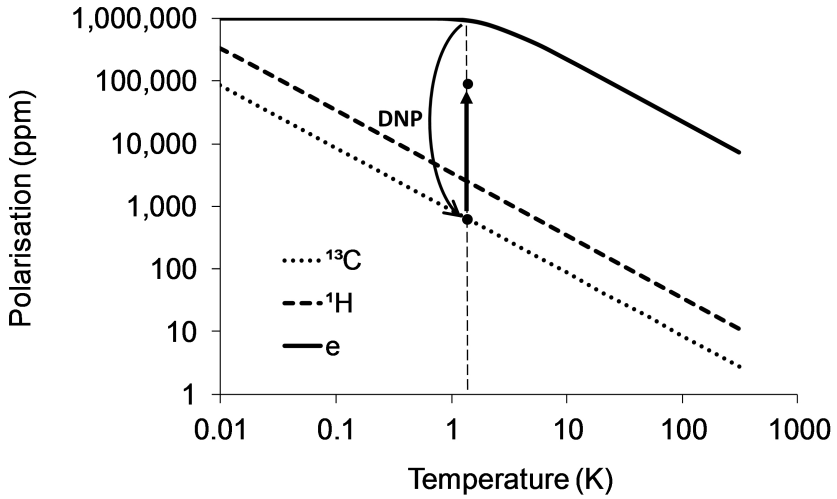

Figure 2.16: Temperature dependence of the electron and nuclear spin reservoir polarization of ^{1}H and ^{13}C at a given external field strength of 3.35 T

By rapid melting and dissolving, the solid can be transformed into an injectable liquid, with small to negligible polarization losses [12]. Using this method, the polarization of ^{13}C nuclei can be increased up to $\approx 3{,}7 \cdot 10^{-1}$, that is more than 10,000 times higher than the thermal equilibrium polarization. However, due to the deviation from the equilibrium state, the lifetime of the formed hyperpolarization is limited, the polarized spin system relaxes with T_1 relaxation time towards the thermal equilibrium. Therefore, for further experiments substances with long T_1 are preferred.

2.4 Tumor metabolism

Tumor metabolism can be viewed as the sum of a large but finite number of interdependent biochemical pathways, each of which provides a specific function for the cell [55]. Many of these pathways, particularly glycolysis and the tricarboxylic acid (TCA) cycle are subject to alternative regulation in cancer. A prominent feature of tumor metabolism is that it differs from that of the surrounding tissue.

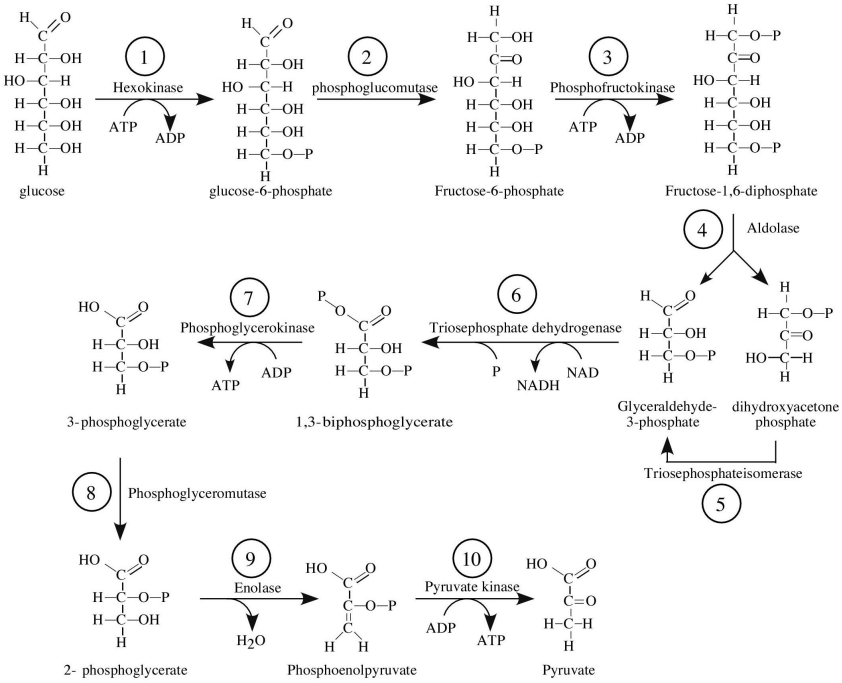

Figure 2.17: Schematic representation of glycolysis. The figure is reprinted with permission of the Department of Biology at the Indiana University, IN.

In the 1920s, Otto Warburg demonstrated that tumors have high rates of glucose consumption and lactate production compared with the normal tissue [56]. This observation created the research field of tumor metabolism, which has been dominated largely by the study of glycolysis (Fig. 2.17) and has been exploited in the clinics by metabolic imaging techniques, namely positron emission tomography (PET) with [^{18}F]-fluoro-2-deoxyglucose (FDG). Because of high levels of glucose transporters and hexokinase activity, cancer cells demonstrate high FDG uptake and phosphorylation compared with the normal tissue. Enhanced fluxes in other pathways including lipid synthesis, amino acid transport, and nucleotide transport have also been observed in aggressive tumors and are being investigated for diagnostic purposes or as therapeutic targets. Most tumors have also an acidic extracellular pH compared with normal tissue.

2.4.1 Pyruvate metabolism

The metabolism of pyruvate (Fig. 2.17) belongs to the fingerprint of a cell's metabolism. Being the end product of glycolysis, its production depends highly

on the rate of glycolysis. Mainly pyruvate is reduced by the coenzyme nicotinamide adenine dinucleotide (NADH) produced in the pathway to generate lactate, in the reaction catalyzed by the enzyme LDH. Alternatively, pyruvate undergoes transamination with glutamate to form alanine, in the reaction catalyzed by alanine transaminase (ALT). The reactions catalyzed by both LDH and ALT are readily reversible in the cell. A third reaction involves the irreversible decarboxylation of pyruvate by the pyruvate dehydrogenase (PDH) complex to carbon dioxide and acetyl CoA, which can enter the TCA cycle. The carbon dioxide released is subsequently interconverted with bicarbonate in the reaction catalyzed by carbonic anhydrase (CA). The structural formulas of the main metabolites considered in this work are shown in Fig. 2.18.

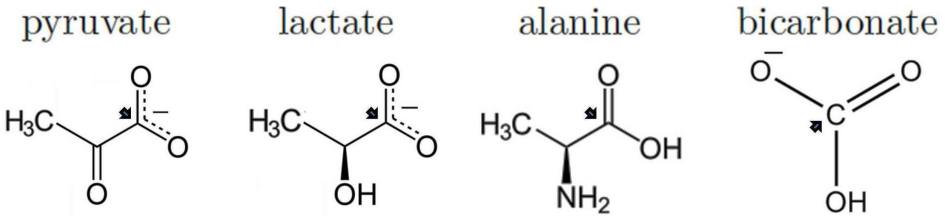

Figure 2.18: Structural formula of pyruvate, lactate, alanine and bicarbonate. The arrows show the location of the ^{13}C isotope for [1-^{13}C]pyruvate, [1-^{13}C]lactate, [1-^{13}C]alanine and ^{13}C-bicarbonate.

Simplified, the main metabolic reactions of pyruvate can be represented as

1. pyruvate + NADH + H^+ $\overset{LDH}{\leftrightarrow}$ lactate + NAD^+

2. pyruvate + glutamate $\overset{ALT}{\leftrightarrow}$ alanine + α-ketoglutarate

3. pyruvate + CoA $\overset{PDH}{\rightarrow}$ CO_2 + acetyl-CoA , and the following reaction $CO_2 + H_2O \overset{CA}{\leftrightarrow}$ bicarbonate + H^+

2.5 Hyperpolarized metabolic MRI

The metabolic imaging enables not only to determine the position of the atomic nucleus, but also provides information about the molecule, to which the detected nucleus belongs. This allows to track the metabolic pathway of a substance or to

observe metabolic processes in specific organs. Since the metabolism in the diseased organs typically differs from the metabolism in healthy organs, metabolic imaging is of great interest for medicine. A good example of the metabolic imaging is PET. After injection of [^{18}F]-FDG, it is possible to detect the regions of high glucose uptake and metabolism. On the other hand, it is known that the metabolism and uptake of glucose in some tumor types is more intense, what therefore allows efficient tumor localization.

Successful molecular imaging is primarily based on two key factors: high SNR, which makes possible to detect molecules at extremely low concentrations, and a good spatial resolution. No metabolic imaging technique can currently fulfill both criteria. Indeed, PET can achieve high SNR and even the molar concentrations lower than 10^{-11} M can be detected, the spatial resolution is poor ($\approx 5 - 10$ mm). MRI provides superior spatial resolution, but is not able to detect molar concentrations below 10^{-11} M. Hyperpolarized MRI method promises not only to fulfill the two criteria mentioned before, but also to make the dynamic metabolic imaging possible. For this purpose, an appropriate hyperpolarized contrast agent is required.

2.5.1 ^{13}C-labeled compounds for hyperpolarized MRI

The pharmacokinetic and pharmacological behavior of the hyperpolarized contrast agent depends only on the selected molecule, as the hyperpolarization does not change the chemical or physical properties of the substance. ^{13}C-labeled molecules are mostly suitable for reasonable metabolic MRI due to the following properties:

- ^{13}C is a stable isotope
- ^{13}C is magnetically active ($\gamma_{^{13}C} = 1/4 \cdot \gamma_{^{1}H}$)
- some ^{13}C-labeled molecules have long T_1 relaxation time $\approx 20 - 60$ s
- ^{13}C-labeled molecules have relatively high polarization level (up to 50 %)
- ^{13}C has negligible in vivo signal ($\approx$ 1,1% natural abundance)
- carbon-based molecules play a major role in metabolism

A combination of these properties together with

- non-toxicity

- fast uptake and metabolic conversion
- suitable for imaging CS of downstream metabolites
- correlation with disease progression and response to therapy

makes some hyperpolarized agent, described below, feasible for clinical application.

2.5.2 [1-^{13}C]pyruvate

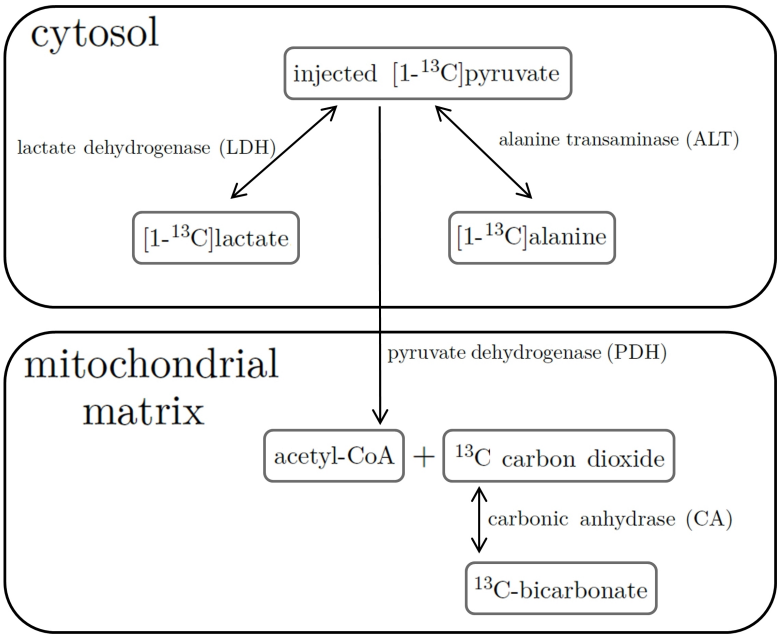

Figure 2.19: Diagram of metabolic pathways investigated with DNP hyperpolarized [1-^{13}C]-pyruvate. Pyruvate/lactate conversion is catalyzed by lactate dehydrogenase (LDH), and pyruvate/alanine conversion is catalyzed by alanine transaminase (ALT). Pyruvate is irreversibly converted to acetyl-CoA and CO_2 by pyruvate dehydrogenase (PDH), and CO_2 is in a pH-dependent equilibrium with bicarbonate [39].

A particularly interesting and promising substance for hyperpolarization and further investigation is [1-^{13}C]-pyruvate. It has been the most widely studied substrate to date, reflecting its central role in cellular metabolism (see chapter 2.4.1), the ease with which it can be hyperpolarized, its relatively long T_1 relaxation time, and its very rapid transport across the cell membrane and subsequent metabolism. In metabolically active tissues, following injection, hyperpolarized [1-^{13}C]pyruvate is absorbed by tissues and metabolized to [1-^{13}C]lactate, [1-^{13}C]alanine, and ^{13}C-bicarbonate (Fig. 2.19).

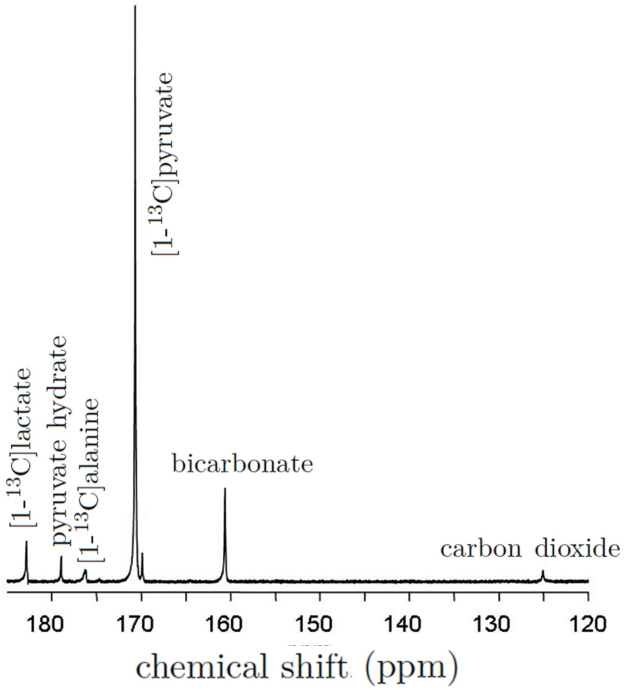

Figure 2.20: In vivo ^{13}C NMR spectrum (in Hz) after injection of [1-^{13}C]pyruvate.

Due to the differing CSs of downstream metabolites (Fig. 2.20), it is possible to distinguish the metabolite signals spectrally. Hyperpolarized pyruvate can be used for tumor localization, identification of tumor grade or assessment of tumor response to therapy.

Following alternative substrates have been successfully hyperpolarized and used in preclinical models (together with their clinical potential):

- **^{13}C bicarbonate**: rapid interconversion with $^{13}CO_2$, catalyzed by carbonic anhydrase, can be used for in vivo pH measurement
- **[1,4-^{13}C]fumarate**: conversion via enzyme fumarase to [1,4-^{13}C]malate as a marker of cellular necrosis
- **[1-^{13}C]lactate**: similar to pyruvate metabolism, measurement of backward conversion of lactate to pyruvate, i.e. LDH activity measurement
- **[1-^{13}C]urea**: metabolically inactive agent for perfusion measurement

- **[5-^{13}C]glutamine**: conversion to [5-^{13}C]glutamate, catalyzed by intramitochondrial glutaminase, as a marker of tumor growth and cell proliferation
- **[1-^{13}C]acetate**: conversion to acetyl CoA and acetyl carnitine enables probing fatty acid metabolism
- **[2-^{13}C]fructose**: its uptake enables probing glucose transporter GLUT5 distribution and hexokinase activity
- **[1-^{13}C]-α-ketoisocaproate**: metabolism to leucine by the enzyme branched chain amino acid transferase (BCAT), which is found to be upregulated in some tumors

One of the possible strengths of DNP is the ability of co-polarization of more than one substrate for probing several metabolic processes simultaneously [57].

3 Theory and Methods

In order to acquire time-resolved metabolic MR images of sufficiently high quality, an appropriate pulse sequence for hyperpolarized MRI needs to be designed, that provides a predictable high MR signal during the acquisition time. The first part of this chapter is focused on the development and optimization of such pulse sequences for hyperpolarized ^{13}C MRI. The developed spectral and kinetic fitting methods for hyperpolarized ^{13}C signal quantification are explained in the second part of this chapter. Quantitative kinetic information about pyruvate metabolism in tissue is of great interest as a key characteristic of some diseases and requires direct measurement of the metabolic conversion rates. Kinetic determination of metabolic conversion was performed by simple and robust spectral fitting of time-resolved FID signal of ^{13}C-labeled metabolites and subsequent kinetic modeling using a two compartment model between pyruvate and each downstream metabolite independently. Combining the developed quantification method with IDEAL spiral chemical shift imaging (CSI) enables spatially-resolved metabolic conversion rate mapping. Optimization, offline reconstruction and quantification algorithms were implemented in MATLAB (The MathWorks, Natick, MA, USA) in a semi-automatic fashion.

3.1 Optimal control design of pulse sequences

The optimal control theory (OCT) is a modern numerical approach to the dynamic optimization problem for nonlinear systems, based on the minimization of the determined cost function by searching optimal values of the selected control variables or so-called optimal path [63]. Applying OCT to the Bloch equations (which are represented by a system of bilinear equations) allows to control the dynamics of the magnetization by RF pulses and thus to design a pulse sequence, which satisfies particular predefined conditions ([64],[65],[66],[67]). In the following, the application of OCT to a system of the magnetization vectors within particular

CS offset and B_1 field inhomogeneity is presented, in order to obtain long stable echo train with a high total signal for data acquisition.

3.1.1 Optimal control theory

OCT can be applied to dynamic systems under particular conditions that can be summarized in following three criteria:

- **dynamic equation:** The system should be described by the dynamic equation, which is generally represented by a time-dependent differential equation

$$\dot{\vec{x}} = \vec{f}(\vec{x}(t), \ldots) \tag{3.1}$$

  with vec $\vec{x}(t)$ denoting the time-dependent system states. By controlling the system in a time interval t_0 to t_1, the system moves from the initial state $\vec{x}(t_0)$ to the target state $\vec{x}(t_1)$.

- **control variables:** There should be a possibility to influence and thus to control the path $\vec{x}(t)$ from the initial to the target state of the system. This can be realized through the introduction of the control variables $\vec{u}(t)$ to the system. Thus, Eq. (3.1) transforms to

$$\dot{\vec{x}} = \vec{f}(\vec{x}(t),\vec{u}(t),t) \tag{3.2}$$

- **control path:** Multiple possible control paths must exist, which can be influenced by the control variables.

The objective of OCT is finding an optimal path. It has to be previously defined, which requirements the optimal path should meet and how to compare different paths with each other. Therefore, a so-called cost function is introduced, which obtains the minimal value in case of an optimal path. The cost function can be defined by two independent components:

- **running cost:** The requirements that the path has to meet during the system movement (e.g. minimizing the distance between two points). The running cost can be described by

$$J_{run} = + \int_{t_0}^{t_1} L(\vec{x}(t),\vec{u}(t),t)dt \tag{3.3}$$

with function $L(\vec{x}(t),\vec{u}(t),t)$ dependent on the goal of optimization.

- **final cost:** The requirements that the system has to meet at the end of the movement (e.g. reaching particular final state). The final cost depends only on the final time t_1 and can be represented as

$$J_{fin} = \Phi(\vec{x}(t_1)) \tag{3.4}$$

The sum of these two functions forms a total cost function. The optimal control path should then satisfy the following condition

$$\min_{u(t)} J_{total} = \min_{u(t)} \left[\Phi(\vec{x}(t_1)) + \int_{t_0}^{t_1} L(\vec{x}(t),\vec{u}(t),t)dt \right] \tag{3.5}$$

Introducing the so-called Hamiltonian function,

$$H(\vec{x}(t),\vec{u}(t),t) = L(\vec{x}(t),\vec{u}(t),t) + \vec{\lambda}(t) \cdot \vec{f}(\vec{x}(t),\vec{u}(t),t) \tag{3.6}$$

with $\vec{\lambda}(t)$ so-called Lagrange multiplier function, allows to derive the variation of the total cost function

$$\begin{aligned} \delta J = \frac{\partial J}{\partial x}\delta x + \frac{\partial J}{\partial u}\delta u = \left(\frac{\partial \Phi(\vec{x}(t_1))}{\partial \vec{x}} - \vec{\lambda}(t_1) \right) \delta x \\ + \int_{t_0}^{t_1} \left\{ \left(\frac{\partial H(\vec{x}(t),\vec{u}(t),t)}{\partial \vec{x}} + \dot{\vec{\lambda}}(t) \right) \delta x + \frac{\partial H(\vec{x}(t),\vec{u}(t),t)}{\partial \vec{u}} \delta u \right\} dt \end{aligned} \tag{3.7}$$

The necessary condition for optimality is that the variation δJ of the modified cost function with respect to all feasible variations δx and δu should vanish

$$\delta J = 0 \tag{3.8}$$

Since δx and δu are independent, this condition can be achieved only in the case when all terms of the Eq. (3.7) are zero. Thus, the following equations are derived

$$\vec{\lambda}(t_1) = \frac{\partial \Phi(\vec{x}(t_1))}{\partial \vec{x}} \tag{3.9}$$

$$\dot{\vec{\lambda}}(t) = -\frac{\partial H(\vec{x}(t),\vec{u}(t),t)}{\partial \vec{x}} = -\left(\frac{\partial L(\vec{x}(t),\vec{u}(t),t)}{\partial \vec{x}} + \vec{\lambda}(t) \cdot \frac{\partial f(\vec{x}(t),\vec{u}(t),t)}{\partial \vec{x}} \right) \tag{3.10}$$

which describe the dynamics of Lagrange multiplier, and the condition

$$\frac{\partial H(\vec{x}(t),\vec{u}(t),t)}{\partial \vec{u}} = \frac{\partial L(\vec{x}(t),\vec{u}(t),t)}{\partial \vec{u}} + \vec{\lambda}(t) \cdot \frac{\partial f(\vec{x}(t),\vec{u}(t),t)}{\partial \vec{u}} = 0 \tag{3.11}$$

which should be fulfilled for the optimal path.

In case of the non-optimal path

$$\frac{\partial H(\vec{x}(t),\vec{u}(t),t)}{\partial \vec{u}} \neq 0 \tag{3.12}$$

the following variation of the cost function is obtained

$$\begin{aligned} \delta J &= \int_{t_0}^{t_1} \left(\frac{\partial H(\vec{x}(t),\vec{u}(t),t)}{\partial \vec{u}} \delta u \right) dt \\ &= \int_{t_0}^{t_1} \left(\frac{\partial L(\vec{x}(t),\vec{u}(t),t)}{\partial \vec{u}} + \vec{\lambda}(t) \cdot \frac{\partial f(\vec{x}(t),\vec{u}(t),t)}{\partial \vec{u}} \right) \delta u dt \end{aligned} \tag{3.13}$$

By the following modification of the control variable $\vec{u}(t)$ to $\vec{u}'(t)$

$$\vec{u}'(t) = \vec{u}(t) - \epsilon \left(\frac{\partial L(\vec{x}(t),\vec{u}(t),t)}{\partial \vec{u}} + \vec{\lambda}(t) \cdot \frac{\partial f(\vec{x}(t),\vec{u}(t),t)}{\partial \vec{u}} \right) \tag{3.14}$$

and sufficiently small ϵ

$$\delta u = \vec{u}'(t) - \vec{u}(t) = -\epsilon \left(\frac{\partial L(\vec{x}(t),\vec{u}(t),t)}{\partial \vec{u}} + \vec{\lambda}(t) \cdot \frac{\partial f(\vec{x}(t),\vec{u}(t),t)}{\partial \vec{u}} \right) \tag{3.15}$$

the cost function is minimized

$$\delta J = -\epsilon \int_{t_0}^{t_1} \left(\frac{\partial L(\vec{x}(t),\vec{u}(t),t)}{\partial \vec{u}} + \vec{\lambda}(t) \cdot \frac{\partial f(\vec{x}(t),\vec{u}(t),t)}{\partial \vec{u}} \right)^2 dt \leq 0 \tag{3.16}$$

and thus the condition (3.5) is fulfilled.

Based on the obtained in Eq. (3.5) - (3.14) relations, an iterative approach for the cost function minimization can be defined. Therefore, the following algorithm for the finding of the optimal path is developed:

- **Initialization**
  1. definition of the dynamic equation $\dot{\vec{x}} = \vec{f}(\vec{x}(t),\vec{u}(t),t)$ and control variable $\vec{u}(t)$
  2. definition of the time interval t_0 to t_1
  3. design of the cost function J
  4. generating of the initial control variable $\vec{u}_{init}(t)$
- **Iteration**
  1. determination of Lagrange multiplier from the dynamic equations (3.9) and (3.10)
  2. adjustment of the control variable according to Eq. (3.14)

Once the condition (3.11) is satisfied, also the condition $\delta J = 0$ will be fulfilled. The optimal values $\vec{u}^*(t)$ are thus generated from the initial control variable $\vec{u}_{init}(t)$. Since the condition $\delta J = 0$ does not guarantee the global minimum of the cost function J, the algorithm may lead to the non-optimal result of a local minimum. Therefore, it is recommended to start the optimization algorithm several times with different initial control variables $\vec{u}_{init}(t)$ and to compare the cost functions of the obtained optimal paths $\vec{u}^*(t)$.

3.1.2 Optimal control theory for Bloch equations

OCT can be well applied on the dynamics of the MR signal. Considering the magnetization vector

$$\vec{M}(t) = (M_x,M_y,M_z) \tag{3.17}$$

in an external magnetic field $\vec{B}$, the x and y components of the magnetic field $\vec{B}$ can be controlled by the RF pulse using alternating field B_1 (see chapter 2.1.4). The z component remains constant B_0. As it was previously shown, the magnetization vector rotates about the external magnetic field with the angular frequency

$$\vec{\omega}(t) = \gamma\vec{B}(t) \quad , \ \vec{\omega}(t) = (\omega_x,\omega_y,\omega_z) \tag{3.18}$$

Suppose therefore that it is possible to control ω_x and ω_y by an RF pulse and $\omega_z = \gamma B_0$ remains constant.

Thus, according to Eq. (2.8), the magnetization dynamics can be described by

$$\begin{aligned}\frac{dM_x}{dt} &= \left[\vec{M}(t) \times \vec{\omega}(t)\right]_x - \frac{M_x}{T_2} \\ \frac{dM_y}{dt} &= \left[\vec{M}(t) \times \vec{\omega}(t)\right]_y - \frac{M_y}{T_2} \\ \frac{dM_z}{dt} &= \left[\vec{M}(t) \times \vec{\omega}(t)\right]_z - \frac{M_z - M_0}{T_1}\end{aligned} \tag{3.19}$$

The control variables are then ω_x and ω_y, as the parameters that can be influenced. For the further optimization, an appropriate cost function needs to be defined in a particular time interval t_0 to t_1. The final cost can be defined as

$$J_{fin} = -\left(\vec{M}(t_1) \cdot \vec{M}_{Target}\right) \tag{3.20}$$

with $\vec{M}_{Target}$ predefined target magnetization, which the algorithm will try to reach at time point t_1. For the running cost, it would be important not to generate high energy pulses, since these are difficult to implement. The following term

$$J_{run} = \frac{\alpha}{2} \int_{t_0}^{t_1} \left(\omega_x^2(t) + \omega_y^2(t)\right) dt \tag{3.21}$$

is proportional to the energy of the pulse ($E \propto \omega^2$) and should be therefore minimized.

For imaging pulse sequences, the total acquired MR signal, which is caused by the transverse magnetization, needs to be maximized. The sum of all the acquired signals can be described by

$$S = \frac{1}{n} \int_{t_0}^{t_1} \sum_{l}^{n} \delta(t - t_l) \cdot |M_T(t)|\, dt \tag{3.22}$$

Here $M_T(t)$ denotes the transverse magnetization ($M_T(t) = M_x(t) + jM_y(t)$), $\delta(t)$ the delta function, n ($n = \int_{t_0}^{t_1} \sum_l \delta(t - t_l) dt$) and t_l number of acquisitions and acquisition times, respectively.

The variations of MR signal can be defined as

$$\delta S = \frac{1}{n} \int_{t_0}^{t_1} \sum_l \delta(t - t_l) \cdot \left| M_T(t) - e^{j\varphi_l} \cdot \bar{M}_T \right| dt \tag{3.23}$$

with $\bar{M}_T$ mean of acquired M_T at time points t_l ($\bar{M}_T = \frac{1}{n} \int_{t_0}^{t_1} \sum_l \delta(t - t_l) \cdot |M_T(t)|\, dt$) and φ_l desired phase of the acquired signal. The total cost function is formed by the sum of all costs

$$\begin{aligned} J = & - \left(\vec{M}(t_1) \cdot \vec{M}_{Target} \right) + \frac{\alpha}{2} \int_{t_0}^{t_1} \left(\omega_x^2(t) + \omega_y^2(t) \right) dt \\ & - \frac{\beta_1}{n} \int_{t_0}^{t_1} \sum_l \delta(t - t_l) \cdot |M_T(t)|\, dt \\ & + \frac{\beta_2}{n} \int_{t_0}^{t_1} \sum_l \delta(t - t_l) \cdot \left| M_T(t) - e^{j\varphi_l} \cdot \bar{M}_T \right| dt \end{aligned} \tag{3.24}$$

with α, β_1 and β_2 the proportionality coefficients. By proper choice of these coefficients, the priority of the optimization between the terms of the total cost can be set. Higher coefficient means better results of minimization of the corresponding term, but results also usually in worse result for the other terms. The minus sign before some terms means that the corresponding cost should be maximized.

With the designed cost function, the dynamic equations of $\vec{\lambda}(t)$ can be derived according to Eq. (3.9)

$$\vec{\lambda}(t_1) = -\vec{M}_{Target} \tag{3.25}$$

and according to Eq. (3.10)

$$\begin{aligned}
\frac{d\lambda_x}{dt} =& \frac{\beta_1}{n}\frac{\sum\limits_l \delta(t-t_l)\cdot M_x(t)}{|M_T(t)|} - \frac{\beta_2}{n}\frac{\sum\limits_l \delta(t-t_l)\cdot Real(M_T(t)-e^{j\varphi_l}\cdot\bar{M}_T)}{\left|M_T(t)-e^{j\varphi_l}\cdot\bar{M}_T\right|} \\
&+ \left[\vec{\lambda}(t)\times\vec{\omega}(t)\right]_x + \frac{\lambda_x}{T_2} \\
\frac{d\lambda_y}{dt} =& \frac{\beta_1}{n}\frac{\sum\limits_l \delta(t-t_l)\cdot M_y(t)}{|M_T(t)|} - \frac{\beta_2}{n}\frac{\sum\limits_l \delta(t-t_l)\cdot Imag(M_T(t)-e^{j\varphi_l}\cdot\bar{M}_T)}{\left|M_T(t)-e^{j\varphi_l}\cdot\bar{M}_T\right|} \\
&+ \left[\vec{\lambda}(t)\times\vec{\omega}(t)\right]_y + \frac{\lambda_y}{T_2} \\
\frac{d\lambda_z}{dt} =& \left[\vec{\lambda}(t)\times\vec{\omega}(t)\right]_z + \frac{\lambda_z}{T_1}
\end{aligned} \tag{3.26}$$

as well as the modification of the control variables, that leads to the minimization of the cost function

$$\begin{aligned}
\omega'_x(t) &= \omega_x(t) - \epsilon\left(\alpha\omega_x(t) + \left[\vec{\lambda}(t)\times\vec{M}(t)\right]_x\right) \\
\omega'_y(t) &= \omega_y(t) - \epsilon\left(\alpha\omega_y(t) + \left[\vec{\lambda}(t)\times\vec{M}(t)\right]_y\right)
\end{aligned} \tag{3.27}$$

If the system is expanded to include additional magnetization vectors with particular CS offset and B_1 field inhomogeneity, the total magnetization can be expressed as

$$\vec{M} = \sum_k \sum_i \vec{M}^{i,k}(t) \tag{3.28}$$

with $\vec{M}^{i,k}$ the magnetization vector with i^{th} CS-index k^{th} B_1-index (Fig. 3.1).

$$\vec{M}^{i,k}(t) = \left(M_x^{i,k}(t), M_y^{i,k}(t), M_z^{i,k}(t)\right) \tag{3.29}$$

Similar to the one magnetization vector system, the angular frequencies of the magnetization vectors in the rotating about the axis z with $\omega_L = \gamma B_0$ coordinate system are given by

$$\vec{\omega}^{i,k}(t) = \gamma\vec{B}^{i,k}(t) = \left(\omega_x^k(t), \omega_y^k(t), \omega_z^i(t)\right) \tag{3.30}$$

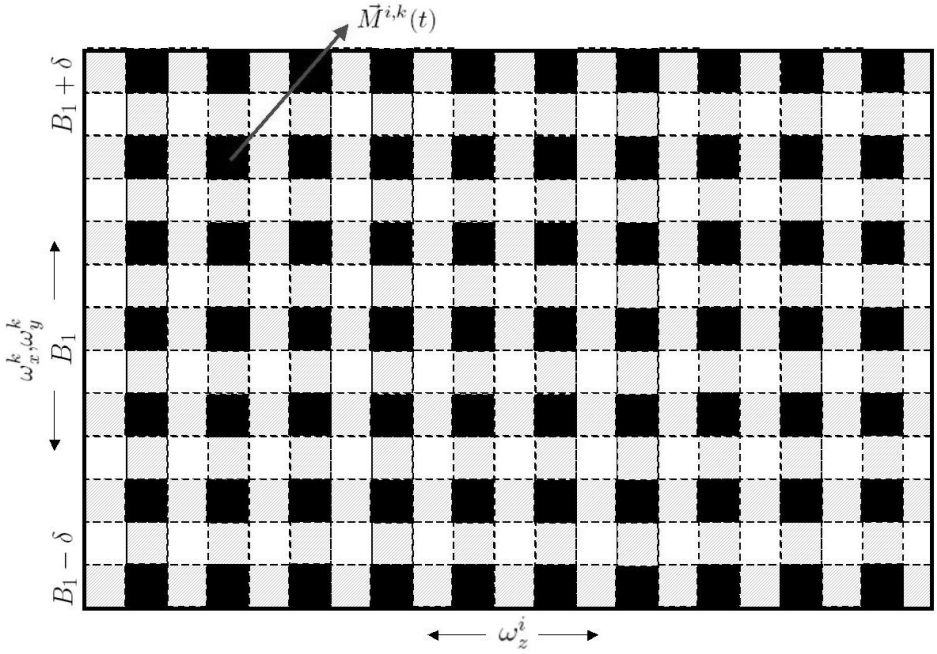

Figure 3.1: Discretization of the off-resonance ω_z^i and B_1 ($\omega_x(t)$, $\omega_y(t)$) field area. Each magnetization vector $\vec{M}^{i,k}(t)$ has its own Bloch equation according to $\vec{\omega}^{i,k}(t)$. The algorithm minimizes the cost function for all the magnetization vectors form the defined area.

with $\omega_x^k(t)$ and $\omega_y^k(t)$ control variables ($\propto B_{1,x}(t)$ and $B_{1,y}(t)$, respectively), and ω_z^i off-resonance of the i^{th} magnetization vector. And corresponding Lagrange multipliers are

$$\vec{\lambda}^{i,k}(t) = \left(\lambda_x^{i,k}(t),\lambda_y^{i,k}(t),\lambda_z^{i,k}(t)\right) \tag{3.31}$$

that means each Lagrange multiplier $\vec{\lambda}^{i,k}(t)$ corresponds to its individual magnetization vector $\vec{M}^{i,k}(t)$.

The dynamic equations are thus represented as

$$\begin{aligned}
\frac{dM_x^{i,k}}{dt} &= \left[\vec{M}^{i,k}(t) \times \vec{\omega}^{i,k}(t)\right]_x - \frac{M_x^{i,k}}{T_2} \\
\frac{dM_y^{i,k}}{dt} &= \left[\vec{M}^{i,k}(t) \times \vec{\omega}^{i,k}(t)\right]_y - \frac{M_y^{i,k}}{T_2} \\
\frac{dM_z^{i,k}}{dt} &= \left[\vec{M}^{i,k}(t) \times \vec{\omega}^{i,k}(t)\right]_z - \frac{M_z^{i,k} - M_0}{T_1}
\end{aligned} \tag{3.32}$$

and the total cost function is designed similar to Eq. (3.24)

$$\begin{aligned} J = &- \sum_k \sum_i \left(\vec{M}^{i,k}(t_1) \cdot \vec{M}_{Target} \right) + \sum_k \frac{\alpha}{2} \int_{t_0}^{t_1} \left((\omega_x^k(t))^2 + (\omega_y^k(t))^2 \right) dt \\ &- \sum_k \sum_i \frac{\beta_1^{i,k}}{n} \int_{t_0}^{t_1} \sum_l \delta(t - t_l) \cdot \left| M_T^{i,k}(t) \right| dt \\ &+ \sum_k \sum_i \frac{\beta_2^{i,k}}{n} \int_{t_0}^{t_1} \sum_l \delta(t - t_l) \cdot \left| M_T^{i,k}(t) - e^{j\varphi_l^{i,k}} \cdot \bar{M}_T^{i,k} \right| dt \end{aligned} \tag{3.33}$$

Thus, according to Eq. (3.9) and (3.10), following dynamic equations for $\vec{\lambda}^{i,k}(t)$ are derived

$$\vec{\lambda}^{i,k}(t_1) = -\vec{M}_{Target} \tag{3.34}$$

$$\begin{aligned} \frac{d\lambda_x^{i,k}}{dt} =& \frac{\beta_1^{i,k}}{n} \frac{\sum_l \delta(t - t_l) \cdot M_x^{i,k}(t)}{\left| M_T^{i,k}(t) \right|} - \frac{\beta_2^{i,k}}{n} \frac{\sum_l \delta(t - t_l) \cdot Real(M_T^{i,k}(t) - e^{j\varphi_l^{i,k}} \cdot \bar{M}_T^{i,k})}{\left| M_T^{i,k}(t) - e^{j\varphi_l^{i,k}} \cdot \bar{M}_T^{i,k} \right|} \\ &+ \left[\vec{\lambda}^{i,k}(t) \times \vec{\omega}^{i,k}(t) \right]_x + \frac{\lambda_x^{i,k}}{T_2} \\ \frac{d\lambda_y^{i,k}}{dt} =& \frac{\beta_1^{i,k}}{n} \frac{\sum_l \delta(t - t_l) \cdot M_y^{i,k}(t)}{\left| M_T^{i,k}(t) \right|} - \frac{\beta_2^{i,k}}{n} \frac{\sum_l \delta(t - t_l) \cdot Imag(M_T^{i,k}(t) - e^{j\varphi_l^{i,k}} \cdot \bar{M}_T^{i,k})}{\left| M_T^{i,k}(t) - e^{j\varphi_l^{i,k}} \cdot \bar{M}_T^{i,k} \right|} \\ &+ \left[\vec{\lambda}^{i,k}(t) \times \vec{\omega}^{i,k}(t) \right]_y + \frac{\lambda_y^{i,k}}{T_2} \\ \frac{d\lambda_z^{i,k}}{dt} =& \left[\vec{\lambda}^{i,k}(t) \times \vec{\omega}^{i,k}(t) \right]_z + \frac{\lambda_z^{i,k}}{T_1} \end{aligned} \tag{3.35}$$

and the required modification of the control variables for the minimization of the total cost function

$$\begin{aligned}\omega_x'^k(t) &= \omega_x^k(t) - \epsilon\left(\alpha\omega_x^k(t) + \left[\sum_k\sum_i\left(\vec{\lambda}^{i,k}(t)\times\vec{M}^{i,k}(t)\right)\right]_x\right)\\ \omega_y'^k(t) &= \omega_y^k(t) - \epsilon\left(\alpha\omega_y^k(t) + \left[\sum_k\sum_i\left(\vec{\lambda}^{i,k}(t)\times\vec{M}^{i,k}(t)\right)\right]_y\right)\end{aligned} \tag{3.36}$$

With the method described above the time evolution of the $\vec{B_1}(t)$ field, i.e. RF pulses, can be controlled and optimized. It is important to note, that the control variables ω_x and ω_y are allowed to be non-continuous, that is the typical case for RF pulses in practical MRI applications. Using the proposed optimization algorithm: i) the total magnetization $\vec{M}$ will be moved to the desired target state $\vec{M}_{Target}$, ii) the total energy required for the $\vec{B_1}(t)$ field excitation will be minimized, iii) the sum of the signals at specific time points t_l will be maximized, and iv) the variations of the amplitude and phase of the signal minimized. In other words, the result can be defined as an energetically favorable RF pulse sequence which generates stable echo train with a high total signal and brings the magnetization to the desired state.

3.1.3 Implementation

The described above optimization algorithm was implemented in MATLAB (according to Eq. (3.28) - (3.36)) and required following major programming steps:

- **Initialization**
  1. definition of the initial conditions $\vec{M}^{i,k}(t_0) = \left(M_x^{i,k}(t_0), M_y^{i,k}(t_0), M_z^{i,k}(t_0)\right)$, ω_z^i, $\vec{M}_{Target}$, ϵ
  2. discretization of the time interval t_0 to t_1: $t_p = t_0 + \frac{t_1 - t_0}{N}p$
  3. generating an initial control variables $\omega_x^k(t_p)$ and $\omega_y^k(t_p)$
- **Iteration**
  1. Computation of the total magnetization evolution $\vec{M}(t_p)$ according to Eq. (3.28) and (3.32) (propagation $\vec{M}^{i,k}(t_0) \rightarrow \vec{M}^{i,k}(t_1)$)
  2. Computation of the Lagrange multipliers dynamics $\vec{\lambda}^{i,k}(t_p)$ according to Eq. (3.34) and (3.35) (propagation $\vec{\lambda}^{i,k}(t_1) \rightarrow \vec{\lambda}^{i,k}(t_0)$)
  3. Modification of the control variables $\omega_x^k(t_p)$ and $\omega_y^k(t_p)$ according to Eq. (3.36)

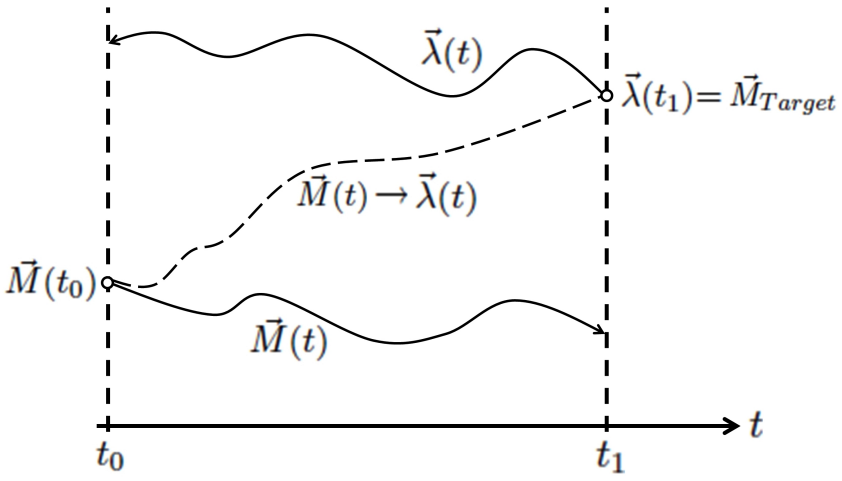

Figure 3.2: Optimization scheme: Propagation $\vec{M}(t_0) \rightarrow \vec{M}(t_1)$ and $\vec{\lambda}(t_1) \rightarrow \vec{\lambda}(t_0)$ for a given pulse sequence in order to achieve a particular target state $\vec{M}_{Target}$ [71].

For the computation, all differential equations were substituted by rotation matrices, which are more favorable in MATLAB programming environment. Neglecting the relaxation effects and assuming the control variables to be constant over a short time interval Δt (so-called hard pulse case) following analytical solution of Bloch equation $\frac{d\vec{M}}{dt} = \left[\vec{M} \times \vec{\omega}\right]$ can be derived [72]

$$\vec{M}(t + \Delta t) = \mathbf{R}(\Delta t)\vec{M(t)} \tag{3.37}$$

with rotation matrix $\mathbf{R}$=

$$\begin{pmatrix} cos\alpha + n_1^2(1 - cos\alpha) & n_1n_2(1 - cos\alpha) - n_3sin\alpha & n_1n_3(1 - cos\alpha) + n_2sin\alpha \\ n_2n_1(1 - cos\alpha) + n_3sin\alpha & cos\alpha + n_2^2(1 - cos\alpha) & n_2n_3(1 - cos\alpha) - n_1sin\alpha \\ n_3n_1(1 - cos\alpha) - n_2sin\alpha & n_3n_2(1 - cos\alpha) + n_1sin\alpha & cos\alpha + n_2^2(1 - cos\alpha) \end{pmatrix}$$

where $\alpha = \Delta t \cdot \sqrt{\omega_x^2 + \omega_y^2 + \omega_z^2}$ and $\vec{n} = (n_1,n_2,n_3) = \frac{\Delta t}{\alpha}(\omega_x,\omega_y,\omega_z)$

In order to use the rotation matrix solution for the dynamic equation of Lagrange multipliers, which in our case has following simplified form $\frac{d\vec{\lambda}}{dt} = \vec{S} + \left[\vec{\lambda} \times \vec{\omega}\right]$, following substitution was made

$$\vec{\lambda^*} = \vec{\lambda} - \vec{s} \quad with \quad [\vec{s} \times \vec{\omega}] = \vec{S} \tag{3.38}$$

which results in the mathematically identical to the Bloch equation form

$$\frac{d\vec{\lambda}^*}{dt} = \left[\vec{\lambda}^* \times \vec{\omega}\right] \tag{3.39}$$

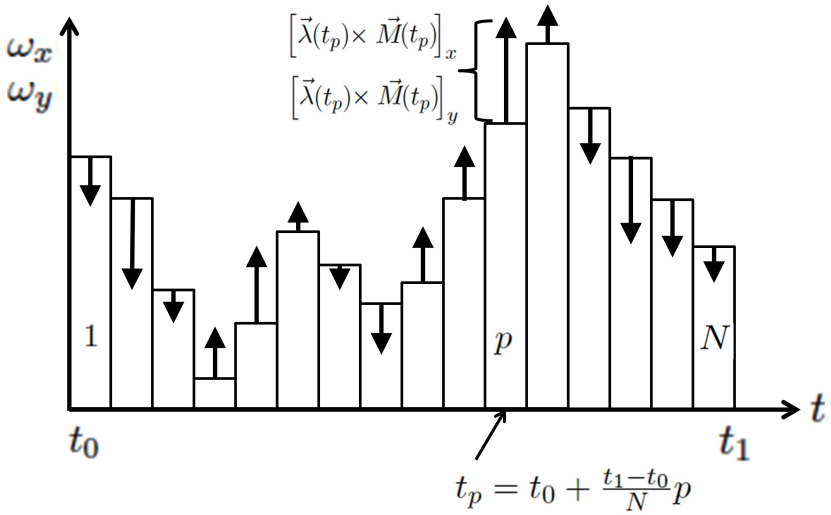

Figure 3.3: Schematic representation of the control variables $\omega_x(t)$ and $\omega_y(t)$ consisting of N steps with a discretization time of $\Delta t = \frac{t_1-t_0}{N}$. At each step p the control variable is constant. The vertical arrows show how each amplitude should be changed according to the Eq. (3.36) [73].

The use of rotation matrices reduced the computational time by a factor of about 15 compared to the commonly used MATLAB differential equation solver ode45. The optimization algorithm is schematically illustrated in Fig. 3.2 and 3.3. The iteration is repeated until the change in the total cost function ΔJ after one iteration step is less than a pre-determined limit ΔJ_{limit}. The choice of the constant ϵ depends on the system parameters. Using small ϵ results in more iteration steps and thus the computation time is longer. The larger values of ϵ can lead to instability and non-convergence of the algorithm. It is also possible to define differing ϵ, which decreases with the number of iterations till particular minimal value, in order to find first a rough solution and to refine it at the later iteration steps. Also the algorithm can be further improved by using conjugation of ϵ or by using quasi-Newton methods.

3.2 Spectral fitting

Estimation of metabolic conversion rates requires beforehand accurate spectral fitting of the acquired signal. For this purpose, a user independent fully automatic spectral fitting method for hyperpolarized ^{13}C MRS was developed, which utilizes the specific properties of the ^{13}C spectra.

3.2.1 Hyperpolarized FID signal model

In comparison to standard thermal-equilibrium-based spectroscopy, spectral fitting of hyperpolarized ^{13}C signals is simplified by i) a missing macromolecular baseline background and ii) a sparse signal spectrum of typically well-separated singlet peaks. Accordingly, measured time-discretized FID signals $s_n = s(t_n)$ were expressed as a summation over the metabolic basis spectra F_{nm}:

$$s_n = \sum_m a_m F_{nm} \tag{3.40}$$

with

$$F_{nm} = exp(-\alpha_m t_n^{r_m} + i\omega_m t_n) \tag{3.41}$$

Here, t_n denotes the sampling time, a_m the individual metabolite signal amplitude, ω_m CS frequency, α_m and r_m line shape parameters of the metabolite basis spectra (α_m mainly dependent on the effective transverse relaxation time of metabolite $T^*_{2,m}$ and r_m =1 or 2 corresponding to Lorentzian or Gaussian line shapes, respectively). For the typical case of more samples than unknown metabolites Eq. (3.41) describes an over-determined system that can be efficiently solved using algebraic methods ([74],[75]). The construction of the **F** matrix requires prior knowledge of the $\{\omega_m, \alpha_m, r_m\}$ parameters, which were estimated in a preprocessing step from the spectra corresponding to the measured FIDs, as explained in the next section.

3.2.2 Matching pursuit spectral decomposition

Matching pursuit is an iterative method to decompose a signal into the main constituents of a given complete set of basis functions (so-called dictionary). It is known to provide sparse approximations of input signals in terms of the provided dictionary ([76],[77]). Here the method was used to automatically extract the

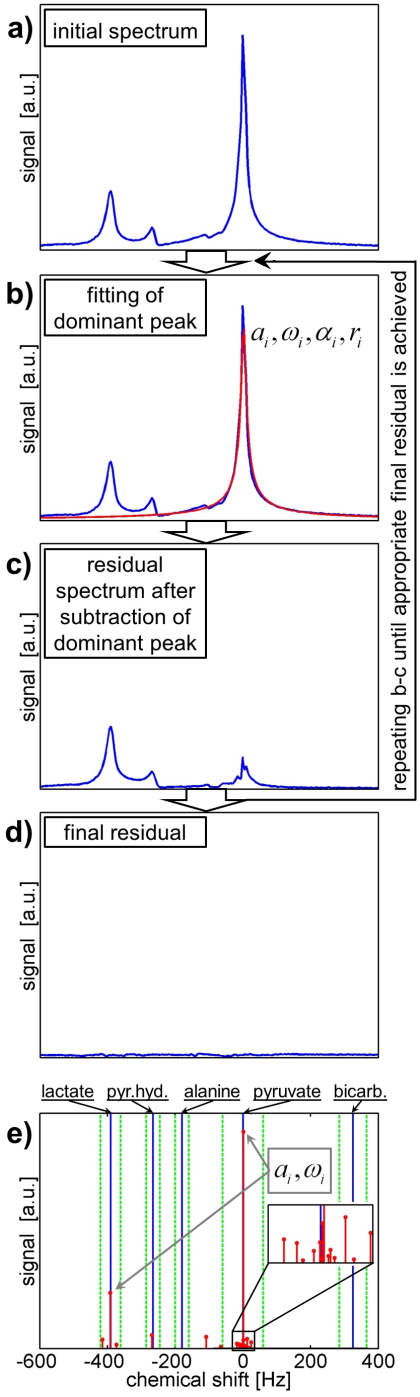

Figure 3.4: Exemplary schematic representation of spectral fitting using the matching pursuit algorithm (a-d). e) Sparse representation of initial spectrum (red circles show obtained amplitudes and frequencies $\{a_i, \omega_i\}$) together with expected metabolite CS frequencies (blue lines) and predefined frequency intervals (green lines).

$\{\omega_m, \alpha_m, r_m\}$ parameters required for the construction of the **F** matrix (3.41). The used dictionary was formed by an overcomplete set of basis spectra with variable parameters $\{\omega_i, \alpha_i, r_i\}$ defining the search space. In each iteration k, the basis spectra were tested and the spectrum resulting in the lowest residuum

$$\underset{a_i,\omega_i,\alpha_i,r_i}{min} \|s_k(t_n) - a_i exp(-\alpha_i t_n^{r_i} + i\omega_i t_n)\| \tag{3.42}$$

was retained and subtracted to form the input for the next iteration

$$s_{k+1}(t_n) = s_k(t_n) - a_i exp(-\alpha_i t_n^{r_i} + i\omega_i t_n) \tag{3.43}$$

Hence, the obtained decomposition represented a sparse approximation of the spectrum with $\{a_i, \omega_i, \alpha_i, r_i\}$ the amplitudes, CS frequencies and line shape parameters of the found basis spectra (Fig. 3.4). For the considered case of dynamic measurements, the procedure was repeated for all individual FIDs to improve sensitivity.

In the implemented processing, the CS spectrum was first centered at the dominant peak, which was assigned to be pyruvate. Prior knowledge of the approximate relative CS frequencies of the pyruvate downstream metabolites was then used to assign each metabolite a particular frequency band within the spectrum. For each metabolite, the parameters $\{\omega_m, \alpha_m, r_m\}$ were calculated based on an amplitude-weighted average of the basis spectra parameters $\{\omega_i, \alpha_i, r_i\}$ contained in the respective frequency band. The line shape parameters r_m were rounded to describe either Lorentzian ($r_m = 1$) or Gaussian ($r_m = 2$) distributions. The frequency bands of lactate, alanine, pyruvate hydrate, and bicarbonate were defined at -390 ± 30, -180 ± 20, -265 ± 20 and $+325 \pm 40$ Hz relative to pyruvate at 0 ± 60 Hz.

3.2.3 Linear least-squares, time-domain spectral fitting

Spectral fitting of metabolite amplitudes a_m can be considered as the solution of the inverse problem defined by the matrix equation (3.41). For the typical case of more FID samples than unknown metabolite constituents, this describes an overdetermined system that can be solved in a weighted linear least squares sense using the Moore-Penrose pseudo-inverse according to

$$\mathbf{a} = (\mathbf{F}^H \mathbf{W} \mathbf{F})^{-1} \mathbf{F}^H \mathbf{W} \mathbf{s} \tag{3.44}$$

with the superscript H the complex conjugate operator, and $\mathbf{W}$ an optional, diagonal weighting matrix. In order to increase the detectability of low amplitude signals next to a dominant pyruvate peak (i.e. to reduce CS aliasing), the pyruvate resonance can also be approximated by more than a single spectral component.

3.3 Kinetic modelling

For widespread use in medicine, standardization of the analysis of [1-^{13}C]pyruvate kinetics and its downstream metabolites will be required. Initially, the metabolite ratios were used as metrics for the comparison of various effects ([26],[29]). An alternative to the lactate to pyruvate ratio, which is critically dependent on the timing of injection and subsequent data acquisition, is to measure the lactate and pyruvate signals over time and fit these to a kinetic model ([20],[23],[25]).

3.3.1 Two-site exchange kinetic modeling

The spectrally fitted metabolite time signals a_m (see chapters 3.2.1.-3.2.2.) were used to derive apparent rate constants characterizing metabolite exchange and signal decay. In case of hyperpolarized pyruvate the signal dynamics was described by a two-site exchange model including the pyruvate substrate *pyr* and a single metabolic product m (Fig. 3.5).

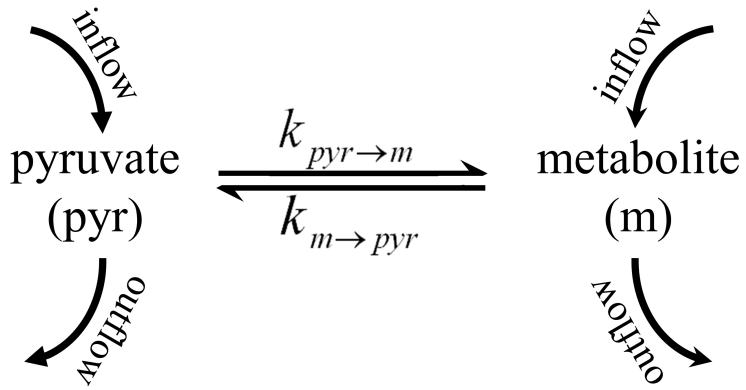

Figure 3.5: Schematic of a two-site exchange model of pyruvate metabolism.

According to this model the time evolution of metabolite m concentration c_m is dependent on pyruvate concentration c_{pyr}

$$\frac{dc_m}{dt} = +k_{pyr\rightarrow m}c_{pyr} - k_{m\rightarrow pyr}c_m \tag{3.45}$$

with $k_{pyr\rightarrow m}$ and $k_{m\rightarrow pyr}$ denoting the apparent build-up and depletion rates of metabolite m, respectively, including enzymatically driven conversion as well as transport effects. The apparent rates were assumed to be constant during the experiment time period. The estimated metabolite time signals a_m represent the transverse component of the metabolite signal intensities and are therefore proportional to the metabolite concentration c_m with a factor, which depends on local flip angle and polarization at the acquisition time and is constant for all metabolites during one time step. Thus, the proposed kinetic model accounts for forward ($k_{pyr\rightarrow m}$) and backward ($k_{m\rightarrow pyr}$) conversion and needs to be corrected by signal decay mechanisms due to T_1 relaxation and repetitive excitation. In a time-discretized formulation this led to the following rate equation:

$$\frac{\Delta a_{m,k}}{T_k} = +k_{pyr\rightarrow m}a_{pyr,k} - \frac{a_{m,k}}{T_{1,m}} - \frac{1-cos(\beta_k)}{T_k}a_{m,k} - k_{m\rightarrow pyr}a_{m,k} \tag{3.46}$$

with T_k and β_k as the time increment and the effective flip angle of the k^{th} measurement point, respectively. Summarizing the contributions proportional to $a_{m,k}$ and $a_{pyr,k}$ and considering a constant repetition time ($T_k = \Delta t$) and flip angle, the above equation was simplified to

$$\frac{\Delta a_{m,k}}{\Delta t} = +k_{pyr\rightarrow m}a_{pyr,k} - R_{eff,m}a_{m,k} \tag{3.47}$$

with the effective decay rate, $R_{eff,m} = 1/T_{1,m} + [1-cos(\beta_k)]/\Delta t + k_{m\rightarrow pyr}$, accounting for the signal decay effects due to T_1 relaxation, repetitive excitation, and backward conversion. This equation was solved for the unknown apparent build up rate $k_{pyr\rightarrow m}$ and the effective decay rate $R_{eff,m}$ using either time or frequency domain analysis.

3.3.2 Time-domain fitting of kinetic model

Given time-resolved metabolite signals, Eq. (3.47) results in an over-determined system of linear equations for $k_{pyr\rightarrow m}$ and $R_{eff,m}$:

$$\begin{pmatrix} \frac{\Delta a_{m,1}}{\Delta t} \\ \vdots \\ \frac{\Delta a_{m,K}}{\Delta t} \end{pmatrix} = \begin{pmatrix} -a_{m,1} & -a_{pyr,1} \\ \vdots & \vdots \\ -a_{m,K} & -a_{pyr,K} \end{pmatrix} \begin{pmatrix} R_{eff,m} \\ k_{pyr\rightarrow m} \end{pmatrix}$$

which can be solved using the Moore-Penrose pseudo-inverse similar to as discussed in the context of Eq. (3.44).

3.3.3 Frequency-domain fitting of kinetic model

Transforming Eq. (3.47) from time to frequency domain results in the following equation

$$i\Omega_n \tilde{a}_{m,n} = +k_{pyr\to m}\tilde{a}_{pyr,n} - R_{eff,m}\tilde{a}_{m,n} \tag{3.48}$$

with $\tilde{a}_{m,n} = \sum_{k=1}^{K} a_{m,k} exp(i\Omega_n k \cdot \Delta t) \cdot \Delta t$ and $\tilde{a}_{pyr,n} = \sum_{k=1}^{K} a_{pyr,k} exp(i\Omega_n k \cdot \Delta t) \cdot \Delta t$ the discrete-time Fourier transforms of $a_{m,k}$ and $a_{pyr,k}$, respectively. Equation (3.48) describes an over-determined system of linear equations similar to the time-domain one described above. Interestingly, for $\Omega_n = 0$, Eq. (3.48) provides a clear physical interpretation of the often used ratio of time-integrated metabolite signals:

$$\frac{\sum_{k=1}^{K} a_{m,k}}{\sum_{k=1}^{K} a_{pyr,k}} = \frac{\tilde{a}_m(\Omega_n = 0)}{\tilde{a}_{pyr}(\Omega_n = 0)} = \frac{k_{pyr\to m}}{R_{eff,m}} \tag{3.49}$$

Furthermore, this identity of DC (zero frequency component) signal ratios can be used to derive analytical expressions for $k_{pyr\to m}$ and $R_{eff,m}$ according to:

$$k_{pyr\to m} = i\Omega_n \frac{\tilde{a}_m(\Omega_n = 0) \cdot \tilde{a}_{m,n}(\Omega_n)}{\tilde{a}_m(\Omega_n = 0) \cdot \tilde{a}_{pyr,n}(\Omega_n) - \tilde{a}_{pyr}(\Omega_n = 0) \cdot \tilde{a}_{m,n}(\Omega_n)} \tag{3.50}$$

and

$$R_{eff,m} = i\Omega_n \frac{\tilde{a}_m(\Omega_n = 0) \cdot \tilde{a}_{pyr,n}(\Omega_n)}{\tilde{a}_m(\Omega_n = 0) \cdot \tilde{a}_{pyr,n}(\Omega_n) - \tilde{a}_{pyr}(\Omega_n = 0) \cdot \tilde{a}_{m,n}(\Omega_n)} \tag{3.51}$$

Both time and frequency domain methods have advantages and disadvantages. The time-domain fitting can be applied to any time window of the signal, while for the frequency domain fitting, the entire signal acquisition is required, from the pyruvate arrival until the hyperpolarized signal is completely decayed. The main advantage of the frequency domain description is the avoidance of an explicit time differentiation, which generally results in noise amplification. Conceptually, the proposed kinetic model accounts for variable inflow and outflow of pyruvate but

assumes them to be the same (or negligible) for the metabolic product m. In comparison to previously presented methods, this formulation decouples the kinetics between pyruvate and its metabolic products into single differential equations. As a consequence, in the presented description, no explicit arterial input function is required, as it is implicitly contained in the pyruvate signals. Note that this formulation does not allow resolving the effective decay rate into its individual contributions as listed in the context of Eq. (3.47).

3.4 Chemical shift imaging

Fast spectroscopic imaging techniques (or chemical shift imaging (CSI)) enable spatially resolved dynamic data acquisition of variable uptake and metabolism of hyperpolarized compounds. Therefore, it allows for further spatially resolved quantification of metabolic fluxes. The majority of CSI techniques, e.g. the inversion recovery method, chemical shift selective imaging sequence and the saturation method, were developed for proton imaging and do not account for the non-reversible polarization as in case of hyperpolarization. Hence, an efficient and robust imaging method needed to be developed.

3.4.1 IDEAL spiral CSI

The spectral-spatial IDEAL spiral CSI ([37],[78]) enables information encoding from five dimensions including CS, three spatial dimensions and time. This imaging method is implemented by single-shot spiral image acquisition and echo time shifting combined with spectrally-preconditioned, minimum-norm CS inversion (Fig. 3.6). Starting with FID and followed by P single shot spiral acquisitions with different echo times (TE_p), the acquired data for the p^{th} echo time and n^{th} time point can be expressed in k-space as

$$\mathbf{d}_n = \sum_{m=1}^{M} A_{p,m} a'_m(\mathbf{k}_n) \tag{3.52}$$

with $\mathbf{d}_n = \begin{pmatrix} d_1(t_n) \\ \vdots \\ d_P(t_n) \end{pmatrix}$ signal vector, $\mathbf{k}_n$ k-space location at time point t_n, $a'_m(\mathbf{k}_n)$ metabolite signals in k-space domain and A chemical shift matrix with elements

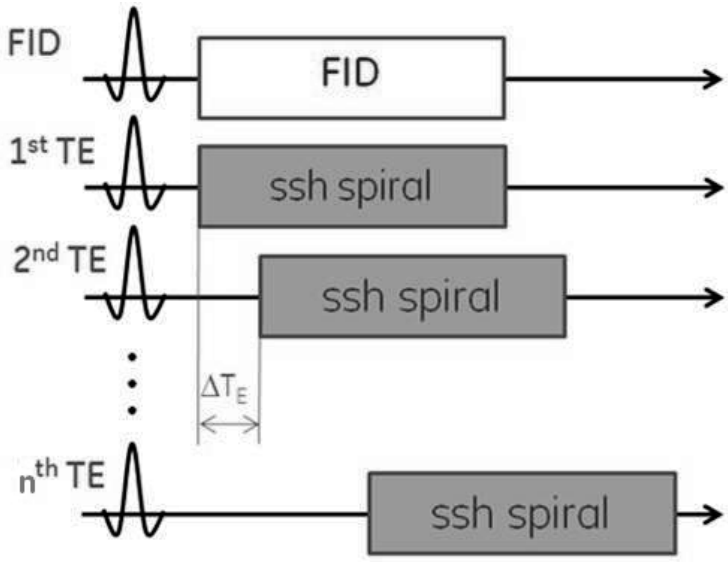

Figure 3.6: Illustration of IDEAL spiral CSI. Each excitation is followed by a single-shot imaging module (gray boxes) and the spectral encoding is achieved via echo time shifting from excitation to excitation. Additionally, a FID acquisition is performed at the beginning which provides spectral prior knowledge for the reconstruction.

$A_{p,m} = exp(i\omega_m TE_p)$. The initial FID is used in the reconstruction as spectral prior knowledge to precondition the further chemical shift inversion using matching pursuit algorithm. For the image reconstruction of IDEAL spiral CSI acquired data the metabolite signals in k-space domain can be initially estimated with Moore-Penrose pseudo-inverse $a'_m(\mathbf{k}_n) = A^H \mathbf{d}_n$ Afterwards spatially resolved metabolite signals are obtained using fast Fourier transform and gridding reconstruction along the spiral trajectory $a_m(\mathbf{r}) = FFT\{Gridding(a'_m(\mathbf{k}_n))\}$.

4 Experiments

4.1 Hyperpolarization

The sample mixture for polarization contained 14 M [1-^{13}C]pyruvic acid (Cambridge Isotope Laboratories, Andover, MA, USA) doped with 15 mM OXO63 trityl radical (Oxford Instruments, Abingdon, UK) and 10 mM Dotarem (Guerbet, Villeprinte, France). The sample was polarized in the solid state at 1.4 K and 3.35 T for approximately 45 min using a HyperSense DNP polarizer (Oxford Instruments, Abingdon, UK) (Fig. 4.1). The dissolution agent, containing 20 mM NaOH, 20 mM TRIS buffer, and 0.025 g/L Na2-EDTA or containing 80 mM NaOH, 80 mM TRIS buffer, and 0.1 g/L Na2-EDTA dissolved in water for in vitro or in vivo experiments, respectively, was heated to 185 °C and flushed the polarized sample at 10 bar. The final injectable solution contained 20 mM (for in vitro) or 80 mM (for in vivo) hyperpolarized [1-^{13}C]pyruvate with a pH value of 7.6. The liquid state polarization was measured immediately following the dissolution using a Minispec mq40 NMR analyzer (Bruker Optik, Ettlingen, Germany) and was found to be between 20 % and 30 %. The time delay between dissolution and injection was 15 - 20 s.

4.2 Experimental setup

All experiments were performed on a 3 T GE Signa HDx MRI scanner (GE Healthcare, Milwaukee, WI, USA). For in vitro experiments, an optimized experimental setup was developed allowing measurement of pyruvate metabolism in a clinical MRI scanner. It retained stable conditions of the probe and provided higher SNR compared to the standard MR equipment. A schematic of this experimental setup is shown in Fig. 4.2. The NMR tube (8 mm diameter) containing a probe

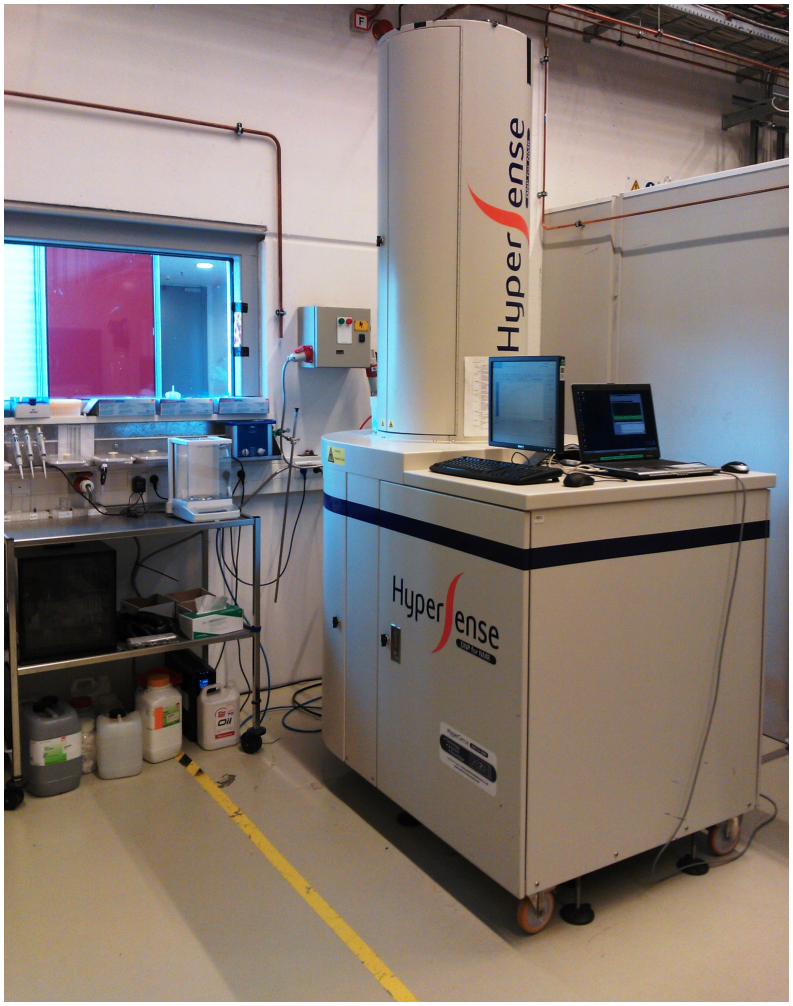

Figure 4.1: HyperSense DNP polarizer lab for preparation of hyperpolarized compounds.

of e.g. enzyme mixture or tumor cells suspension was inserted into a custom-built solenoid coil surrounded by a heating module containing circulating warm water (adapted from animal warming system, Gaymar Industries, Orchard Park, NY, USA). The temperature of the probe was adjustable and remained stable (37 °C) during the experiment. In order to improve the T_2^* linewidth, susceptibility-matched plugs and NMR tubes (Doty Scientific, Columbia, SC, USA) were used.

The solenoid transmit-receive ^{13}C coil was designed and optimized for 2mL sample volume. The coil had 11 mm in diameter and 50 mm in length and was made of 9 turns of copper wire (diameter = 1.5 mm) divided in three equal parts. The

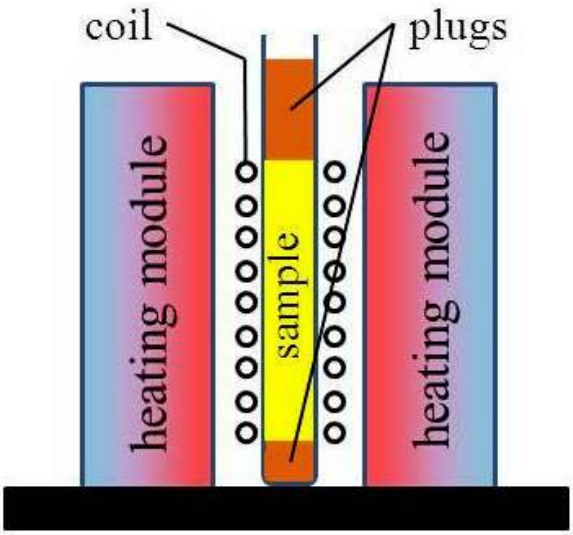

Figure 4.2: Schematic construction of the experimental setup for in vitro experiments.

electrical circuit of the coil is shown in Fig. 4.4. The whole experimental setup was placed into an MRI scanner.

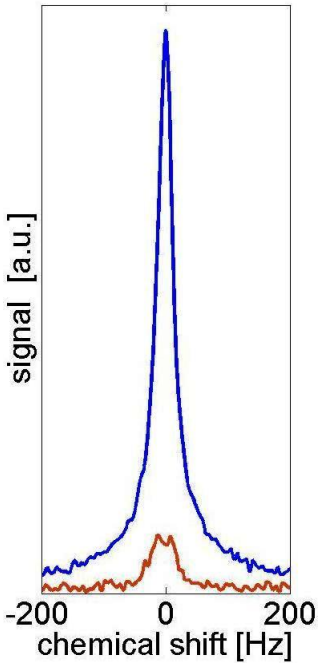

Figure 4.3: Spectrum of 2 mL ^{13}C-acetate acquired by ^{13}C volume coil (red) and optimized experimental setup (blue).

In order to compare the proposed setup with measurements using a dual-tuned

^{1}H-^{13}C volume coil [79], a phantom with highly concentrated thermally polarized ^{13}C-acetate was used. The spectrum of 2 mL acetate in round-bottom flask was acquired by the volume coil and is illustrated in Fig. 4.3 together with the spectrum of the same amount of acetate in NMR tube measured by the proposed solenoid coil. With the new optimized experimental setup, the SNR was improved approx. tenfold while susceptibility artifacts were significantly reduced compared to measurements using a dual-tuned ^{1}H-^{13}C volume coil. The increased sensitivity of the custom built solenoid coil allowed even spectral resolution of J-coupling of pyruvate ($\approx$ 4 Hz at 3 T) or detection of radiation damping effects (by injecting larger volume of hyperpolarized substance) in the clinical MR scanner.

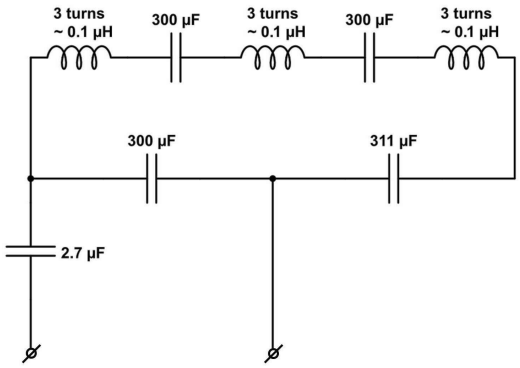

Figure 4.4: Schematic diagram of the electrical circuit of the solenoid transmit-receive ^{13}C coil.

4.3 In vitro LDH enzyme mixture experiments

Pyruvate was dissolved to a concentration of 20 mM and injected into the prepared in vitro sample, which was either an LDH enzyme mixture or tumor cell suspension. The LDH enzyme mixture consisted of coenzyme NADH and LDH enzyme (Sigma-Aldrich Corp, Saint Louis, MO, USA) dissolved in TRIS buffer (pH 7.6). Different combinations of final concentrations of pyruvate, NADH and LDH were tested in order to validate the proposed spectral and kinetic fitting methods. Data were acquired for about 3 min after the injection, with a custom-built (described above), solenoid transmit-receive ^{13}C coil using dynamic FID measurements (flip angle $\alpha = 5°$, repetition time $TR = 1$ s, 5 kHz acquisition bandwidth).

4.4 In vitro MCF-7 tumor cells experiments

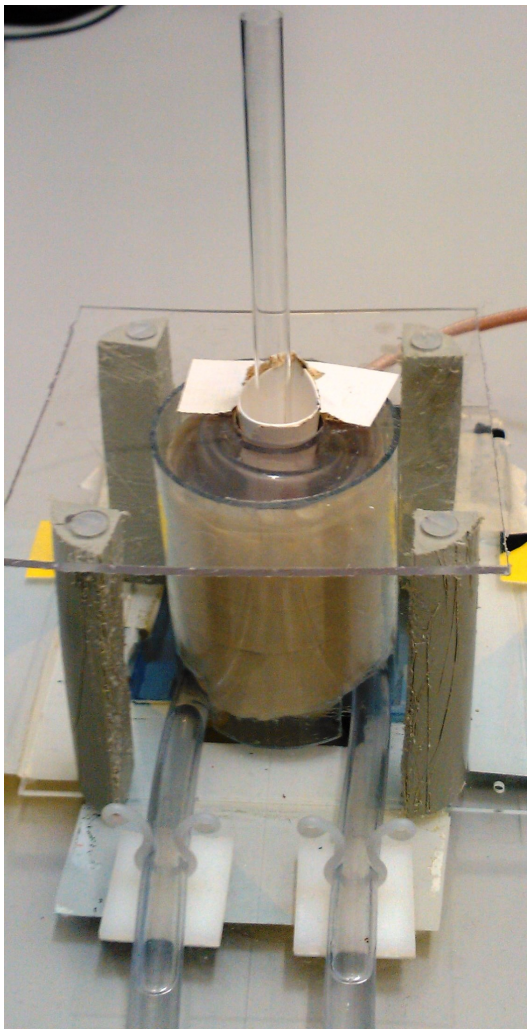

Figure 4.5: Experimental setup for in vitro experiments.

For the tumor cell experiments (Fig. 4.5), 100 μl of 20 mM hyperpolarized pyruvate were injected into the spheroid suspension, representing 10^8 cells of the breast cancer cell line MCF-7 maintained in Dulbecco's Modified Eagle's Medium (DMEM), supplemented with 25 mM glucose, 4 mM glutamine and 5 % fetal calf serum (pH 7.4). Dynamic FID ($\alpha = 20°$, $TR = 2$ s, 5 kHz acquisition bandwidth) were measured using the same solenoid transmit-receive ^{13}C coil. The final concentration of pyruvate in the tumor cell spheroid suspension was chosen to be similar to the pyruvate concentration in blood during in vivo experiments (about 0.2-0.4 mM).

4.5 In vivo experiments with surface coil

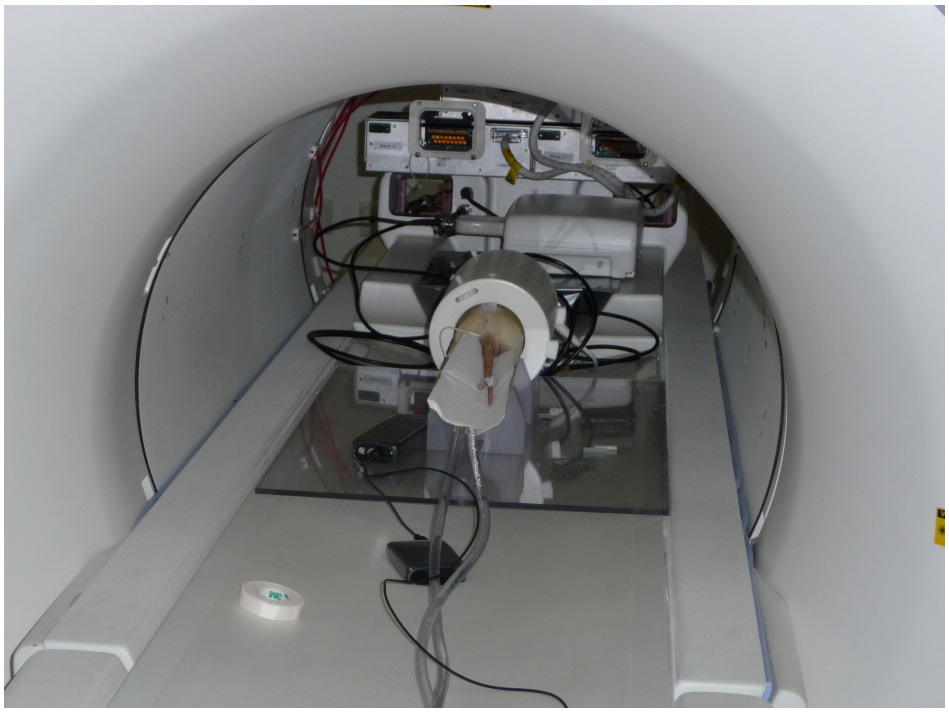

Figure 4.6: Example of the positioning of the rat for imaging experiment.

For the animal experiments, 80 mM pyruvate solution at a dosage of 0.2 mmol/kg body mass was injected inside the MRI scanner at a rate of approximately 0.2 mL/s into the tail vein of four adult female Fischer 344 rats (Charles River, Sulzfeld, Germany; 165 ± 6 g body weight) bearing subcutaneous mammary adenocarcinomas (Fig. 4.6). Tumors were induced by implanting 10^6 MAT B III cells (syngenic breast cancer cell line), and were imaged 12-16 days after cell implantation. The animal's anesthesia was maintained with 1-3 % isofluorane in oxygen starting about 1 h before the first injection. During the experiment, the heart rate, temperature and breathing signal were monitored using an animal monitoring system (SA Instruments, Stony Brook, NY, USA). All animal experiments were approved by the regional governmental commission for animal protection (Regierung von Oberbayern, Munich, Germany).

Slice-selective FID measurements were performed for 2 min following the injection of hyperpolarized pyruvate ($\alpha = 10°$, $TR = 1$ s, 5 kHz acquisition bandwidth). A single, 10 mm thick axial slice was carefully aligned to cover the subcutaneous tu-

mor. Spin excitation and signal reception were performed using a transmit-receive ^{13}C loop coil (diameter = 20 mm) placed around the subcutaneous tumor. The selective coil placement together with its localized sensitivity provided a ^{13}C signal primarily from the tumor region.

4.6 In vivo IDEAL spiral CSI experiments

Figure 4.7: Exemplary planning of the imaging geometry for multislice IDEAL spiral CSI experiments. The central slice (e.g. slice #3) was placed to cross the tumor.

For spatially and temporally resolved spectroscopy, IDEAL spiral CSI was used as described in chapter 3.4.1. consisting of 7 echo time shifted (TE = 1.12 ms) singe-shot spirals ($\alpha = 10°$, TR = 500 ms, FOV = 80 mm, nominal matrix resolution of 32×32, 62.5 kHz acquisition bandwidth, 45 ms readout) plus one additional FID acquisition. This allowed dynamic, multislice (4 slices, 10 mm thickness) CS imaging at a temporal resolution of 4 s. The exemplary planning of the imaging geometry is shown in Fig. 4.7. A syringe containing [1-^{13}C]lactate was used as

a reference for both ^{13}C and proton images. Image reconstruction was performed based on CS inversion followed by gridding reconstruction as described in [37]. The required CS frequencies were extracted from the FID measurements using the matching pursuit algorithm. In the post-processing, Gaussian k-space filtering was applied, resulting in an effective image resolution of 5×5 mm^2. For anatomical referencing of the ^{13}C metabolic images, standard gradient echo images were acquired from the same slice geometry.

5 Results

5.1 Pulse sequence optimization

Theoretically, the developed optimization algorithm allows to control the magnetization by any active RF pulse in the pulse sequence. In this work, the main focus was laid on the preparation of the magnetization for further data acquisition with fast imaging pulse sequences, such as SSFP, CPMG and non-CPMG (see chapter 2.2.5), in the presence of B_1 field inhomogeneity and for a predefined off-resonance offset. In the following, results of pulse sequence optimization are shown for the off-resonance offset of -200 to 200 Hz and the range of B_1 field inhomogeneity of $\approx \pm$ 16 %, that results in a $\pm$ 30° error of 180° refocusing pulse. The discretization steps of 20 Hz and 3° were applied, which resulted in 20×20 resolution matrix. The pulses were assumed to be hard pulses with pulse width of 100 μs and the repetition time TR for signal acquisition was 10 ms. These values correspond well to the real parameters for fast MRI. The optimization was performed for the case of hyperpolarized signal, which means high initial magnetization (was normalized to 1 for the simplicity) and neglectable relaxation processes (these were neglected only during the active RF pulse allowing the use of rotation matrices instead of solving differential equations; for the magnetization evolution between the pulses typical values of pyruvate relaxation times T_1 and T_2 of 30 s and 2 s, respectively, were used).

Figure 5.1 shows an exemplary result of the optimization of 7 equidistant preparation pulses for the following echo train with 48 180° refocusing pulses of SSFP pulse sequence. The cost function was designed to maximize the total acquisition signal and reduce the variation of signals during the echo train as described in chapter 3.1.2, which were also used as visualization metrics of the results. The energy minimization and target magnetization terms from Eq. (3.24) were neglected. Starting with arbitrary initial 7 preparation pulses, the algorithm provided appro-

priate optimization result for the given offset. The schematic diagram of the pulse sequence and the evolution of the total cost function are shown in Fig. 5.2. The components of the RF pulse amplitude are expressed in degrees of the flip angle according to Eq. (2.18), which means RF amplitude for the 180° pulse of 5 kHz.

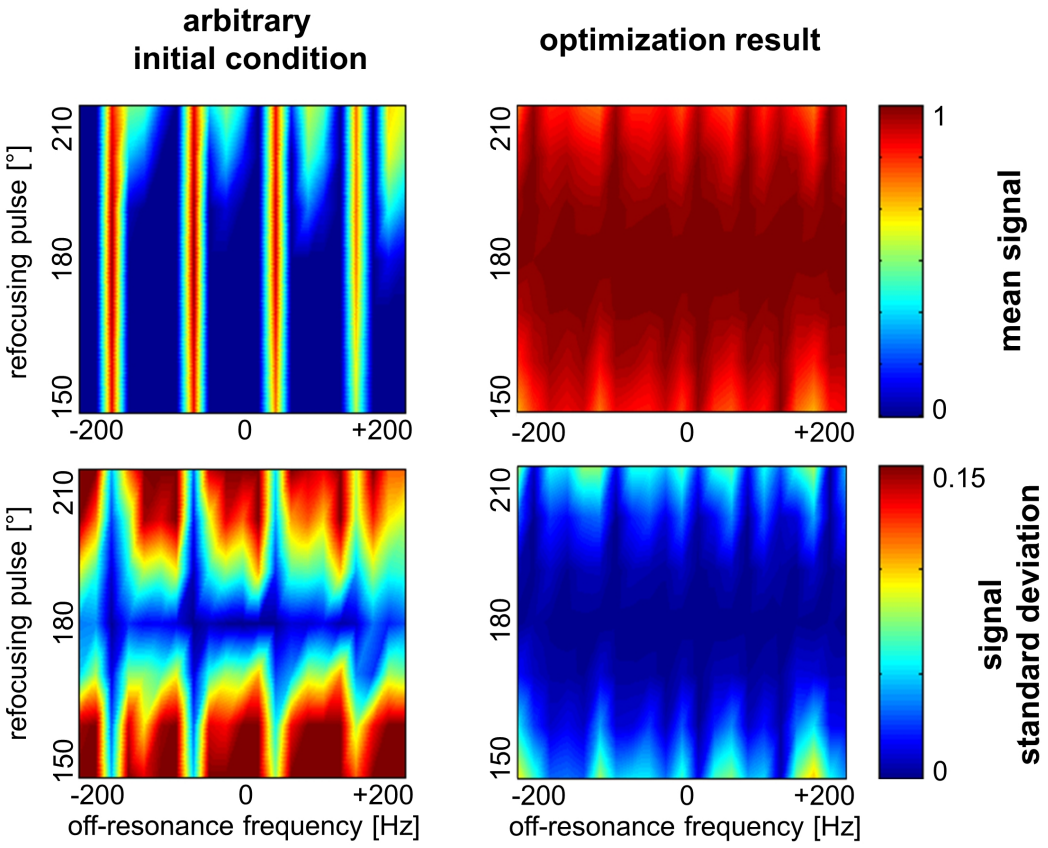

Figure 5.1: Result of the optimization (right) of 7 preparation pulses (PW = 100 μs) for the SSFP pulse sequence with 180° refocusing pulses (TR = 10 ms) compared to the initial arbitrary preparation pulses (left). Data are shown as mean of the signal (top) and its standard deviation (bottom) over 48 acquisitions after preparation period for the off-resonance offset of -200 to 200 Hz and B_1 inhomogeneity resulting in ±30° error of refocusing pulses.

Similar result was obtained by optimization of the non-CPMG pulse sequence (with quadratic phase modulation of refocusing pulses) with the same parameters (Fig. 5.3). These results confirm that non-CPMG and SSFP pulse sequences could be well applicable for the hyperpolarized MRI.

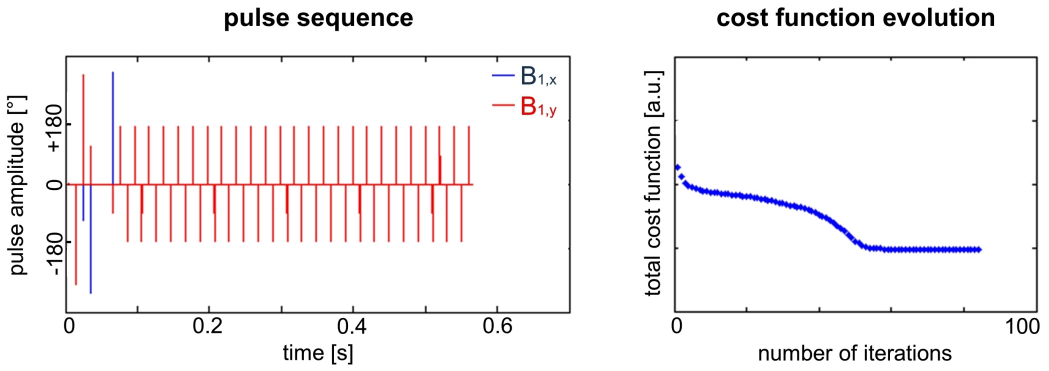

Figure 5.2: Pulse sequence diagram (left) of the SSFP pulse sequence with 7 optimized preparation (some pulses have near zero amplitude) and 48 refocusing pulses (cf. Fig. 5.1). Blue and red lines in the left figure show the x and y components of the RF pulse amplitude expressed in degrees of the flip angle. The evolution and convergence of the total cost function are shown on the right.

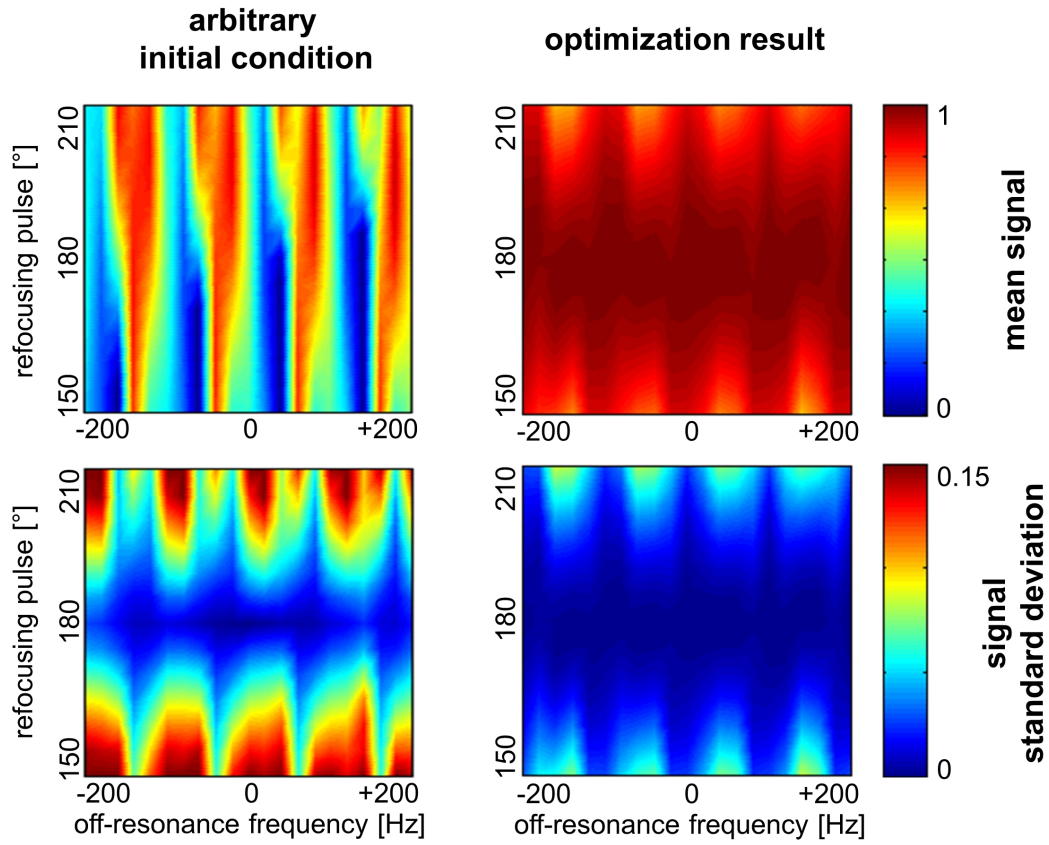

Figure 5.3: Exemplary result of the optimization of 7 preparation pulses for non-CPMG pulse sequence.

Instead of using 7 discrete preparation pulses, the algorithm allows also to implement and to optimize one shaped preparation pulse. Such a shaped pulse has more flexibility and leads to better optimization results, though it is difficult to implement for a slice-selective excitation. Figures 5.4 and 5.5 show the results of

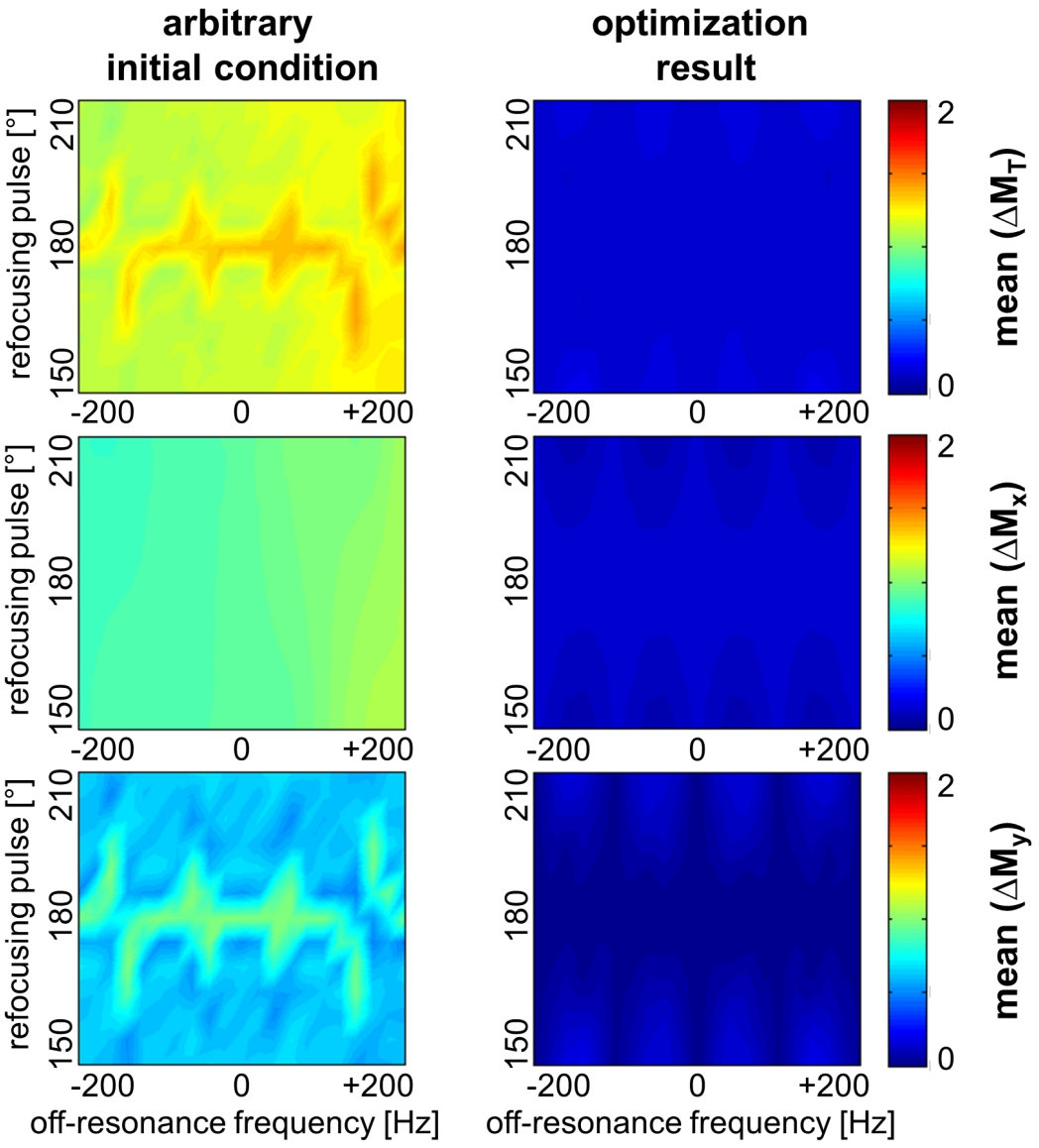

Figure 5.4: Exemplary result of the optimization of shaped preparation pulse (5 ms pulse width) for CPMG pulse sequence.

the optimization of the shaped preparation pulse with 5 ms pulse width for CPMG and non-CPMG pulse sequences with 24 180° refocusing pulses, respectively. Here,

another quality metrics for the visualization of the results was chosen: the mean variation of the total transverse M_T (top), M_x (middle) and M_y (bottom) components to the mean acquired signal $\bar{M}_T$, $\bar{M}_x$ and $\bar{M}_y$ (cf. Eq. (3.23)). This metrics represents more detailed the stability of the amplitude and phase of the MR signal.

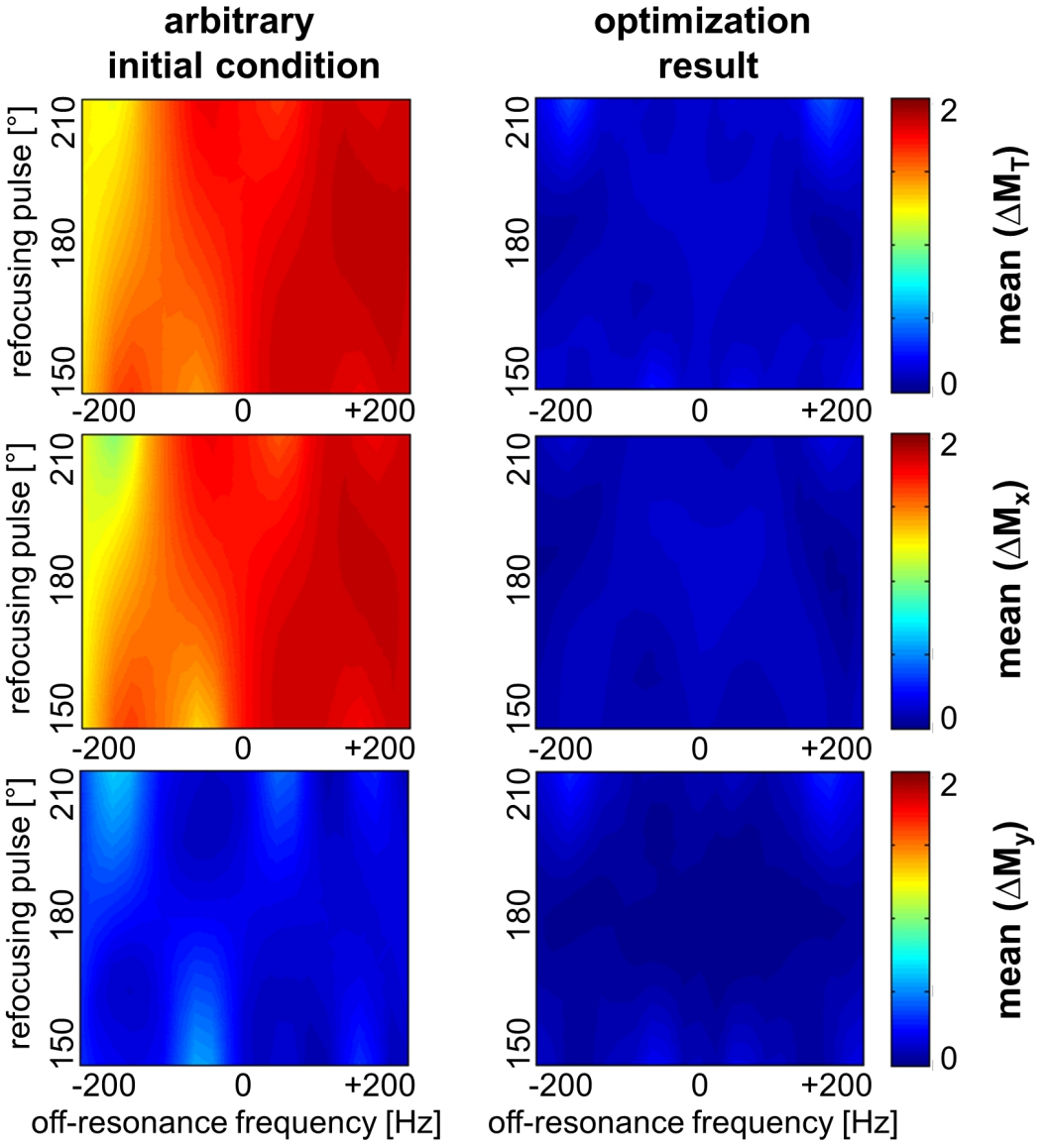

Figure 5.5: Exemplary result of the optimization of shaped preparation pulse (5 ms pulse width) for non-CPMG pulse sequence.

Figure 5.6 shows the preparation pulse profile, the pulse sequence scheme and the evolution of the total cost function for the non-CPMG pulse sequence example.

Each refocusing pulse was shifted in phase quadratically.

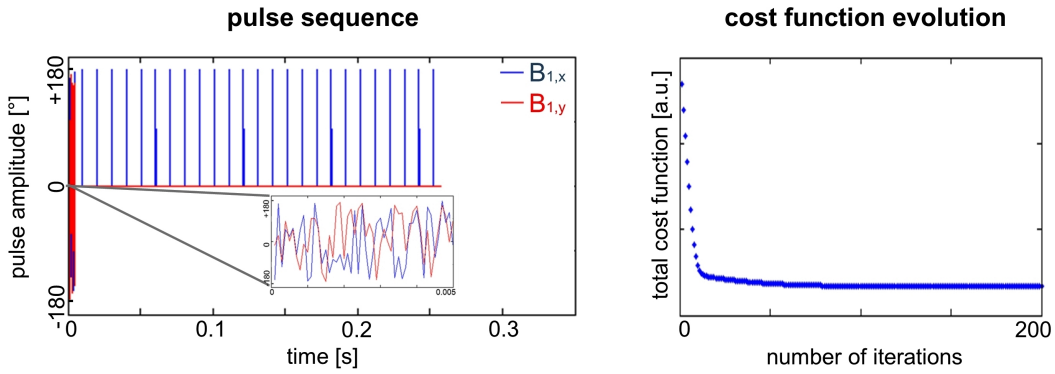

Figure 5.6: Pulse sequence diagram and the optimized preparation pulse profile (left) of the non-CPMG pulse sequence with shaped preparation pulse, together with the evolution of the total cost function (right).

In some cases, instead of maximization of the total signal, it is required to keep the magnetization at the certain constant level for further acquisition time steps. Such an application is especially useful for the non-recoverable hyperpolarized signal. For this purpose, the optimization algorithm was changed by setting the signal maximization term of the cost function to zero (by β_1=0 in Eq. (3.24)) and replacing the mean signal $\bar{M_T}$ in Eq. (3.23) by the desired transverse magnetization M_T^{desir}. Fig. 5.7 shows an example of such optimization for 7 preparation pulses of the non-CPMG pulse sequence with 24 180° refocusing pulses, where the desired transverse magnetization was chosen to be equivalent to the 60° excitation of the initial z magnetization.

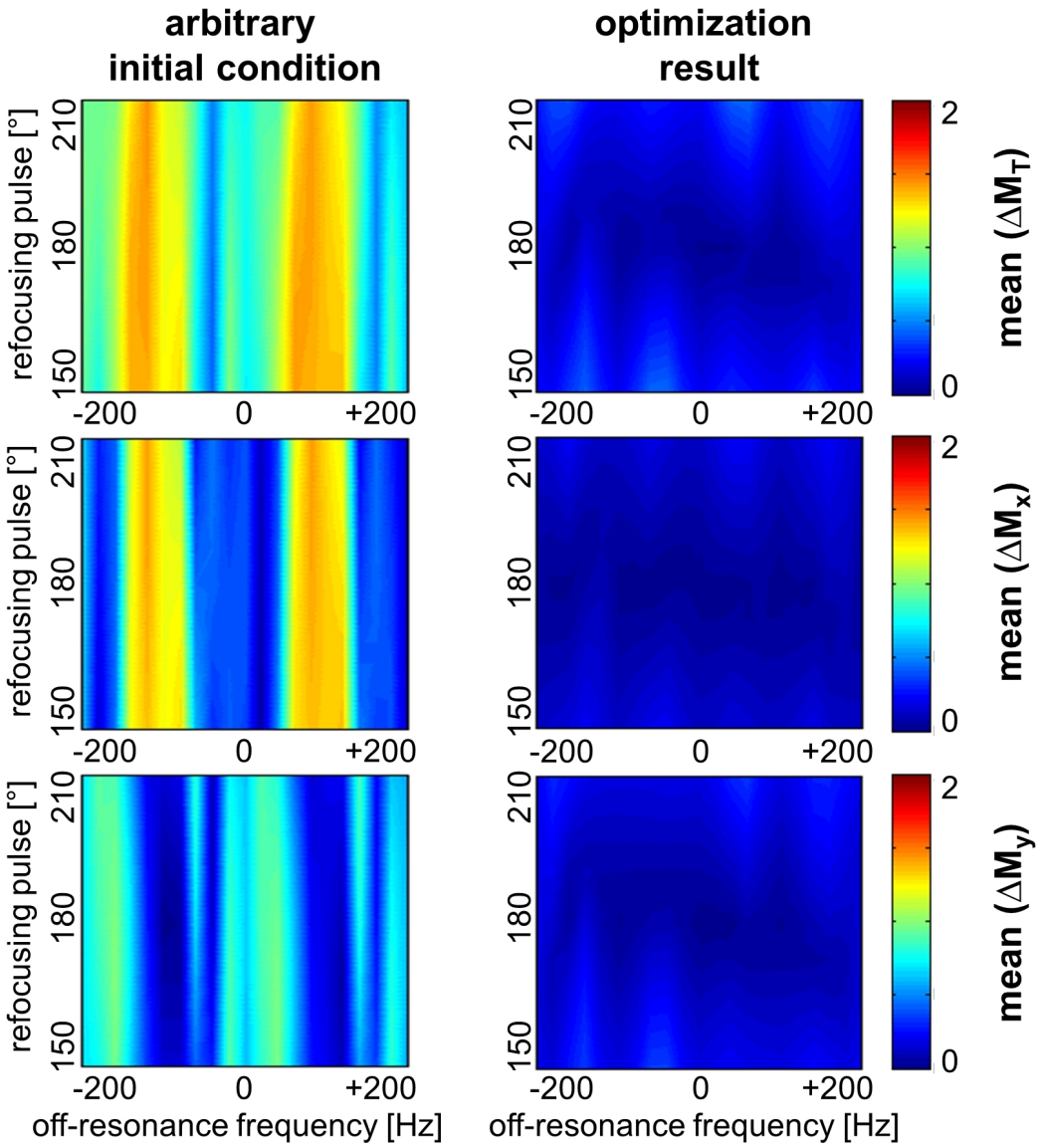

Figure 5.7: Exemplary result of the optimization of 7 preparation pulses for the non-CPMG pulse sequence keeping the total magnetization at 60° and 120° excitation planes.

5.2 Spectral fitting

Figure 5.8 illustrates spectral fitting results of FID spectra acquired 30 s post injection for in vitro (LDH enzyme mixture (a) and tumor cell suspension (b)) and in vivo tumor rat (c) experiments. First the CS frequencies and line shape parameters were estimated using matching pursuit spectral decomposition. Table 5.1 summarizes obtained CS frequencies, which are in good agreement with values reported in the literature [80].

Experiment	lactate	pyruvate hydrate	alanine	pyruvate	bicarbonate
LDH enzyme mixture	-392 ± 5	-267 ± 6	-	0	-
tumor cell suspension	-396 ± 5	-270 ± 3	-	0	-
in vivo surface coil	-393 ± 4	-263 ± 4	-181 ± 3	0	$+326 \pm 3$
in vivo IDEAL spiral CSI	-395 ± 9	-268 ± 8	-182 ± 7	0	$+320 \pm 8$

Table 5.1: Estimated CS frequencies of ^{13}C metabolites (in Hz, mean ± SD) relative to [1-^{13}C]pyruvate for different types of experiments. The spectra were acquired at B_0 = 3 T and fitted using the matching pursuit algorithm.

In a second step, the relative metabolite concentrations were estimated using linear least-squares time domain spectral fitting according to Eq. (3.41) and (3.44). The fitted spectra closely follow the measured FID spectra, indicating the validity of the underlying CS model. Using a phantom containing several compounds at accurately adjusted concentrations, the quantification error of metabolite amplitudes was estimated to be about 11 %, i.e., similar to that for other fitting methods such as AMARES and LCModel ([27],[28],[29]).

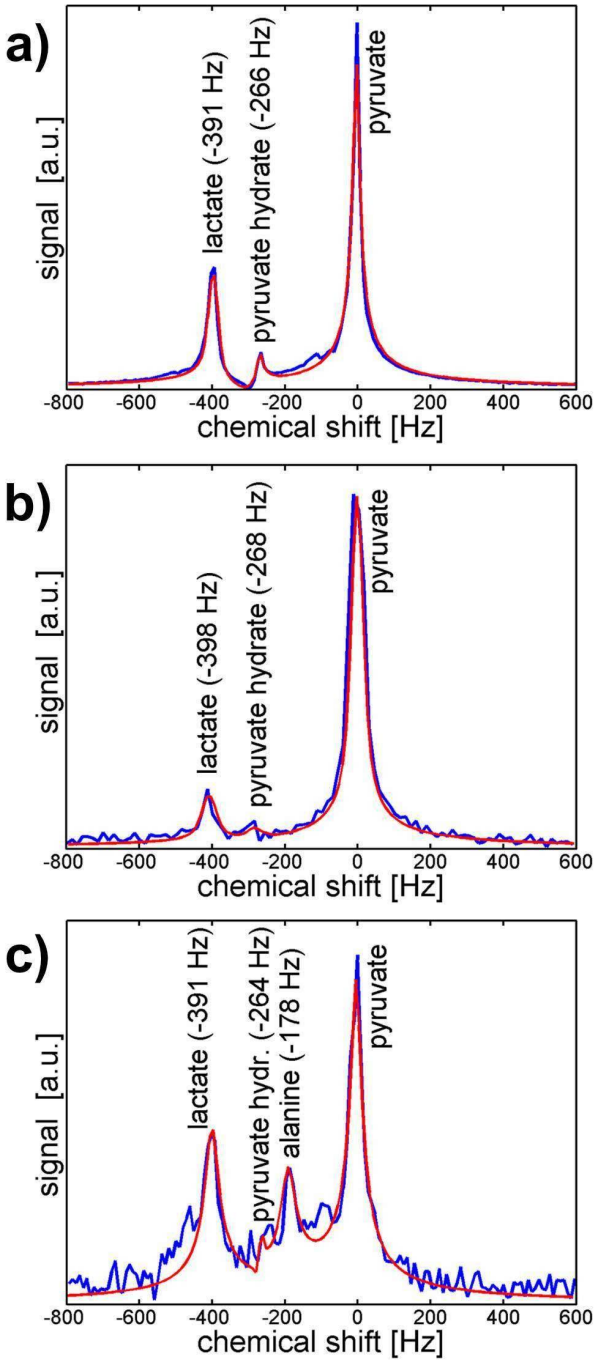

Figure 5.8: Exemplary spectra acquired 30 s after pyruvate injection (blue lines) and corresponding fitting results (red lines) for LDH enzyme mixture (a), tumor cell suspension (b) and in vivo rat tumor (c) experiments. The relative CS frequencies and line shape parameters were calculated using the matching pursuit algorithm.

5.3 Kinetic modelling

In both in vitro and in vivo experiments, a significant lactate signal was observed. Alanine and bicarbonate signals were noticed only in vivo and at comparatively lower amplitude. In the following, the kinetic fitting of the lactate signal will be considered.

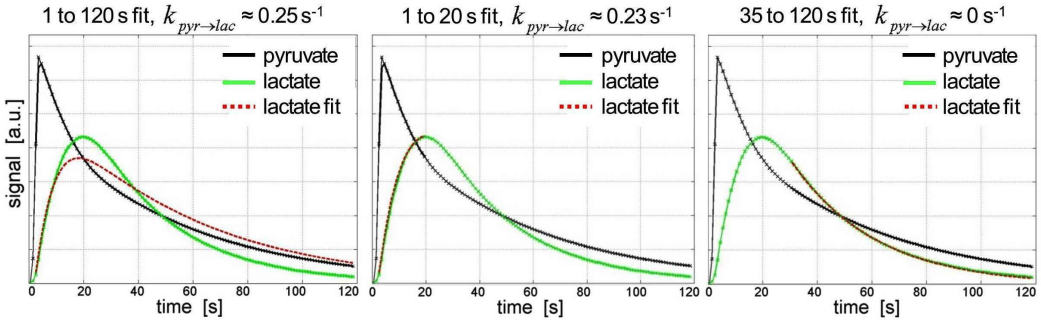

Figure 5.9: Example of LDH enzyme experiments with insufficient amount of coenzyme NADH. The proposed kinetic model was not able to fit over the entire time (left), but for shorter time intervals appropriate fitting results were found (middle and right).

The LDH enzyme experiments with insufficient amount of substrates were provided and showed that under this conditions the metabolic conversion rate changes significantly during the experiment (based on Michaelis-Menten kinetics). In this case the proposed kinetic model was still able to fit the time courses of metabolites but only over the smaller time intervals (assuming the smaller changes of substrate concentration) and not for the whole experiment time (Fig. 5.9).

Figure 5.10 displays results of the two-site exchange kinetic fitting in terms of the apparent build up rate $k_{pyr\rightarrow lac}$ and the effective relaxation rate $R_{eff,lac}$ for the same experimental conditions as those used in Fig. 5.8. Fitting was applied to the time intervals containing a significant pyruvate signal. The solid lines show metabolite signal curves, obtained from the spectral fitting of the measured FIDs. The dashed lines show the corresponding kinetic fitting results. A comparison of the typical metabolite signals in time and frequency domain is demonstrated in Fig. 5.11. It indicates a sparse, DC-centered representation of the metabolite signals in the frequency domain.

The experiments with the tumor cells showed that the apparent build-up rate

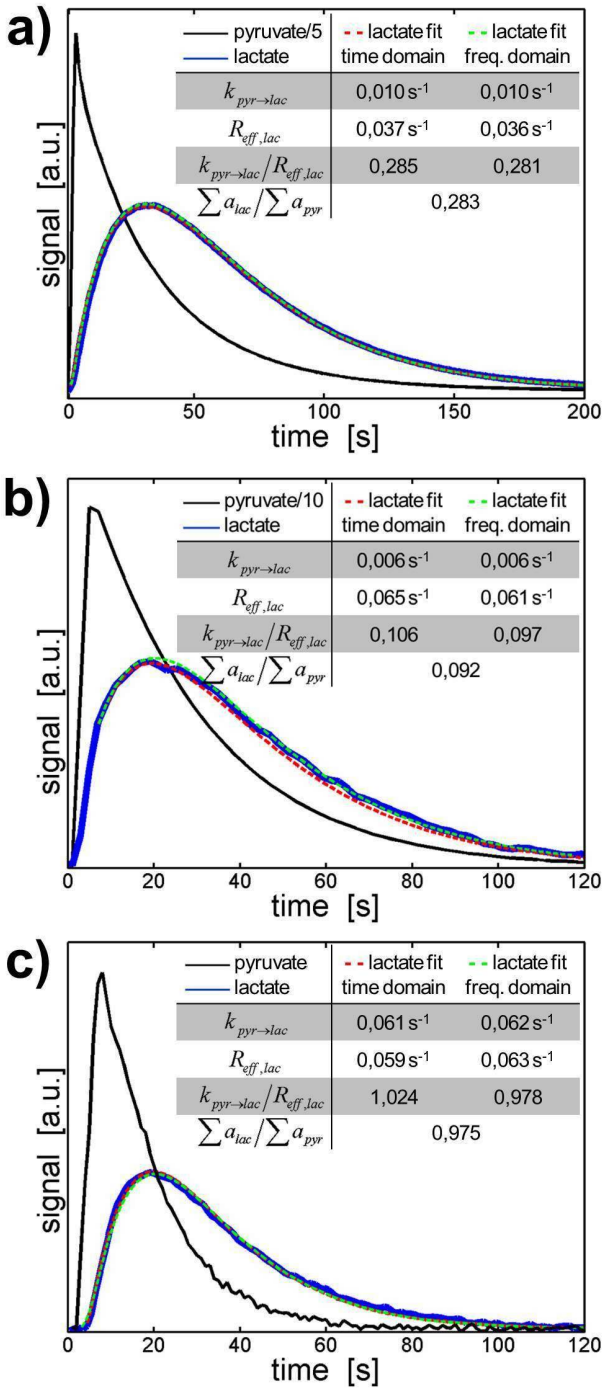

Figure 5.10: Exemplary time courses of metabolite signals and corresponding kinetic fitting results with apparent rate constants for LDH enzyme mixture (a), tumor cell suspension (b) and in vivo rat tumor (c) experiments. For the enzyme experiment, 2 ml of 20 mM hyperpolarized pyruvate were injected into the enzyme mixture containing NADH and 20 activity units of LDH.

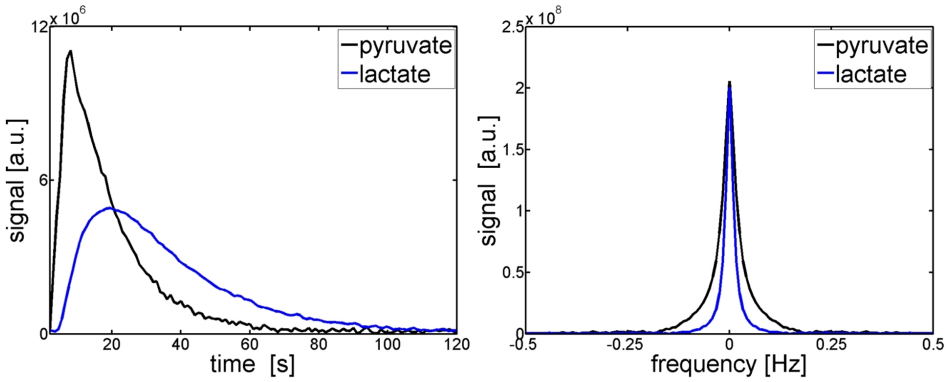

Figure 5.11: Typical in vivo metabolite signals (cf. Fig. 5.10 c) in time (left) and frequency (right) domain (absolute values). The similar signal intensity of pyruvate and lactate at $\Omega_n = 0$ in the frequency domain can be explained by the estimated ratio $k_{pyr\to lac}/R_{eff,lac} = \tilde{a}_{lac}(0)/\tilde{a}_{pyr}(0) \approx 1$.

constant $k_{pyr\to lac}$ depends not only on the LDH enzyme activity. For this purpose, the build up of [1-^{13}C]lactate in intact cells was compared with the one from the same amount of lysed cells (breaking down the membrane), holding all other experimental settings unchanged. The apparent build-up rate was approx. 10-fold higher in homogenates than in intact cells, suggesting that the cellular uptake of [1-^{13}C]pyruvate may be a rate-limiting factor. Preliminary experiments showed also sensitivity of tumor cells metabolism to extracellular pH and temperature. In further experiments with altering extracellular pH in range 6.6 - 7.8 no statistically significant correlation was found. However, for a better understanding of the cellular metabolism, the dependency of apparent rate constants on microenvironmental changes needs to be investigated in future studies. The results might be particularly useful for interpretation of eventual variations in in vivo tumors caused by differing physiological conditions.

Excellent fit quality was achieved in vitro and in vivo using both time and frequency domain fitting. It validated two-site exchange with only two fitting parameters, $k_{pyr\to lac}$ and $R_{eff,lac}$, as an effective kinetic model to accurately describe hyperpolarized ^{13}C pyruvate signal dynamics.

5.3.1 Time vs. frequency domain fitting

Further analysis of kinetic fitting in time and frequency domains showed significant differences between two methods. Table 5.2 compares the performance of time and frequency domain fitting as a function of SNR using Monte Carlo simula-

SNR		2.5	5	10	25	50	100
time domain	$k_{pyr\to lac}$	0.038± 0.070	0.062± 0.037	0.088± 0.014	0.099± 0.004	0.100± 0.002	0.100± 0.001
	$R_{eff,lac}$	0.019± 0.277	0.030± 0.103	0.056± 0.009	0.065± 0.003	0.066± 0.001	0.067± 0.001
freq. domain	$k_{pyr\to lac}$	0.088± 0.023	0.096± 0.014	0.100± 0.007	0.100± 0.003	0.100± 0.001	0.100± 0.001
	$R_{eff,lac}$	0.053± 0.020	0.062± 0.011	0.066± 0.006	0.067± 0.002	0.067± 0.001	0.067± 0.001

Table 5.2: Comparison of estimated apparent build-up and effective decay rate constants (in s^{-1}, mean ± SD) for different SNR of metabolite time signals using time and frequency domain methods. Metabolite time courses were generated by Monte Carlo simulations using representative in vivo values $k_{pyr\to lac}$=0.01 s^{-1} and $R_{eff,lac}$=0.067 s^{-1}. The SNR was defined at the maximum of pyruvate signal.

tions based on representative in-vivo tumor signal time courses and rate constants. At low SNR the frequency-domain fitting outperforms the time-domain method, whereas at higher SNR the two methods converge.

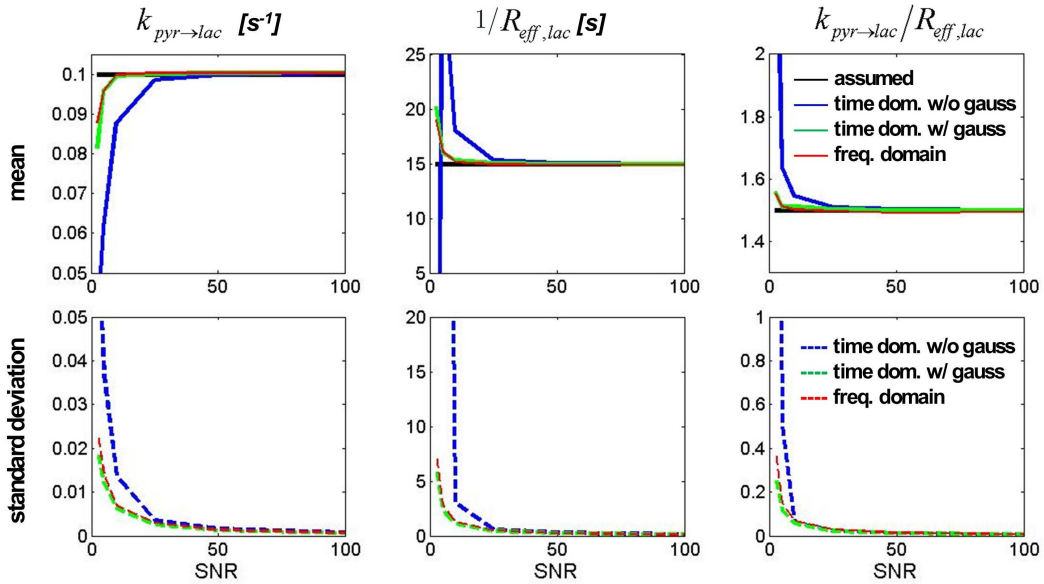

Figure 5.12: Comparison of fitting in time vs. frequency domain as a function of SNR (based on Monte Carlo simulations for assumed values). Mean (top) and standard deviation (bottom) of estimated $k_{pyr\to lac}$ (left), $1/R_{eff,lac}$ (middle) and ratio $k_{pyr\to lac}/R_{eff,lac}$ (right) are shown. The time domain fitting was performed with (green) and without (blue) Gaussian filter of 10 Hz.

Generally, higher SNR or sampling rate increased the accuracy of the fitting results for both methods. For the fitting in frequency domain, various frequency intervals around DC (cf. Fig. 5.11 rights) were tested, but no significant advantage of using wide frequency range was found. This result confirmed the sparsity of the signal information in frequency domain. Interestingly, applying the Gaussian filter on the data prior to fitting in time domain, provided similar results as using frequency domain fitting (Fig. 5.12).

5.4 Animal imaging

IDEAL spiral CS imaging was used to acquire dynamic, multislice metabolite maps at an effective time resolution of 4 s (Fig. 5.13). The data are displayed in form of image overlays of metabolite images with a high-resolution gradient echo image of identical scan geometry used as anatomical reference. The metabolite images (nominal matrix resolution of 32×32) were interpolated to the resolution of proton images (256×256). The images contain a wealth of information including substrate perfusion, uptake, and metabolic conversion and provided the input for spatially resolved, apparent build-up rate constant mapping. For this purpose, kinetic fitting according to Eq. (3.47) and (3.48) was applied on a pixel-by-pixel basis.

Figure 5.14 exemplary displays four different slices of the tumor bearing rat in the form of time-integrated metabolite images for lactate and pyruvate (top two rows), the ratio of time-integrated metabolite signals (middle row) and the apparent build-up rate constant maps of lactate estimated in time and frequency domain (bottom two rows). In both of the tumor containing slices (slices #3 and #4), the subcutaneous tumor clearly displays increased metabolic activity. In comparison to the time-integrated metabolite images, the apparent build-up rate constant maps and the ratio of time-integrated metabolite images show increased contrast for metabolically active tissues such as the tumor (Table 5.3). In contrast, well-supplied regions of low metabolic activity, such as the blood vessels, gastrointestinal tract (GIT) and the kidneys, appear suppressed.

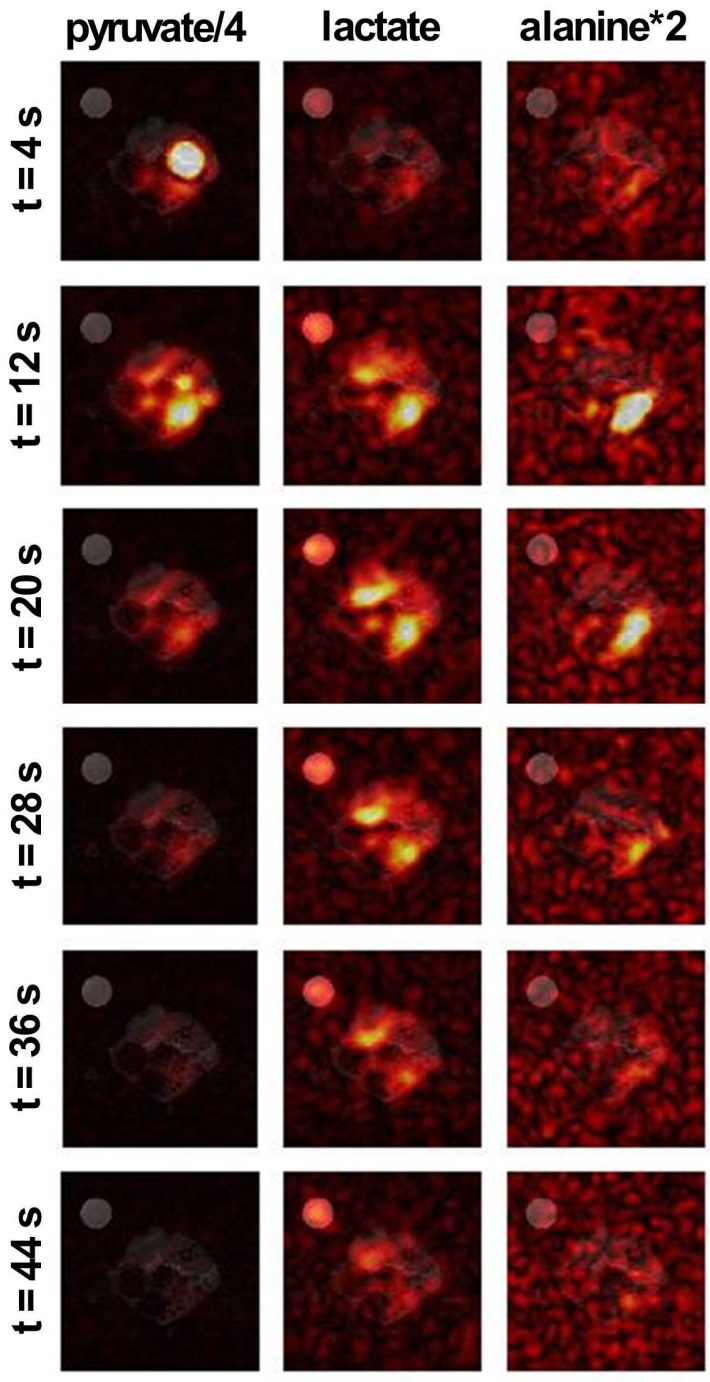

Figure 5.13: Example of dynamic IDEAL spiral CSI experiment in the tumor slice. Three metabolite images (pyruvate, lactate and alanine) are illustrated for the first six time points with temporal resolution of 8 s. The timing is relative to the start of data acquisition. The signals are shown in [a.u.], the relative scales of pyruvate and alanine are increased by four times or decreased by twice, respectively, compared to lactate.

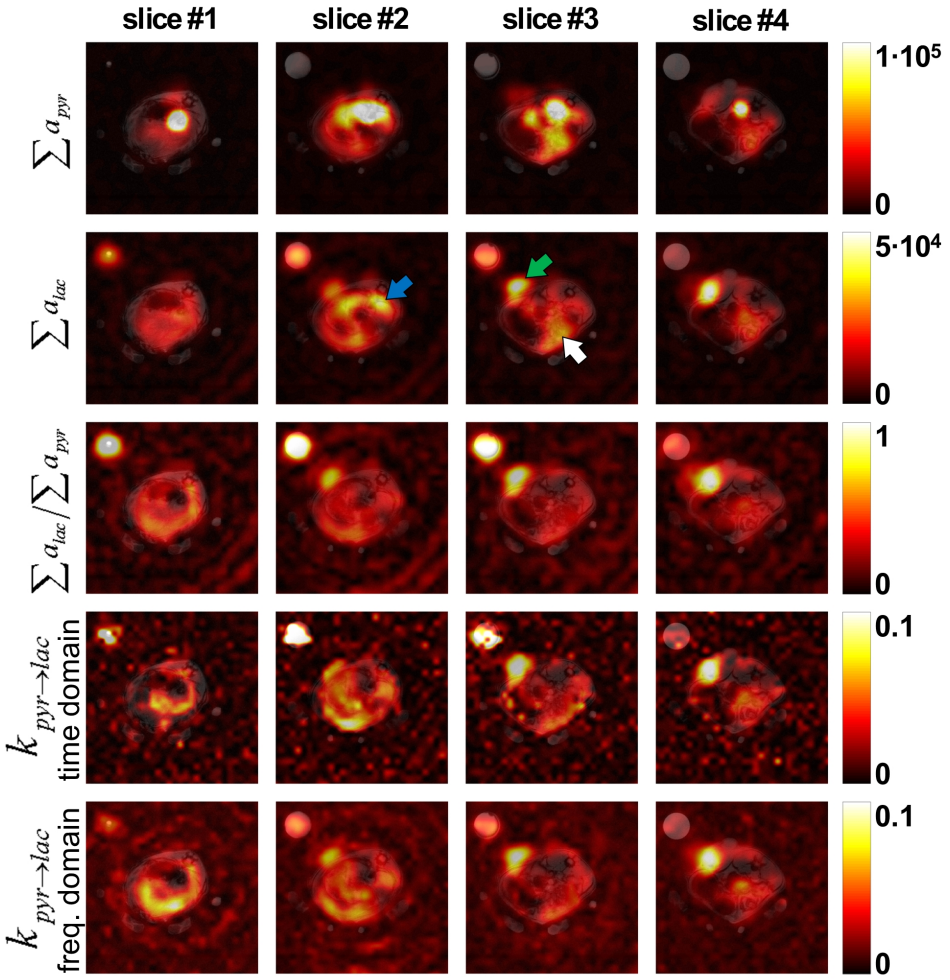

Figure 5.14: Time-integrated metabolite maps of pyruvate and lactate (top two rows, in a. u.), ratio of time-integrated metabolite signals (middle row) and apparent build-up rates of lactate estimated in time and frequency domain (bottom two rows, in s^{-1}) for 4 different slices. Based on reference proton images, slices #3 and #4 contain parts of the tumor. A syringe containing [1-^{13}C]lactate (at the top-left corner of each image) was used as a reference for both ^{13}C and proton images. The arrows are pointing to tumor (green), GIT (white) and kidneys (blue).

The consistency of the proposed kinetic model and results of the kinetic fitting in time and frequency domains is shown in Fig. 5.15. The analytical expression between apparent rates and metabolite time signals, which was found in Eq. (3.49), provided a good metrics for the comparison of the kinetic fitting results with the acquired raw data. The results of fitting in frequency domain were very similar to the raw data results even in the regions with low SNR, whereas the results of

time	SNR in tumor area	tumor to kidneys		tumor to GIT	
		CNR	CR	CNR	CR
mean lactate signal	25.4	2.61	0.05	8.72	0.21
$k_{pyr\to lac}$ time domain	7.0	4.28	0.44	4.36	0.46
$k_{pyr\to lac}$ freq. domain	7.8	5.20	0.50	4.17	0.48

Table 5.3: SNR in tumor area, CNR and contrast resolution (CR) of mean lactate signal and apparent rate constant. The contrast was compared between tumor, GIT and kidneys, which areas are shown in Fig. 5.14.

fitting in time domain showed some differences in the noise regions. In the regions of the sufficient SNR (almost the whole area containing the proton signal of the rat) all three methods showed nearly identical results.

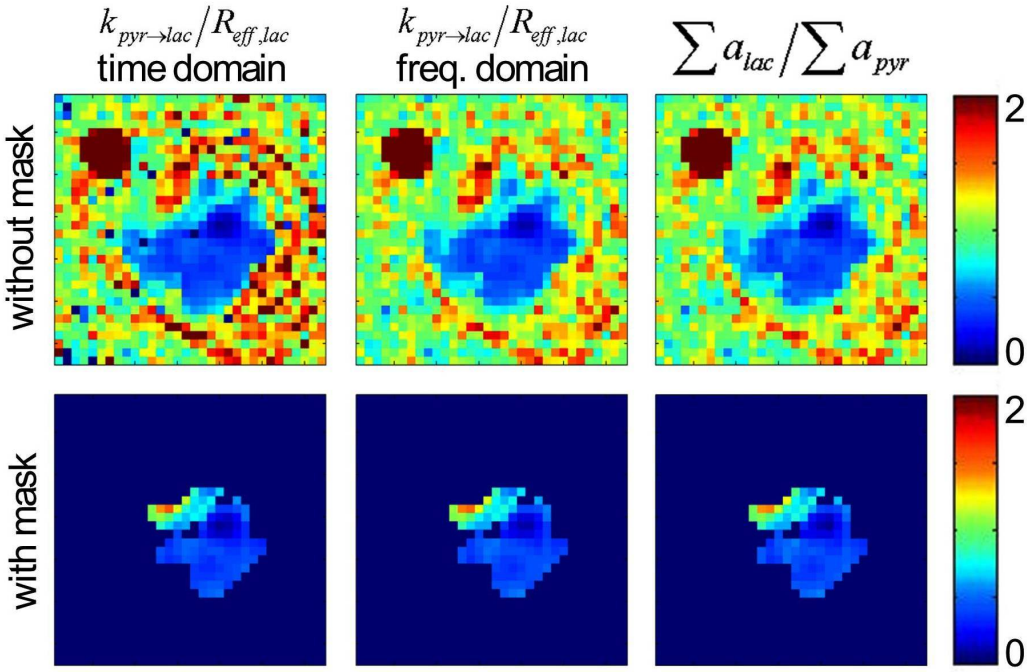

Figure 5.15: Comparison of the ratio of apparent build-up rate constant $k_{pyr\to lac}$ to apparent decay rate $R_{eff,lac}$, estimated in time and frequency domains, with a ratio of time-integrated metabolite signals $\sum a_{lac}/\sum a_{pyr}$. The bottom row shows the same data with a mask based on the SNR of the data.

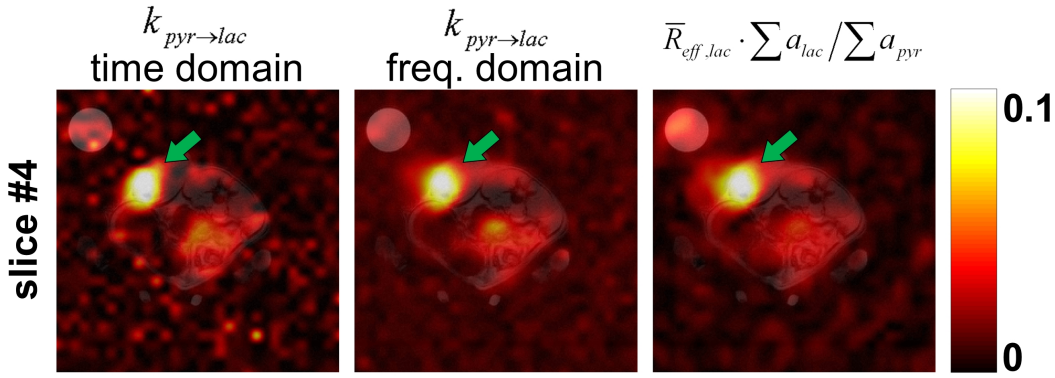

Figure 5.16: Comparison of apparent build-up rate constant maps with a ratio of time-integrated metabolite signals normalized by average decay rate $\tilde{R}_{eff,lac} = 0.1\ \mathrm{s}^{-1}$ (cf. Fig. 5.14 slice #4). High apparent build-up rate constant in the tumor (green arrow) indicates its high metabolic activity.

Figure 5.16 compares apparent build-up rate constant maps for lactate obtained from time (left) and frequency (middle) domain fitting to an approximate one derived from the ratio of the time-integrated signals of lactate to those of pyruvate, normalized by the average decay rate $\tilde{R}_{eff,lac} = 0.1\ \mathrm{s}^{-1}$ (right). Equation (3.49) shows the linear relationship between the apparent build-up rate constant and the ratio of time-integrated metabolite signals with the apparent decay rate $R_{eff,m}$ as a proportional coefficient. Owing to the fact that the major contribution to $R_{eff,m}$ is caused by the repetitive excitation, and assuming relatively small differences between T_1 relaxation times in organs and a negligible backward conversion, the apparent decay rate was substituted by an averaged decay rate $\tilde{R}_{eff,lac}$. The later was estimated from the IDEAL spiral CS imaging protocol ($\alpha = 10°$ with eight excitations per 4 s time step) and assuming an average lactate T_1 relaxation time of 15 s according to Eq. (3.47). A total of four tumor rats were measured. Images of the tumor slices of the remaining three animals and the corresponding kinetic fitting results are shown in Fig. 5.17. The quantitative values of the apparent build-up rate of lactate $k_{pyr\rightarrow lac}$ in tumor were consistent with the values found in Fig. 5.10 (c).

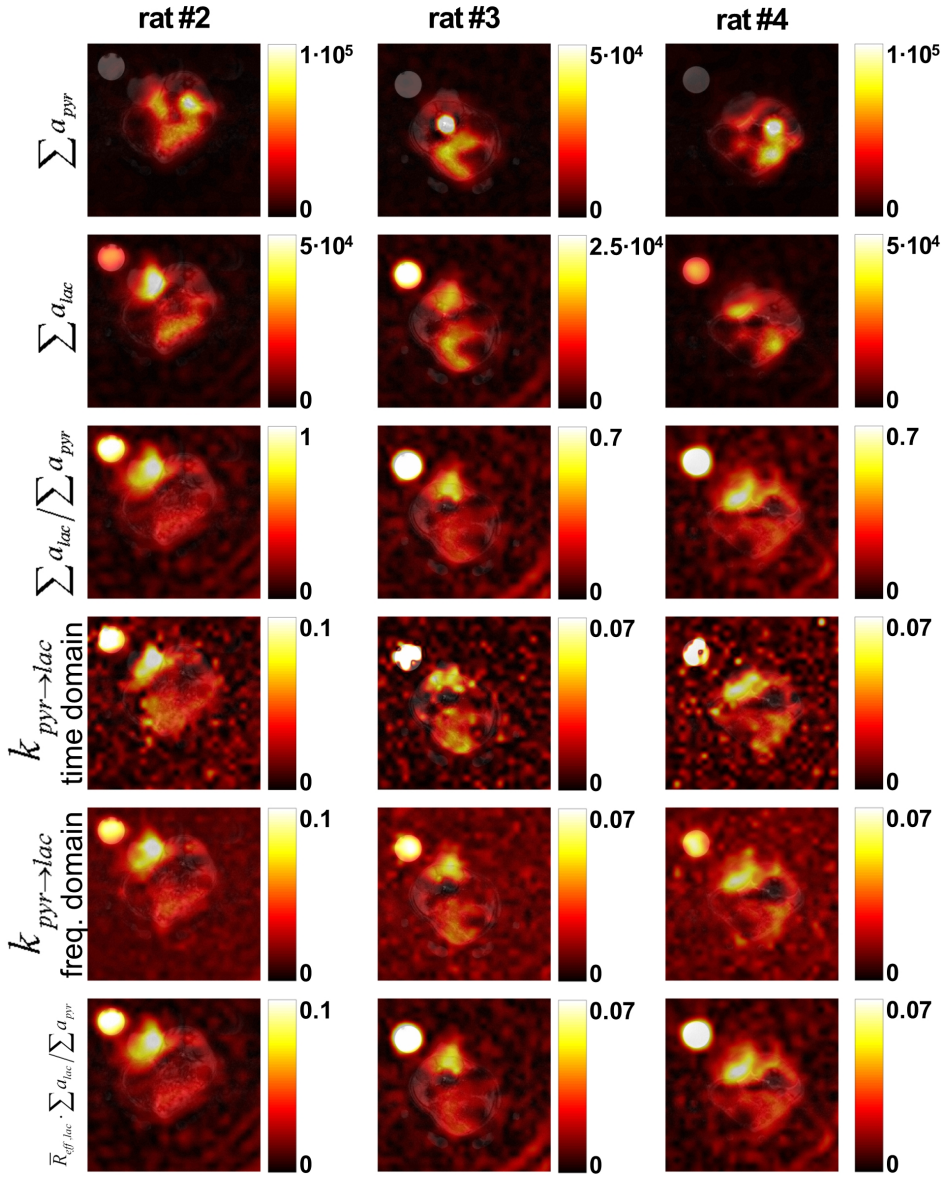

Figure 5.17: Metabolic images of the tumor slices in three tumor rats and corresponding apparent build-up rate constant maps of lactate together with ratio of time-integrated metabolite signals normalized by average decay rate $\tilde{R}_{eff,lac} = 0.1$ s^{-1}.

6 Discussion and Conclusions

The first aim of this work was the development of new acquisition strategies for hyperpolarized metabolic MRI. The non-recoverable magnetization of the hyperpolarized nuclei required to design carefully appropriate pulse sequences without unnecessary signal depletion based on experimental inhomogeneities. For this purpose, the known imaging pulse sequences were modified and optimized using optimal control theory. The main focus was laid on the optimization of the preparation pulses fur further data acquisition with fast imaging pulse sequences. The obtained results indicate significant theoretical improvements using the developed optimization algorithm for different pulse sequences. In further studies, the feasibility of the method needs to be confirmed by experimental results.

The second aim of this work was to develop automatic and robust methods for the quantification and interpretation of dynamic hyperpolarized ^{13}C signals, with an emphasis on spatially-resolved apparent build-up rate constant mapping. For this purpose, dynamic FID measurements were first spectrally fitted into individual metabolite time signals, which were then kinetically fitted to obtain the apparent rate constants, $k_{pyr\rightarrow m}$ and $R_{eff,m}$. The signal formation was described based on physically motivated, linear forward models.

For spectral fitting, advantage is taken of the observation that hyperpolarized ^{13}C spectra are formed by well-separated singlet peaks without a macromolecular baseline. Accordingly, measured time-domain signals are conveniently described as a summation over individual metabolite basis spectra (cf. Eq. (3.41)). The metabolite's CS frequencies and line shape parameters, required for the construction of the FID matrix, are extracted from the same FID measurements using a matching pursuit algorithm.

For kinetic fitting, a two-site exchange model was adapted with two variable fitting parameters in the form of i) an apparent build-up rate $k_{pyr\rightarrow m}$ and ii) an effective decay rate $R_{eff,m}$. Both rate constants are of quantitative nature with units of inverse seconds. It is important to note that $k_{pyr\rightarrow m}$ accounts for not only enzymatically driven forward conversion but also transport effects ([31],[34]). In order to individually resolve these two effects, the metabolite signals would need to be compartmentalized into intracellular and extracellular spaces, but currently clear distinction is not possible. The second parameter summarizes the signal decay mechanisms due to repetitive excitation, T_1 relaxation, and backward conversion into an effective decay rate $R_{eff,m}$. Addressing the kinetic equation in differential form eliminates the need for an explicit arterial input function, which is generally difficult to measure directly [81] and is, hence, often modeled based on simplified assumptions [25]. Instead, the arterial input function is implicitly contained in the measured pyruvate signals. A time-discretized formulation of the kinetic model allows apparent rate constants fitting in either the time or frequency domain. The later description is applicable only if the entire hyperpolarized signal time course is available but offers essential advantages. Firstly, it provides a natural and effective way of compressing the dynamic of metabolite signals into a few dominant Fourier coefficients around DC in the frequency space. Furthermore, in the frequency domain, the noise enhancing time differentiation is avoided, which is crucial in case of low SNR. Mathematically, the spectral and the kinetic signal model (both time- and frequency domain representations) describe over-determined, linear fitting problems, which in the matrix notation can be robustly solved using well-known algebraic methods.

The excellent spectral and kinetic fit quality demonstrated both for in vitro and in vivo experiments (cf. Fig. 5.8 and 5.10) validates the underlying signal models including the assumption of time constant apparent rate constants and also demonstrates the robustness of the method. For in vitro experiments, relatively simple modification of the experimental setup was performed in order to achieve high SNR and reduced spectral linewidth, which are required for a precise estimation of the apparent rates, and therefore to allow accurate measurement of changes in pyruvate metabolic flux. In vivo, the temporal invariability of the apparent rate constants can be explained by the underlying Michaelis-Menten kinetics of enzyme reaction considering fast bolus arrival, relatively high concentration of pyruvate

and subsequent minor changes of pyruvate and lactate concentrations in the blood during the experiment [82]. For the performed experiments, the apparent build-up rate in the tumor was found to be comparable with the effective decay rate, an important prerequisite for SNR efficient detection of downstream metabolites. Signal decay due to repetitive excitation is typically significant and can, to a certain extent, be minimized via experimental optimization. For instance, spectral-spatial multi-band excitation schemes can be used with smaller flip angles for pyruvate and higher ones for its metabolic products ([10],[38],[78]). This increases the detection efficiency for the downstream metabolites and, at the same time, retains the hyperpolarized substrate pool for longer detection times.

Dynamic CS imaging additionally resolves the hyperpolarized signals spatially, resulting in up to five-dimensional detailed information of ^{13}C metabolism. In this work, IDEAL spiral CSI [37] was used for dynamic CS image encoding at an effective time resolution of 4 s. However, in principle, other fast CS imaging methods like fast spiral CSI [83] and EPSI [8] can also be used. Displaying and analyzing such multi-dimensional data in a comprehensive manner is challenging. Here, spatially resolved kinetic fitting was used to compress the temporal dynamics into two apparent rate constants. In particular, $k_{pyr\rightarrow m}$ comprehensively visualizes the metabolic activity of underlying tissues and organs in a quantitative and spatially resolved manner. Because pyruvate is typically injected at partially saturation concentration ([29],[84]), the obtained rate constants are dependent on the amount and speed of the injected substrate as well as its distribution within the body. Conversely, $R_{eff,m}$ is generally more difficult to interpret because of its cumulative nature, which includes three distinct decay mechanisms. In comparison to a single time point or time-averaged metabolite images, the apparent build-up rate emphasizes metabolically active tissue (i.e. tumor or heart) and suppresses regions of high perfusion but low conversion (i.e. kidneys or gastrointestinal tract), which results in improved contrast resolution. Figure 5.14 and Table 5.3 illustrate the improved contrast provided by the apparent build-up rate, which clearly identifies the tumor location as the region of enhanced metabolism with $k_{pyr\rightarrow lac} \approx 0.1$ s^{-1}. Very similar contrast behavior was also obtained from the DC ratio of the metabolite maps normalized by the averaged decay rate as shown in Fig. 5.16. This method is more advantageous for data with low SNR, but may cause less precise quantitative results, due to the underlying assumption of an average, spatially-constant apparent

decay rate.

The developed quantification algorithm is not only limited to hyperpolarized [1-^{13}C]pyruvate, but can be also applied on other metabolically active hyperpolarized compounds, e.g. [5-^{13}C]glutamine, or improved by the co-polarization techniques. The utility of apparent build-up rate constant mapping for the non-invasive localization and characterization of tumors and their response to therapy needs to be further investigated in dedicated studies. In particular, it needs to be investigated whether its quantitative nature can be used in a similar manner as, for instance, the standardized uptake value (SUV) commonly used in positron-emission tomography (PET) [85].

Bibliography

[1] F. Bloch, W.W. Hansen, and M. Packard. The nuclear induction experiment. *Phys Rev*, 70:474–485, 1946.

[2] E.M. Purcell, H.C. Torrey, and R.V. Pound. Resonance absorption by nuclear magnetic moments in a solid. *Phys Rev*, 69:37–38, 1946.

[3] P. C. Lauterbur. Image formation by induced local interactions: Examples employing nuclear magnetic resonance. *Nature*, 242(5394):190–191, 1973.

[4] P. Mansfield and A. A. Maudsley. Medical imaging by NMR. *British Journal of Radiology*, 50(591):188–194, 1977.

[5] A.W. Overhauser. Polarization of nuclei in metals. *Phys Rev*, 92:411–415, 1953.

[6] L. Zhao and M.S. Albert. Biomedical imaging using hyperpolarized noble gas MRI: pulse sequence considerations. *Nucl Instrum Methods Phys Res A*, 420:454–460, 1998.

[7] E. Durand, G. Guillot, L. Darrasse, G. Tastevin, P.J. Nacher, A. Vignaud, D. Vattolo, and J. Bittoun. CPMG measurements and ultrafast imaging in human lungs with hyperpolarized ^{3}He at low field (0.1 T). *Magnetic Resonance in Medicine*, 47:75–81, 2002.

[8] C. H. Cunningham, A. P. Chen, M. J. Albers, J. Kurhanewicz, R. E. Hurd, Y. F. Yen, J. M. Pauly, S. J. Nelson, and D. B. Vigneron. Double spin-echo sequence for rapid spectroscopic imaging of hyperpolarized ^{13}C. *Journal of Magnetic Resonance*, 187(2):357–362, 2007.

[9] A. B. Kerr, P. E. Larson, M. Lustig, C. H. Cunningham, A. P. Chen, D. B. Vigneron, , and J. M. Pauly. Multiband spectral-spatial design for high-field and hyperpolarized ^{13}C applications. In *Proceedings of the 16th Annual Meeting of ISMRM*, 2008.

[10] P. Larson, A. Kerr, A. Chen, M. Lustig, M. Zierhut, S. Hu, C. Cunningham, J. Pauly, J. Kurhanewicz, and D. Vigneron. Multiband excitation pulses for hyperpolarized ^{13}C dynamic chemical-shift imaging. *Journal of Magnetic Res-*

onance, 194(1):121–127, 2008.

[11] C. H. Cunningham, A. P. Chen, M. Lustig, B. A. Hargreaves, J. Lupo, D. Xu, J. Kurhanewicz, R. E. Hurd, J. M. Pauly, S. J. Nelson, and D. B. Vigneron. Pulse sequence for dynamic volumetric imaging of hyperpolarized metabolic products. *Journal of Magnetic Resonance*, 193:139–146, 2008.

[12] J. H. Ardenkjaer-Larsen, B. Fridlund, A. Gram, G. Hansson, L. Hansson, M. H. Lerche, R. Servin, M. Thaning, and K. Golman. Increase in signal-to-noise ratio of > 10,000 times in liquid-state NMR. *Proceedings of the National Academy of Sciences*, 100(18):10158–10163, 2003.

[13] K. Golman. Molecular imaging with endogenous substances. *Proceedings of the National Academy of Sciences*, 100(18):10435–10439, 2003.

[14] K. Golman. Real-time metabolic imaging. *Proceedings of the National Academy of Sciences*, 103(30):11270–11275, 2006.

[15] J. H. Ardenkjaer-Larsen, S. Macholl, and H. Johannesson. Dynamic nuclear polarization with trityls at 1.2 K. *Applied Magnetic Resonance*, 34(3-4):509–522, 2008.

[16] F.A. Gallagher, M.I. Kettunen, and K.M. Brindle. Biomedical applications of hyperpolarized ^{13}C magnetic resonance imaging. *Progress in Nuclear Magnetic Resonance Spectroscopy*, 55(4):285–295, 2009.

[17] O. Feron. Pyruvate into lactate and back: From the Warburg effect to symbiotic energy fuel exchange in cancer cells. *Radiotherapy and Oncology*, 92(3):329–333, 2009.

[18] R. J. DeBerardinis, J. J. Lum, G. Hatzivassiliou, and C. B. Thompson. The biology of cancer: Metabolic reprogramming fuels cell growth and proliferation. *Cell Metabolism*, 7(1):11–20, 2008.

[19] K. Golman, R. i. Zandt, M. Lerche, R. Pehrson, and J. H. Ardenkjaer-Larsen. Metabolic imaging by hyperpolarized ^{13}C magnetic resonance imaging for in vivo tumor diagnosis. *Cancer Research*, 66(22):10855–10860, 2006.

[20] S. E. Day, M. I. Kettunen, F. A. Gallagher, D. Hu, M. Lerche, J. Wolber, K. Golman, J. H. Ardenkjaer-Larsen, and K. M. Brindle. Detecting tumor response to treatment using hyperpolarized ^{13}C magnetic resonance imaging and spectroscopy. *Nature Medicine*, 13(11):1382–1387, 2007.

[21] S.J. Kohler, Y. Yen, J. Wolber, A.P. Chen, M.J. Albers, R. Bok, V. Zhang, J. Tropp, S. Nelson, D.B. Vigneron, J. Kurhanewicz, and R.E. Hurd. In vivo 13-carbon metabolic imaging at 3 T with hyperpolarized 1-^{13}C-pyruvate.

Magnetic Resonance in Medicine, 58(1):65–69, 2007.

[22] M. J. Albers, R. Bok, A. P. Chen, C. H. Cunningham, M. L. Zierhut, V. Y. Zhang, S. J. Kohler, J. Tropp, R. E. Hurd, Y.-F. Yen, S. J. Nelson, D. B. Vigneron, and J. Kurhanewicz. Hyperpolarized ^{13}C lactate, pyruvate, and alanine: Noninvasive biomarkers for prostate cancer detection and grading. *Cancer Research*, 68(20):8607–8615, 2008.

[23] C. S. Ward, H. S. Venkatesh, M. M. Chaumeil, A. H. Brandes, M. VanCriekinge, H. Dafni, S. Sukumar, S. J. Nelson, D. B. Vigneron, J. Kurhanewicz, C. D. James, D. A. Haas-Kogan, and S. M. Ronen. Noninvasive detection of target modulation following phosphatidylinositol 3-kinase inhibition using hyperpolarized ^{13}C magnetic resonance spectroscopy. *Cancer Research*, 70(4):1296–1305, 2010.

[24] D. Mayer, Y.-F. Yen, J. Tropp, A. Pfefferbaum, R. E. Hurd, and D. M. Spielman. Application of subsecond spiral chemical shift imaging to real-time multislice metabolic imaging of the rat in vivo after injection of hyperpolarized ^{13}C 1-pyruvate. *Magnetic Resonance in Medicine*, 62(3):557–564, 2009.

[25] M. L. Zierhut, Y.-F. Yen, A. P. Chen, R. Bok, M. J. Albers, V. Zhang, J. Tropp, I. Park, D. B. Vigneron, and J. Kurhanewicz. Kinetic modeling of hyperpolarized 1-^{13}C-pyruvate metabolism in normal rats and TRAMP mice. *Journal of Magnetic Resonance*, 202(1):85–92, 2010.

[26] I. Park, P. E. Z. Larson, M. L. Zierhut, S. Hu, R. Bok, T. Ozawa, J. Kurhanewicz, D. B. Vigneron, S. R. Vandenberg, C. D. James, and S. J. Nelson. Hyperpolarized ^{13}C magnetic resonance metabolic imaging: application to brain tumors. *Neuro-Oncology*, 12(2):133–144, 2010.

[27] L. Vanhamme, A. van den Boogaart, and S. Van Huffel. Improved method for accurate and efficient quantification of MRS data with use of prior knowledge. *Journal of Magnetic Resonance*, 129(1):35–43, 1997.

[28] S. W. Provencher. Automatic quantitation of localized in vivo ^{1}H spectra with LCModel. *NMR in Biomedicine*, 14(4):260–264, 2001.

[29] M. A. Janich, M. I. Menzel, F. Wiesinger, E. Weidl, O. Khegai, J. H. Ardenkjaer-Larsen, S. J. Glaser, A. Haase, R. F. Schulte, and M. Schwaiger. Effects of pyruvate dose on in vivo metabolism and quantification of hyperpolarized ^{13}C spectra. *NMR in Biomedicine*, 25(1):142–151, 2012.

[30] F. Wiesinger, I. Miederer, M. I. Menzel, E. Weidl, M. A. Janich, J. H. Ardenkjaer-Larsen, M. Schwaiger, and R. F. Schulte. Metabolic rate constant

mapping of hyperpolarized 13C pyruvate. In *Proceedings of the 18th Annual Meeting of ISMRM*, volume 18, page 3282, 2010.

[31] K. M. Brindle, S. E. Bohndiek, F. A. Gallagher, and M. I. Kettunen. Tumor imaging using hyperpolarized ^{13}C magnetic resonance spectroscopy. *Magnetic Resonance in Medicine*, 66(2):505–519, 2011.

[32] T. Harris, G. Eliyahu, L. Frydman, and H. Degani. Kinetics of hyperpolarized 1-^{13}C-pyruvate transport and metabolism in living human breast cancer cells. *Proceedings of the National Academy of Sciences*, 106(43):18131–18136, 2009.

[33] K. R. Keshari, J. Kurhanewicz, R. E. Jeffries, D. M. Wilson, B. J. Dewar, M. Van Criekinge, M. Zierhut, D. B. Vigneron, and J. M. Macdonald. Hyperpolarized ^{13}C spectroscopy and an NMR-compatible bioreactor system for the investigation of real-time cellular metabolism. *Magnetic Resonance in Medicine*, 63(2):322–329, 2010.

[34] T. H. Witney, M. I. Kettunen, and K. M. Brindle. Kinetic modeling of hyperpolarized ^{13}C label exchange between pyruvate and lactate in tumor cells. *Journal of Biological Chemistry*, 2011.

[35] M. I. Kettunen, D. Hu, T. H. Witney, R. McLaughlin, F. A. Gallagher, S. E. Bohndiek, S. E. Day, and K. M. Brindle. Magnetization transfer measurements of exchange between hyperpolarized [1-^{13}C]pyruvate and [1-^{13}C]lactate in a murine lymphoma. *Magnetic Resonance in Medicine*, 63(4):872–880, 2010.

[36] R. E. Hurd, Y.-F. Yen, D. Mayer, A. Chen, D. Wilson, S. Kohler, R. Bok, D. Vigneron, J. Kurhanewicz, J. Tropp, D. Spielman, and A. Pfefferbaum. Metabolic imaging in the anesthetized rat brain using hyperpolarized [1-^{13}C] pyruvate and [1-^{13}C] ethyl pyruvate. *Magnetic Resonance in Medicine*, 63(5):1137–1143, 2010.

[37] F. Wiesinger, E. Weidl, M. I. Menzel, M. A. Janich, O. Khegai, S. J. Glaser, A. Haase, M. Schwaiger, and R. F. Schulte. IDEAL spiral CSI for dynamic metabolic MR imaging of hyperpolarized [1-^{13}C]pyruvate. *Magnetic Resonance in Medicine*, 68(1):8–16, 2012.

[38] T. Xu, D. Mayer, M. Gu, Y.-F. Yen, S. Josan, J. Tropp, A. Pfefferbaum, R. Hurd, and D. Spielman. Quantification of in vivo metabolic kinetics of hyperpolarized pyruvate in rat kidneys using dynamic ^{13}C MRSI. *NMR in Biomedicine*, 24(8):997–1005, 2011.

[39] S. Hu, A. P. Chen, M. L. Zierhut, R. Bok, Y.-F. Yen, M. A. Schroeder, R. E. Hurd, S. J. Nelson, J. Kurhanewicz, and D. B. Vigneron. In vivo carbon-13

dynamic MRS and MRSI of normal and fasted rat liver with hyperpolarized ^{13}C-pyruvate. *Molecular Imaging and Biology*, 11(6):399–407, 2009.

[40] J. Kurhanewicz, D. B. Vigneron, K. Brindle, E. Y. Chekmenev, A. Comment, C. H. Cunningham, R. J. Deberardinis, G. G. Green, M. O. Leach, S. S. Rajan, R. R. Rizi, B. D. Ross, W. S. Warren, and C. R. Malloy. Analysis of cancer metabolism by imaging hyperpolarized nuclei: prospects for translation to clinical research. *Neoplasia*, 13(2):81–97, 2011.

[41] M. Kim and S. Lee. Spin echoes after arbitrary N pulses. *Journal of Magnetic Resonance*, 125:114–119, 1997.

[42] William Allyn Grissom. *RF pulse design for parallel excitation in MRI*. PhD thesis, The University of Michigan, 2008.

[43] J. T. Bushberg, J. A. Seibert, E. M. Leidholdt, and J. M. Boone. *The Essential Physics of Medical Imaging*. Lippincott Williams and Wilkins, 3 edition, 2011.

[44] H. Y. Carr and E. M. Purcell. Effects of diffusion on free precession in nuclear magnetic resonance experiments. *Physical Review*, 94(3):630–638, 1954.

[45] K. Scheffler. A pictorial description of steady-states in rapid magnetic resonance imaging. *Concepts Magn Reson*, 11:291–304, 1999.

[46] K. Scheffler and S. Lehnhardt. Principles and applications of balanced SSFP techniques. *Eur Radiol*, 13:2409–2418, 2003.

[47] F. Staehle, J. Leupold, J. Hennig, and M. Markl. Off-resonance-dependent slice profile effects in balanced steady-state free precession imaging. *Magnetic Resonance in Medicine*, 59:1197–1202, 2008.

[48] P. LeRoux. Non CPMG phase modulation, the easy way. In *Proceedings of the 14th Annual Meeting of ISMRM*, 2006.

[49] P. Le Roux. Simplified model and stabilization of SSFP sequences. *Journal of Magnetic Resonance*, 163:23–37, 2003.

[50] P. Le Roux. Non-CPMG fast spin echo with full signal. *Journal of Magnetic Resonance*, 155:278–292, 2002.

[51] W. A. Edelstein, G. H. Glover, C. J. Hardy, and R. W. Redington. The intrinsic signal-to-noise ratio in NMR imaging. *Magnetic Resonance in Medicine*, 3(4):604–618, 1986.

[52] A. Abragam and M. Goldman. Principles of dynamic nuclear polarisation. *Reports on Progress in Physics*, 41(3):395, 1978.

[53] T. Maly, G. T. Debelouchina, V. S. Bajaj, K.-N. Hu, C.-G. Joo, M. L. Mak-Jurkauskas, J. R. Sirigiri, P. C. A. van der Wel, J. Herzfeld, R. J. Temkin,

and R. G. Griffin. Dynamic nuclear polarization at high magnetic fields. *The Journal of Chemical Physics*, 128(5):052211–052219, 2008.

[54] A. B. Barnes, G. De Paepe, P. C. A. van der Wel, K.-N. Hu, C.-G. Joo, V. S. Bajaj, M. L. Mak-Jurkauskas, J. R. Sirigiri, J. Herzfeld, R. J. Temkin, and R. G. Griffin. High-field dynamic nuclear polarization for solid and solution biological NMR. *Applied magnetic resonance*, 34(3-4):237–263, 2008.

[55] Jr Kaelin, W. G. and C. B. Thompson. Q&A: cancer: clues from cell metabolism. *Nature*, 465(7298):562–564, 2010.

[56] O. Warbung. On the origin of cancer cells. *Science*, 123(3191):309–314, 1956.

[57] D. M. Wilson, K. R. Keshari, P. E. Z. Larson, A. P. Chen, S. Hu, M. Van Criekinge, R. Bok, S. J. Nelson, J. M. Macdonald, D. B. Vigneron, and J. Kurhanewicz. Multi-compound polarization by DNP allows simultaneous assessment of multiple enzymatic activities in vivo. *Journal of Magnetic Resonance*, 205(1):141–147, 2010.

[58] Pekka Tapani Sipilä. *Real-Time Magnetic Field Monitoring in Magnetic Resonance Imaging*. PhD thesis, Technische Universität München, 2011.

[59] Oleksandr Khegai. Optimierung von spektral-räumlichen bildgebungssequenzen für hyperpolarisierte ^{13}C magnetresonanzbildgebung. Master's thesis, Technische Universität München, 2009.

[60] Jürgen Kürsch. *Konzeption und Realisierung eines skalierbaren Simulators für die Magnetresonanz-Tomographie*. PhD thesis, Rheinisch-Westfälische Technische Hochschule Aachen, 2003.

[61] J. M. Pauly. RF pulse design: SLR algorithm, spectral-spatial pulses, 2D and 3D pulses. In *Proceedings of the 9th Annual Meeting of ISMRM*, 2001.

[62] J. Pauly, P. Le Roux, D. Nishimura, and A. Macovski. Parameter relations for the Shinnar-Le Roux selective excitation pulse design algorithm. *IEEE Transactions on Medical Imaging*, 10(1):53–65, 1991.

[63] J.J. Gromov, N.A. Zemskoj, A.V. Lagutin, O.G. Ivanova, and V.M. Tutunnik. *Optimal control of dynamic systems*. TGTU, 2nd edition, 2007.

[64] D. Rosenfeld and Y. Zur. Design of adiabatic selective pulses using optimal control theory. *Magnetic Resonance in Medicine*, 36:401–409, 1996.

[65] Timo O. Reiss. *Anwendung der Steuerungstheorie auf die kernmagnetische Resonanzspektroskopie - Von der Entwicklung computergestützter Optimierungsmethoden bis zur experimentellen Umsetzung*. PhD thesis, Technische Universität München, 2003.

[66] S. Conolly, D. Nishimura, and A. Macovski. Optimal control solutions to the magnetic resonance selective excitation problem. *IEEE Transactions on Medical Imaging*, 5(2):106–115, 1986.

[67] D. Xu, K. F. King, Y. Zhu, G. C. McKinnon, and Z.-P. Liang. Designing multichannel, multidimensional, arbitrary flip angle RF pulses using an optimal control approach. *Magnetic Resonance in Medicine*, 59:547–560, 2008.

[68] Sven Mansson. *Hyperpolarized nuclei for NMR imaging and spectroscopy.* PhD thesis, Lund University, 2002.

[69] J. L. Neves, B. Heitmann, N. Khaneja, and S. J. Glaser. Heteronuclear decoupling by optimal tracking. *Journal of Magnetic Resonance*, in press, 2009.

[70] Jochen Leupold. *Neue Methoden zur frequenzselektiven Kernspintomographie mit TrueFISP-Sequenzen.* PhD thesis, Albert-Ludwigs-Universität Freiburg, 2005.

[71] T. E. Skinner, T. O. Reiss, B. Luy, N. Khaneja, and S. J. Glaser. Application of optimal control theory to the design of broadband excitation pulses for high-resolution NMR. *Journal of Magnetic Resonance*, 163:8–15, 2003.

[72] M. T. Vlaardingerbroek and J. A. den Boer. *Magnetic resonance imaging.* Springer, 2nd edition, 1999.

[73] N. Khaneja, T. Reiss, C. Kehlet, T. Schulte-Herbrüggen, and S. J. Glaser. Optimal control of coupled spin dynamics: design of NMR pulse sequences by gradient ascent algorithms. *Journal of Magnetic Resonance*, 172:296–305, 2005.

[74] L. Vanhamme, T. Sundin, P. Van Hecke, and S. Van Huffel. MR spectroscopy quantitation: a review of time-domain methods. *NMR in Biomedicine*, 14(4):233–246, 2001.

[75] S. B. Reeder, J. H. Brittain, T. M. Grist, and Y.-F. Yen. Least-squares chemical shift separation for ^{13}C metabolic imaging. *Journal of Magnetic Resonance Imaging*, 26(4):1145–1152, 2007.

[76] S.G. Mallat and Z. Zhang. Matching pursuits with time-frequency dictionaries. *IEEE Transactions on Signal Processing*, 41(12):3397–3415, 1993.

[77] S. S. Chen, D. L. Donoho, and M. A. Saunders. Atomic decomposition by basis pursuit. *SIAM Review*, 43(1):129, 2001.

[78] R. F. Schulte, J. I. Sperl, E. Weidl, M. I. Menzel, M. A. Janich, O. Khegai, M. Durst, J. H. Ardenkjaer-Larsen, S. J. Glaser, A. Haase, M. Schwaiger, and F. Wiesinger. Saturation-recovery metabolic-exchange rate imaging with

hyperpolarized [1-^{13}C] pyruvate using spectral-spatial excitation. *Magnetic Resonance in Medicine*, 69(5):1209–16, 2012.

[79] K. Derby, J. Tropp, and C. Hawryszko. Design and evaluation of a novel dual-tuned resonator for spectroscopic imaging. *Journal of Magnetic Resonance*, 86:645–651, 1990.

[80] R. A. de Graaf. *Front Matter. In Vivo NMR Spectroscopy.* John Wiley and Sons, Ltd, 1 edition, 2007.

[81] M. Marjanska, T. Teisseyre, N. Halpern-Manners, Y. Zhang, I. Iltis, V. Bajaj, K. Ugurbil, A. Pines, and P.-G. Henry. Measurement of arterial input function in hyperpolarized ^{13}C studies. *Applied Magnetic Resonance*, 43(1):289–297, 2012.

[82] H. J. Atherton, M. A. Schroeder, M. S. Dodd, L. C. Heather, E. E. Carter, L. E. Cochlin, S. Nagel, N. R. Sibson, G. K. Radda, K. Clarke, and D. J. Tyler. Validation of the in vivo assessment of pyruvate dehydrogenase activity using hyperpolarised ^{13}C MRS. *NMR in Biomedicine*, 24(2):201–208, 2011.

[83] D. Mayer, Y. S. Levin, R. E. Hurd, G. H. Glover, and D. M. Spielman. Fast metabolic imaging of systems with sparse spectra: Application for hyperpolarized ^{13}C imaging. *Magnetic Resonance in Medicine*, 56(4):932–937, 2006.

[84] M. A. Schroeder, H. J. Atherton, L. E. Cochlin, K. Clarke, G. K. Radda, and D. J. Tyler. The effect of hyperpolarized tracer concentration on myocardial uptake and metabolism. *Magnetic Resonance in Medicine*, 61(5):1007–1014, 2009.

[85] G. Lucignani, G. Paganelli, and E. Bombardieri. The use of standardized uptake values for assessing FDG uptake with PET in oncology: a clinical perspective. *Nuclear Medicine Communications*, 25(7):651–656, 2004.

List of Figures

List of Tables

List of Abbreviations and Symbols

Abbreviations

NMR	nuclear magnetic resonance
MR	magnetic resonance
MRI	magnetic resonance imaging
MRS	magnetic resonance spectroscopy
SNR	signal-to-noise ratio
CNR	contrast-to-noise ratio
CR	contrast resolution
DNP	dynamic nuclear polarization
CS	chemical shift
CSI	chemical shift imaging
FID	free induction decay
RF	radio frequency
CPMG	Carr-Purcell-Meiboom-Gill pulse sequence
SSFP	steady state free precession pulse sequence
TE	echo time
TR	repetition time
FDG	fludeoxyglucose
TCA	tricarboxylic acid
LDH	lactate dehydrogenase
NADH	nicotinamide adenine dinucleotide
ALT	alanine transaminase
PDH	pyruvate dehydrogenase
CA	carbonic anhydrase
OCT	optimal control theory

Symbols

γ	gyromagnetic ratio
h	Planck constant
k_B	Boltzmann constant
χ	magnetic susceptibility
$\rho(x, y)$	spin density
$\vec{B_0}$	external magnetic field
$\delta\vec{B}$	magnetic field inhomogeneity
$\vec{G}$	magnetic field gradient
$\vec{B_1}$	RF pulse magnetic field
ω_L	Larmor frequency
$\vec{\omega}$	angular frequency
ω_i	chamical shift frequency
$\vec{M}$	magnetization vector
M_0	thermal equilibrium magnetization
M_z	longitudinal magnetization
M_{xy}, M_T	transverse magnetization
α	flip angle
T_1	spin-lattice relaxation time
T_2	spin-spin relaxation time
J	total cost function
J_{run}	running cost
J_{fin}	final cost
$\vec{\lambda}$	Lagrange multiplier
t_n	sampling time
a_m	metabolite signal amplitude
$\tilde{a}_m$	metabolite signal amplitude in frequency domain
$k_{pyr\to m}$	apparent build-up rate
$k_{m\to pyr}$	apparent depletion rate
$R_{eff,m}$	effective decay rate
$\tilde{R}_{eff,m}$	average decay rate

List of Publications

Journals

1. M. A. Janich, M. I. Menzel, F. Wiesinger, E. Weidl, O. Khegai, J. H. Ardenkjaer-Larsen, S. J. Glaser, A. Haase, R. F. Schulte, and M. Schwaiger. "Effects of pyruvate dose on in vivo metabolism and quantification of hyperpolarized ^{13}C spectra." *NMR in Biomedicine*, 25(1):142-51, 2012.
2. F. Wiesinger F, E. Weidl, M. I. Menzel, M. A. Janich, O. Khegai, S. J. Glaser, A. Haase, M. Schwaiger and R. F. Schulte. "IDEAL spiral CSI for dynamic metabolic MR imaging of hyperpolarized [1-^{13}C]pyruvate." *Magnetic Resonance in Medicine*, 68(1):8-16, 2012.
3. R.F. Schulte , J. I. Sperl, E. Weidl, M. I. Menzel, M. A. Janich, O. Khegai, M. Durst, J. H. Ardenkjaer-Larsen, S. J. Glaser, A. Haase, M. Schwaiger and F. Wiesinger. "Saturation-recovery metabolic exchange rate imaging with hyperpolarised [1-^{13}C]pyruvate using spectral-spatial excitation." *Magnetic Resonance in Medicine*, 69(5):1209-16, 2012.
4. M.I. Menzel, E. V. Farrell, M. A. Janich, O. Khegai, F. Wiesinger, S. Nekolla, S. van Marwick, A. Otto, A. Haase, R. F. Schulte and M. Schwaiger. "Multimodal assessment of in vivo biochemistry: Hyperpolarized [1-^{13}C]MRS and ^{18}F-FDG-PET imaging in HCC tumor bearing rats." *Journal of Nuclear Medicine*, jnumed.112.110825, 2013.
5. O. Khegai, R. F. Schulte, M. A. Janich, M. I. Menzel, E. Farrell, A. M. Otto, J. H. Ardenkjaer-Larsen, S. J. Glaser, A. Haase, M. Schwaiger and F. Wiesinger. "Apparent rate constant mapping using hyperpolarized [1-^{13}C]pyruvate." (submitted to *NMR in Biomedicine*).

Conference proceedings

1. O. Khegai, A.M. Otto, M.A. Janich, R.F. Schulte, M.I. Menzel, E. Weidl, S.J. Glaser, S.I. Ziegler, A. Haase, M. Schwaiger, F. Wiesinger. "Quantification method for time-resolved hyperpolarized ^{13}C metabolic imaging." In *Proceedings of ESMRMB*, 2011 (Certificate of Merit).
2. P. A. Gomez Damian, J. I. Sperl, O. Khegai, M. A. Janich, F. Wiesinger, E. Weidl, S. J. Glaser, M. Schwaiger, R. F. Schulte, A. Haase, M. I. Menzel. "Multi-side kinetic model to assess [1-^{13}C]pyruvate in-vivo metabolism." In *Proceedings of ESMRMB*, 2011.
3. M. T. Durst, R. F. Schulte, F. Schilling, E. Weidl, O. Khegai, M. A. Janich, J. I. Sperl, F. Wiesinger, M. Schwaiger, A. Haase. "Parallel spiral CSI for metabolic imaging with hyperpolarised ^{13}C." In *Proceedings of ESMRMB*, 2011.
4. R.F. Schulte, J. I. Sperl, M. Durst, A. Haase, M. Irkens, M. Manglberger, E. Weidl, M. A. Janich, O. Khegai, G. Kudielka, M. I. Menzel, S. J. Glaser, M. Schwaiger, F. Wiesinger. "Advanced parallel imaging techniques for metabolic imaging with hyperpolarised ^{13}C." Third International Symposium on Dynamic Nuclear Polarization, Lausanne, Switzerland, 2011.
5. A.M. Otto, O. Khegai, F. Wiesinger, M.I. Menzel, R.F. Schulte, S.I. Ziegler, S.J. Glaser. "Metabolic flux of tumor cell spheroids measured by nuclear magnetic resonance using hyperpolarized ^{13}C-pyruvate." In *Proceedings of ISPDC*, 2011.
6. D. J. Scholz, O. Khegai, E. Kubala, A. Otto, M. Schwaiger, R. F. Schulte, A. Haase, M. I. Menzel. "Hyperpolarization of ^{13}C-bicarbonate for spatial MRI pH-detection." In *Proceedings of ISPDC*, 2011.
7. F. Wiesinger, O. Khegai, J. I. Sperl, E. Weidl, A. Haase, M. Schwaiger, R. Schulte. "Frequency-domain quantification and interpretation of dynamic hyperpolarized ^{13}C metabolic imaging." In *Proceedings of ISMRM*, 2012.
8. P. A. Gomez Damian, J. I. Sperl, O. Khegai, S. Grott, E. Weidl, M. Janich, F. Wiesinger, S. J. Glaser, A. Haase, M. Schwaiger, R. F. Schulte, M. I. Menzel. "Multi-side kinetic modeling of ^{13}C metabolic MR using [1-^{13}C]pyruvate." In *Proceedings of ISMRM*, 2012.

9. M.I. Menzel, E. Weidl, M. Janich, O. Khegai, F. Wiesinger, A. Haase, R. F. Schulte, M. Schwaiger. "In vivo biochemical imaging of HCC tumor bearing rats using hyperpolarized ^{13}C-pyruvate and ^{18}F-FDG." In *Proceedings of ISMRM*, 2012.

10. R.F. Schulte, J. I. Sperl, E. Weidl, M. I. Menzel, M. A. Janich, O. Khegai, M. Durst, J. H. Ardenkjaer-Larsen, S. J. Glaser, A. Haase, M. Schwaiger, F. Wiesinger. "Saturation-recovery metabolic exchange rate imaging with hyperpolarised [1-^{13}C]pyruvate using spectral-spatial excitation." In *Proceedings of ISMRM*, 2012.

11. M. Durst, R.F. Schulte, F. Schilling, E. Weidl, O. Khegai, M.A. Janich, J. I. Sperl, F. Wiesinger, M. Schwaiger, A. Haase. "Parallel spiral CSI for metabolic imaging with hyperpolarised ^{13}C." In *Proceedings of ISMRM*, 2012.

12. E. Weidl, M. Menzel, M. Janich, O. Khegai, F. Wiesinger, S. G. Nekolla, A. Haase, R. Schulte, M. Schwaiger. "In vivo detection of tumor metabolism with ^{18}F-FDG PET and hyperpolarized [1-^{13}C]-pyruvate magnetic resonance spectroscopic imaging." In *Proceedings of SNM*, 2012.

13. R.F. Schulte , J. I. Sperl, E. Weidl, M. I. Menzel, M. A. Janich, O. Khegai, M. Durst, J. H. Ardenkjaer-Larsen, S. J. Glaser, A. Haase, M. Schwaiger, F. Wiesinger. "Quantitative metabolic imaging methods for hyperpolarised ^{13}C." In *Proceedings of EUROMAR*, 2012.

14. F. Wiesinger, O. Khegai, E. Weidl, A. Haase, M. Schwaiger, R. Schulte. "Metabolic rate constant mapping using hyperpolarized ^{13}C spectroscopic MR imaging." In *Proceedings of WMIC*, 2012.

15. O. Khegai , A. M. Otto, R. F. Schulte, P. T. Sipilae, M. I. Menzel, S. J. Glaser, S. I. Ziegler, A. Haase, M. Schwaiger, F. Wiesinger. "In vitro measurement of pyruvate metabolism using hyperpolarized ^{13}C MRS." In *Proceedings of ICMRBS*, 2012.

16. D.J. Scholz, O. Khegai, A. Otto, R.F. Schulte, M. Schwaiger, S. Ziegler, A. Haase, M.I. Menzel "Quantitative pH analysis with sodium ^{13}C-Bicarbonate at small pH variations." In *Proceedings of ESMRMB*, 2012.

17. O. Khegai, R. F. Schulte, M. A. Janich, M. I. Menzel, E. Weidl, A. M. Otto, S. J. Glaser, S. I. Ziegler, A. Haase, M. Schwaiger, F. Wiesinger. "In vivo mapping of metabolic rate constants with hyperpolarized [1-^{13}C]pyruvate." The Third International Workshop on Metabolic Imaging, Philadelphia, USA, 2012.

18. A.M. Otto, O. Khegai, F.Wiesinger, M.I. Menzel, R. F. Schulte. "Effects of extracellular pH on the activity of pyruvate kinase and lactate dehydrogenase in MCF-7 cells." In *Proceedings of ISPDC*, 2012.

19. O. Khegai, R. F. Schulte, M. A. Janich, M. I. Menzel, E. Farrell, A. M. Otto, J. H. Ardenkjaer-Larsen, S. J. Glaser, A. Haase, M. Schwaiger, F. Wiesinger. "Apparent rate constant mapping using hyperpolarized [1-^{13}C]pyruvate." In *Proceedings of ISMRM*, 2013.

20. R. F. Schulte, O. Khegai, E. Farrell, M. A. Janich, M. I. Menzel, A. Haase, M. Schwaiger, F. Wiesinger. "Metabolic exchange rate imaging with hyperpolarised [1-^{13}C]pyruvate." In *Proceedings of ISMRM*, 2013.

Acknowledgments

I would like to thank to the following people who have contributed to this work in one or another way and have made the last four years a great learning experience for me:

My supervisors, Professor Steffen J. Glaser and Professor Sibylle I. Ziegler, for all the time and effort you have put into giving me guidance and also for giving me flexibility to work on projects of my interest.

Dr. Florian Wiesinger, for his thorough supervision, kind support and efforts, which have greatly contributed to the success of this work.

Dr. Rolf F. Schulte, Dr. Martin A. Janich and Dr. Marion I. Menzel for all the fruitful discussions and constructive feedback.

Colleagues involved in hyperpolarization experiments and daily discussions, Guido Kudielka, Dr. Pekka Sipilä, Dr. Jonathan I. Sperl, Dr. Concetta Gringeri, Dr. Franz Schilling, Stephan Düwel, Markus Durst, Ulrich Köllisch, Johannes Scholz, and Eugen Kubala.

PD Dr. Angela M. Otto, Josef Hintermair and Dr. Eliane Farrell, for the close collaboration and valuable assistance conducting in vitro and in vivo experiments.

Colleagues in the Diagnostics & Biomedical Technologies Lab, for the friendly working atmosphere and support in many details throughout my work.

General Electric Global Research Europe and all the people working there, for giving me the opportunity to use their great facility and administrative support.

The group of Professor Steffen Glaser (Fachgebiet Organische Chemie) for many fruitful discussions and kind cooperation.

The Graduate School of Information Science in Health at Technische Universität München and the German Bundesministerium für Bildung und Forschung for giving financial and administrative support to this work.

My family and friends, who have given me the opportunities and principles that I live for.